The University of Alberta

Determination of Elastic coefficients of Materials by Laser Speckle Interferometry.

By

Shahryar Shareef ©

A thesis submitted to the Faculty of Graduate Studies and
Research in partial fulfillment of the requirements for the degree
of Master of Science
in
Geophysics

Department of Physics

University of Alberta
Edmonton, Alberta
Fall 2002

University of Alberta

Library Release Form

NAME OF AUTHOR: Shahryar Shareef

TITLE OF THESIS: Determination of Elastic coefficients of Materials by Laser Speckle Interferometry.

DEGREE: Masters of Science.

YEAR THIS DEGREE GRANTED: 2002.
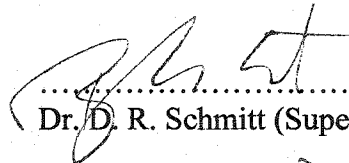
Shahryar Shareef
602 Avadh Bhatia Physics Building
University of Alberta
Edmonton, Alberta
Canada T6G 2J1
shareef@phys.ualberta.ca
sshahryar@netscape.net
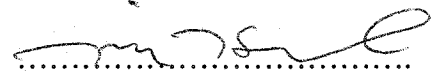
Apri 30th, 2002

The University of Alberta

Faculty of Graduate Studies and Research

The undersigned certify that they have read, and recommend to the Faculty of Graduate Studies and Research, for acceptance, a thesis entitled *Determination of Elastic coefficients of Materials by Laser Speckle Interferometry* submitted by *Shahryar Shareef* in partial fulfilment of the requirements for the degree of Master of Science in Geophysics.

....
Dr. D. R. Schmitt (Supervisor)

....
Dr. M. Heimpel (co-supervisor)

....
Dr. M. Freeman (Physics)

....
Dr. L. Sigurdson (Mech. Eng.)

April the 16th, 2002.

Abstract

Electronic Speckle Pattern Interferometry (ESPI) is becoming more and more popular for deformation analysis and material testing due to its non-invasive nature. In the present work ESPI is used to determine Young's modulus E and Poisson ratio v of materials. First a perfect noise-free synthetic fringe pattern is created assuming normal loading on the material. In the virtual inversion, an iterative minimum error procedure (Least Square Minimization) is used to determine Young's modulus and Poisson ratio. It employs the relative fringe order of picked positions of fringe maxima and minima within a single interferogram. The results from this virtual inversion are within 0.1% of the original values of the Young's modulus and Poisson ratio. Next this method is tested experimentally on a homogeneous block of Plexiglas loaded with a normal force to determine its Young's modulus and Poisson ratio values. The resultant E and v values are within 4% and 1% of the respective values obtained by the standard strain gauge method. This method is then applied to a non-homogeneous marble sample. Finally, Young's modulus of an aluminum and marble sample in the form of a cantilever beam are determined experimentally. The result for aluminum is 60.5 GPa which is within 1% of the actual value of that aluminum beam obtained by the standard strain gauge method. The Young's modulus of marble resulted between 19 GPa and 13 GPa.

Acknowledgement

At the end of this research work when I look back I see numerous people who directly or indirectly inspired me, motivated me and helped me carry on the work to the finish. It is impossible to name all of them in this brief acknowledgement. My appreciation and gratefulness goes to all while I name only a few here.

The first person whom I owe most of my gratitude and respect is my supervisor Dr. D. R. Schmitt not only for allowing me to work under his supervision, help and guidance throughout but also for his extreme patience, smiling face even at the toughest time and soft spoken humoristic character that showed me again and again how to face the challenges of everyday life easily. He helped me both implicitly and explicitly to bring this study near completion.

I thank my co-supervisor Dr. M. Heimpel for many meaningful discussions that we had during the course of the research and the other members of the committee Dr. M. Freeman and Dr. L. Sigurdson for their time and support. I am also grateful to Dr. M. Sacchi for many useful discussions.

My warmest thanks to Mr. Bernie Faulkner (Specialist Machinist, Mech. Eng. Dept., University of Alberta), Mr. Gilbert Lachat, Mr. Tony Paget and Mr. Paul Zimmermann for their contribution in material testing and in manufacturing of the experimental devices.

Many thanks to my co-workers especially to Ulrich, Henning, Marko, Ismael, Marek, and Wolfgang for their many important suggestions.

I am also extremely thankful to Michael Lazorek and Len Tober for helping me throughout with many small details and Dr. F. Weichman for all the encouragement.

My gratefulness to Dr. Robert Jones for allowing me to use pictures from his book which was a constant guide throughout the research. Also my gratitude to Ms. Lynn Chandler of Graduate Studies who helped me get over every problem I had talked about and who works hard for the benefit of the graduate students.

Finally my gratitude to my loving wife Roksana who accepted all the hard times quietly, patiently and stood beside me in every situation. I owe much to her.

'Dedicated to a few very special people'
My
Father, Mother, Sisters, Brother
and
my loving wife.

Table of Contents

List of Tables

List of Figures

Chapter 4

Appendix

List of Figures

List of Symbols

Chapter 2

P = Probability.

I = Intensity.

σ = Standard deviation.

R = Autocorrelation function.

d_{sp} = Speckle size.

$\mathbf{n}$ = Unit vector.

φ = phase change.

λ = Wavelength.

Φ = Sum of the intensity of the incident waves.

ψ = Phase difference.

$\Delta\varphi$ = Change in phase.

V = Voltage.

ρ_{xy} = Correlation co-efficient.

r = Discrete local correlation coefficient.

Chapter 3

U = Displacement vector.

ν = Poisson's ratio.

E = Young's modulus.

F = Load.

$\mathbf{n}$ = Unit vector.

λ = Wavelength.

K = Sensitivity vector.

ρ = Fringe intensity.

n = Fringe order.

φ = Change in phase.

Chapter 4

U_z = Deflection in z-direction.

F = Load.

E = Young's modulus.

I = Moment of inertia.

L = Length of the cantilever.

n = Unit vector.

ρ = Fringe intensity.

φ = Change in phase.

λ = Wavelength.

n = Fringe order.

Chapter 1

Introduction

1.1 Motivation

A surface that appears smooth to the unaided eye may well be quite rough on the scale of optical wavelengths. Coherent laser light reflected from such a surface shows a speckled pattern of randomly distributed dark and bright patches. These patches arise from the constructive and destructive interference of waves reflected from the roughness of the surface and contain important information about the state of the surface. The phenomenon of laser speckle can be used as a very sensitive method of vibration, stress, strain, displacement, and material properties determination by measuring the surface displacement.

Despite the fact that there are well-accepted methods for measuring these parameters, complementary efforts have focussed on developing optical interferometry[1-3] as a tool. Optical methods are desirable because information is obtained over the entire field of view, the object need only be appropriately illuminated and only little surface preparation is required. There are a number of complementary optical techniques. Some of the most popular methods include Double exposure holography[2], Moiré interferometry[3] and Electronic Speckle Pattern Interferometry[1] (ESPI). Each of the different, but complementary, methods has its advantages and disadvantages for different applications.

Double exposure holography (DEH) is perhaps the oldest of the techniques and continues to be used today[4-6]. In its simplest form, two holograms of an object before and after motion of its surface are recorded on the same piece of film. Reconstruction of the interference of these two wave fields produces a series of fringe patterns superimposed on the three-dimensional image of the object. Analysis of the fringe

patterns can allow for the determination of displacements on the order of one-quarter or better of the wavelength of the light employed. One of the drawbacks is that constructing the necessary geometry of reference and object beams might be difficult in constrained locations.

In Moiré interferometry[3] a diffraction grating, typically 1200 lines/mm, is mounted or scribed on the surface of the object to be studied. The object is illuminated under two opposing, collimated beams, both incident on the object at the same angle. Under this geometry, the angle of intersection between the two beams is zero and a uniform intensity is observed. Once the object is deformed, the angle of intersection is no longer zero and the two diffracted wave fields interfere to form a fringe pattern. Moiré fringe patterns have good signal to noise ratios and are well resolved such that an accuracy of $\pm 0.02 \mu m$ is possible. One constraint of this method is that the diffraction grating must be placed on the object in the area to be studied; this may require special machining of the object or the placement of a prepared diffraction grating using epoxies that could influence the experiment.

In ESPI, slight changes in the speckle pattern produced by motion of the object between two video frames provide the basic information. The method exploits the fact that each speckle on the surface of an object illuminated with coherent radiation is an interferometer whose intensity varies cyclically depending on the change in the phase of the light scattered from the location of the speckle. Consequently, the wrapped phase is determined by local correlations of the observed speckle pattern. The major advantages of this method are: there is considerable latitude for placement of source beams and the observing camera, little or no surface preparation is required and the method is inexpensive to implement.

Because of its overall simplicity, ESPI has been chosen to determine material properties in this present work. Before proceeding further into the work, a review of the developments and measurements done using laser speckle interferometry are necessary.

1.2 Literature Review

Since the invention of laser in early 1960s, laser speckles have been found to be an inherent characteristic of any laser experiment. Initially it was thought to be undesirable noise in interferometry but later on was found to contain vast amounts of information about the deformation state of the object. In this chapter a review has been made on the research in determination of stress, strain, displacement, material properties etc. using laser speckle interferometry.

In his paper, Leendertz[7] described the speckle correlation phenomenon which occurred due to the change in an optical path difference. Using a modified Michelson interferometer, he measured an out of plane displacement by recording two images of an object, before and after deformation, on two photo sensitive plates. Light waves transmitted through these plates were diffracted to yield the out of plane displacement fringes. Following this work, Butters and Leendertz[8] developed a double photographic exposure version of the above technique referred to as double exposure speckle pattern interferometry. Two images of an object, before and after deformation, were recorded on a single photographic plate. The film plate was given a small displacement between exposures. The developed film plate shows deformation fringe patterns.

Jones and Wykes[9] presented a thorough study of ESPI interferometers from the viewpoint of optimization of an optical system design. In their study they concentrated on parameters such as television camera characteristics, input laser power, and type of interferometers available for vibration and displacement measurements.

Linear elastic fracture mechanics (LEFM) has been widely used in rock mechanics and experimental studies have indicated that in rock a microcracking process zone exists ahead of the tip of crack. In their work Chengyong *et.al.*[10] observed the growth and formation of the microcracking process zone for three kinds of rock by laser speckle interferometry. The effects of crack width and grain size on the process zone fracture are also studied and the relation between the load and the crack tip opening displacement are examined. They found that the microcrack forms ahead of the crack and then links to form a microcrack damage zone. When the load approaches the initial

crack load, the microcrack process zone extends and widens with the development of many microcracks. They found that the shape and size of the process zone observed by the optical microscope are same as the results observed by the laser speckle method.

Dimensional accuracy of components is extremely important to the manufacturing industry. Very often curvatures are used in specifying the profile of components which, after being machined, turns out to be difficult to measure. In their paper Shang *et. al.*[11] presented a non-contacting and whole field method of measuring curvatures using a moving laser source and image shearing camera. The resulting interference fringe pattern, which is related to the slope of the profile, provided with the information of the curvatures. To enhance the feasibility of this technique in the industrial environment, optical fibres were used so that the desired movement of the laser source could be achieved readily. They applied this technique to measure the profile of wire-cut cylinders having circular and elliptical cross-sections.

Holder[12] *et. al.* investigated the performance of a digital speckle correlation interferometer using an image fibre, both theoretically and experimentally. They derived an expression for the visibility of correlation fringes in terms of spatial filtering properties of the image fibre. The visibility of fringes depends mainly on the resolution of the image fibre as well as the in-plane displacement of diffuse objects. The results show that a computerized video system combined with the image fibre is suitable for laser speckle interferometry.

Laser speckle interferometry has been used to detect and quantify the rust build up on metal surfaces under water by Koyuncu *et. al.*[13] . A CCD camera and a frame grabber card captured speckle information from the sample metal surface. Software techniques were used to convert the image data files in ASCII files in an appropriate format. Three-dimensional surface plots were generated to define the numerical values for the amount of rust build up.

The generation and detection of elastic wave by photo-elastic methods, known as 'laser ultrasonic' is now a commonly used method in research. Bayon *et. al.*[14] used laser speckle interferometry to record the three components of transient vibration induced by an ultrasonic wave at a point on the surface of a solid model. They experimentally investigated the reliability of the method and illustrated maps of the local three-

dimensional transient vibration and particle trajectories of different points at the surface of the solid.

Xu *et. al.*[15] showed the results of experimental investigations using laser speckle interferometry on small sized three point bending notched beams and using photo-elastic coating and strain gauges on very large size compact tension specimens of concrete. Their investigation showed that there exists a stage of stable crack propagation before unstable fracture occurs. The results are in agreement with other investigations using Moiré interferometry[3], holographic interferometry[2] and the microscope[15]. Further the study shows that crack initiation, stable crack propagation and unstable fracture can be distinguished in the fracture process in concrete structures.

Transient in-plane displacements generated in a metal plate subjected to impact loading are measured using a pulsed digital speckle pattern interferometry system by Diaz and Kaufmann[16]. Two separated speckle patterns produced by a ruby laser are recorded using a CCD camera and stored in a frame grabber. Transient displacements are evaluated by digital analysis of the fringes generated by the subtraction of these speckle patterns. The computer used for image processing is also utilized to control image acquisition, to synchronize the laser pulses to the CCD camera and the object position. Experimental results are compared with numerical calculations obtained using the finite-element method and they are in agreement.

Anwander *et. al.*[17] presented a newly developed laser based non-contacting strain sensor suitable for temperatures up to 1200°C, which was adapted to a commercial tensile testing machine equipped with an electrical furnace. The principle of the strain sensor is based on tracking laser speckles through a digital correlation technique. Based on the experimental data, it has been shown that this simple laser-based strain sensor can be used successfully for the determination of mechanical and thermal strains up to temperatures of about 1200°C.

Finally a work done by Zhang *et. al.*[18] studied the elastic modulus of bone from a bovine femur using ESPI. They loaded a small piece of bovine bone prepared as a beam with three-point bending. Full field displacements are found from the interferograms, which are used as the solution for the analytical expression for the beam deflection

defined by classical mechanics of material. The results are in perfect agreement with the results reported in the open literature[19].

1.3 Conclusion

In this present work, ESPI has been used to determine the Young's modulus and Poisson ratio of materials. In the second chapter, the basic mechanism of speckle interferometry and the related mathematical formalism has been discussed. In the third chapter, first forward modeled synthetic fringe patterns are calculated and inverted in a virtual inversion experiment and then experimental fringe patterns are generated and inverted using the same method. In the fourth chapter, experiments have been carried out with aluminum and marble cantilevers and their Young's modulus has been determined.

References:

1. R. Jones and C. Wykes, *'Holographic and speckle interferometry'*, Cambridge University press, Cambridge, 1983.

2. T. Kreis, *'Holographic interferometry – Principles and methods'*, Akademie Verlag, Berlin, 1996.

3. D. Post, B. Han, and P. Ifju, *'High sensitivity Moiré (Experimental analysis for mechanics and materials)'*, Springer-Verlag, New York, 1994.

4. A. Makino, and D. V. Nelson, *'Residual-stress determination by single-axis holographic interferometry and hole drilling - part1: Theory'*, Experimental Mechanics, 34, 66-78, 1994.

5. D. R. Schmitt, and Y. Li, *' Three-dimensional stress relief displacement resulting from drilling a blind hole in acrylic'*, Experimental Mechanics, 36, pp. 412-420, 1996.

6. A. Makino *et. al.*, *'Determination of biaxial residual stresses by a holographic hole drilling technique'*, J. Eng. Mat. Tech., 118, pp. 583-588, 1996.

7. J. A. Leendertz, *'Interferometric displacement measurement on scattering surfaces utilizing speckle effect'*, Physics E: Scientific Instruments, 3, pp. 214-218, 1970.

8. J. N. Butters and J. A. Leendertz, *'A double exposure technique for speckle pattern interferometry'*, Physics E: Scientific Instruments, 4, pp. 277-279, 1971.

9. R. Jones and C. Wykes, *'General parameters for the design and optimization of electronic speckle pattern interferometers'*, Optica Acta, 28, pp. 949-972, 1981.

10. W. Chengyong *et. al.*, *'Int. J. Rock Mech. Min. Sci. & Geomech. Abstr.'*, Vol.27, No.1, pp.65-69, 1990.

11. H. M. Shang *et. al.*, *'Journal of materials processing technology'*, 25, 3, pp.273-280, April, 1991.

12.   L. Holder *et. al.*, *'A digital speckle correlation interferometer using an image fibre'*, Measurement Science and Technology, 4, 7, pp.746-753, Jul,1993.

13.   B. Koyuncu *et. al.*, *'Quantization of surface rust using laser imaging techniques'*, Optics and Laser Technology, 27, 3, pp.199-203, June 1995.

14.   A. Bayon *et. al.*, *'Three-component recording of ultrasonic transient vibration by optical heterodyne interferometry'*, Journal of the Acoustical Society of America, 99, 2, pp. 954-961, Feb 1996.

15.   S. L. Xu *et. al.*, *'Determination of double-K criterion for crack propagation in quasi-brittle fracture, Part I: Experimental Investigation of Crack Propagation'*, International Journal of Fracture, 98, 2, pp.111-149, 1999.

16.   F. V. Diaz and G. H. Kaufmann, *'Impact-induced transient deformation analysis by means of digital speckle pattern interferometry'*, Experimental Mechanics, 39, 4, pp.311-316, Dec. 1999.

17.   M. Anwander *et. al.*, *'Noncontacting strain measurements at high temperatures by the digital laser speckle technique'*, Experimental Mechanics, 40, 1, March 2000.

18.   D. Zhang *et. al.*, *'Evaluating the elastic modulus of bone using electronic speckle pattern interferometry'*, Experimental Techniques, 25, 5, pp.32-34, Sep. 2001.

19.   S. C. Cowin *et. al.*, *'Properties of bone'* in handbook of Bioengineering, McGraw Hill, New York, 1987.

Chapter 2

Speckle Interferometry

2.1 Speckles and its Origin

A granular pattern appears on a surface illuminated with a coherent light source. This is known as the speckle effect[1]. A photographic image of a laser-illuminated surface is shown in Fig.2.1. A similar effect occurs in coherent radar and in ultrasonic imaging. This speckle effect occurs only when the surface is optically rough; i.e., its height variation is of the order of or greater than the wavelength of the illuminating light. When a laser beam illuminates such a surface, the intensity of the scattered light is found to vary randomly with position – this is known as objective speckle. On the other hand, when a rough surface is illuminated by laser light and an image of the surface is formed, the image shows a similar random intensity variation, but in this case the speckle is called 'subjective'. Details on the formation of these two different kinds of speckles are given below.

Objective speckle: Each point on an illuminated surface can be considered to absorb and re-emit the light, thus acting as a source of spherical waves. The complex amplitude of the scattered light at any point in space is given by the sum of the amplitudes of the contributions from each point on the surface. For a surface in the xy-plane (Fig.2.2), if the surface height at a point (x,y) is given by $\xi(x,y)$, then the complex
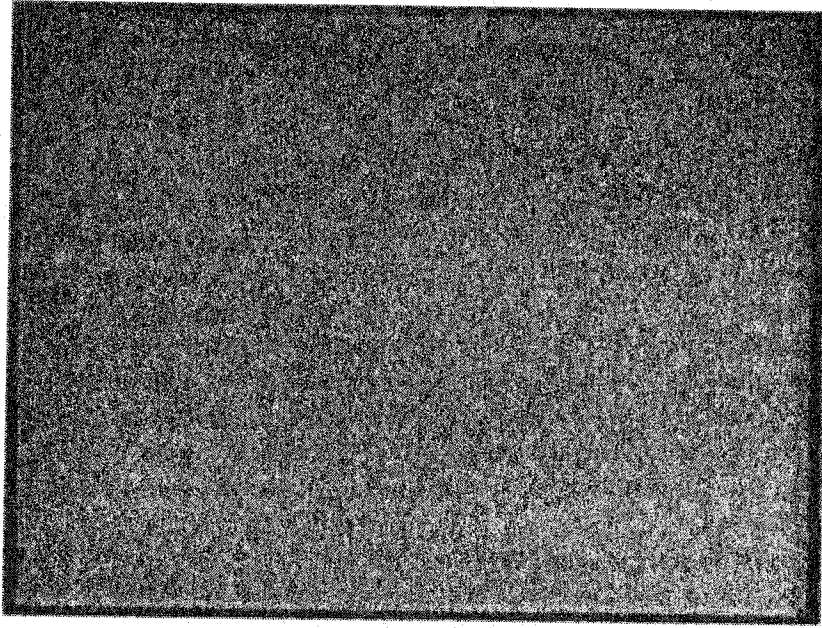
Figure-2.1: A subjective speckle pattern obtained by forming the image of an optically rough surface illuminated by a laser [Taken from Ref. 1, p.51, with kind permission of Dr. R. Jones].
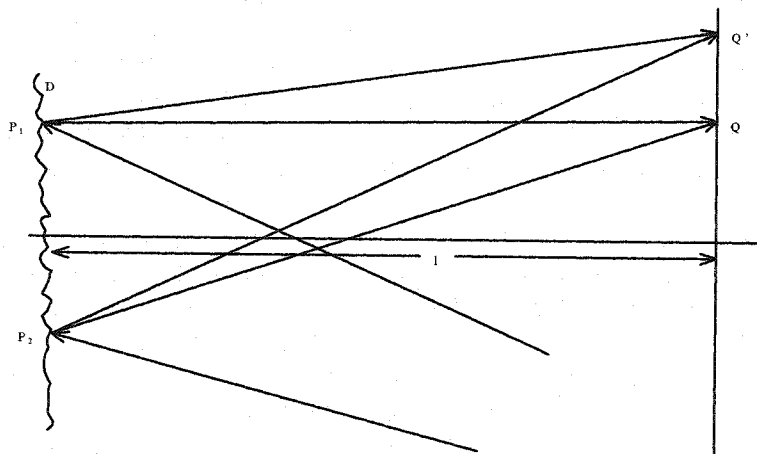
Figure-2.2: The scattering of light by a rough surface.

amplitude at a point P(r) is the sum of the components scattered from the whole surface and is given by

$$U(r) = K \int\limits_{-\infty}^{+\infty} \int u(x,y) \exp\left[\frac{2\pi i}{\lambda} G\xi(x,y) \right] dxdy \tag{2.1}$$

where K is a constant, *u(x,y)* represents the complex amplitude of the light incident at *(x,y)* and G is a geometric factor associated with the illumination and viewing directions which can be assumed to be constant when P is far away from the surface. Since the surface height is varying randomly by λ or more, the phase term $G\xi$(x,y) will also vary by amounts of λc or more where c is the speed of light. Hence the resultant amplitude at P is described by a set of vectors of random phase which when added together give random resultant amplitude. The total amplitude has a value which varies between zero and a maximum value determined by the magnitude and phase of the individual amplitudes. As the point P is varied, the resultant amplitude and hence, intensity, will have a different random resultant value. It is this random intensity variation which is the speckle effect. The statistical properties of speckle have been calculated by Goodman[2]. According to his calculation; the probability that the intensity I at a point, lies between I and I+dI is given by

$$P(I)dI = \frac{1}{\langle I \rangle} \exp\frac{-I}{\langle I \rangle} \tag{2.2}$$

where $\langle I \rangle$ is the expected intensity averaged over many points in the scattered field. The probability P(I') that the intensity is greater than some value I' is given by

$$P(I')dI = \exp\frac{-I'}{\langle I \rangle} \tag{2.3}$$

The mean value of the square of the intensity can be shown to be equal to $2\langle I \rangle^2$, so that the standard deviation of the intensity σ_I is

$$\sigma_I^2 = \langle I^2 \rangle - \langle I \rangle^2 = \langle I \rangle^2 \tag{2.4}$$

If the intensities of the scattered light at two points P and P′ are compared, it is clear that when these points are very close together, the two intensities are closely related but as they move further apart, the intensities become different. The separation of the

minima (or maxima) in the pattern falls within a fairly narrow range. This means speckle size cannot be quantified, but it can be related to the autocorrelation function $R(r_1,r_2)$ of the intensity distribution, defined as[2]

$$R(r_1,r_2) = \langle I(r_1)I(r_2) \rangle \qquad (2.5)$$

where the averaging is performed over many speckles and r_1 and r_2 refers to the positions. When $r_1 = r_2$, from Eq.(2.5), $R = \langle I^2 \rangle$. As (r_1-r_2) increases, the intensities $I(r_1)$ and $I(r_2)$ are no longer the same, and eventually become totally unrelated to one another. In that case

$$R(r_1,r_2) = \langle I(r_1) \rangle \langle I(r_2) \rangle \qquad (2.6)$$

Goodman[2] has derived an expression for the autocorrelation function of the scattered intensity where a uniform intensity beam of dimension L illuminates the surface such that an area of dimensions LxL is illuminated as

$$R(\Delta x, \Delta y) = \langle I^2 \rangle \left[1 + \sin c^2 \left(\frac{L\Delta x}{\lambda z} \right) \sin c^2 \left(\frac{L\Delta y}{\lambda z} \right) \right] \qquad (2.7)$$

where z is the distance between the viewing and object planes, and $(\Delta x, \Delta y)$ are the x and y coordinates of the vector (r_1-r_2) representing the change in viewing position.

The average 'size' of the speckle can be taken as the value of Δx (or Δy) for which the sinc function first becomes zero, given by:

$$(\Delta x)_s = \frac{\lambda z}{L} \qquad (2.8)$$

From Eq.(2.8) its seen that the size of the speckles observed in the light scattered by a rough surface at a given distance from the surface increases as the area illuminated decreases. This type of speckle is called objective because its scale depends only on the plane in space where it is viewed, and not on the imaging system used to view it.

Subjective or Image-plane speckle: The size of the speckles in this kind of speckle is dependent on the aperture of the viewing lens. This is why its termed as subjective speckle. This effect can be observed by comparing the size of the speckles when an object is viewed directly by eye and when an aperture smaller than the pupil is placed in front of the eye. In the latter case the speckle size will be seen to increase[1].

Alternatively, the same effect may be observed by focusing and defocusing one's eyes alternately when looking at the speckle pattern.

The probability distribution of the speckle intensity at a given point is the same as those of the objective speckle (Eqs. 2.2 to 2.4). However, the spatial distribution of the speckle is determined by the diffraction limit of the imaging system. According to Goodman[2], the expression for the autocorrelation function of the scattered intensity of the image-plane speckle is given by[2]

$$R(r) = \left\langle I^2 \right\rangle \left[1 + 2J_1\left(\frac{\pi a r}{\lambda v}\right) \bigg/ \left(\frac{\pi a r}{\lambda v}\right) \right] \tag{2.9}$$

where J_1 is the first order Bessel function. And the speckle size is[2]

$$d_{sp} = \frac{2.4 \lambda v}{a} \tag{2.10}$$

where 'a' is the diameter of the viewing lens aperture and v is the distance from the lens of the image plane. The formation of the speckle pattern is shown in Fig.2.3.

2.2   Phase in Coherent Imaging

In speckle interferometry, light is scattered from a rough surface illuminated with a coherent light source through a lens onto a plane which normally (but not necessarily) is the plane in which the object is in focus. In the following section, phase changes which arise in holographic and speckle interferometric experiments have been calculated.

In Fig.2.4, the surface is illuminated by a wavefront diverging from the point S and is in focus in the observation plane. A point P in the surface illuminates an area in the image plane centred on Q. The optical path from S to the point R via P is given by

$$l = SP + l_p + PO + OR \tag{2.11}$$

where SP and PO represent the mean distance from a region around P to S and O respectively, l_p is the optical path associated with the random variation of the surface height, and OR is the distance from O to R. Now, when the lens is focussed on a point T (Fig.2.5), the point Q in the viewing plane is illuminated by all the rays scattered from
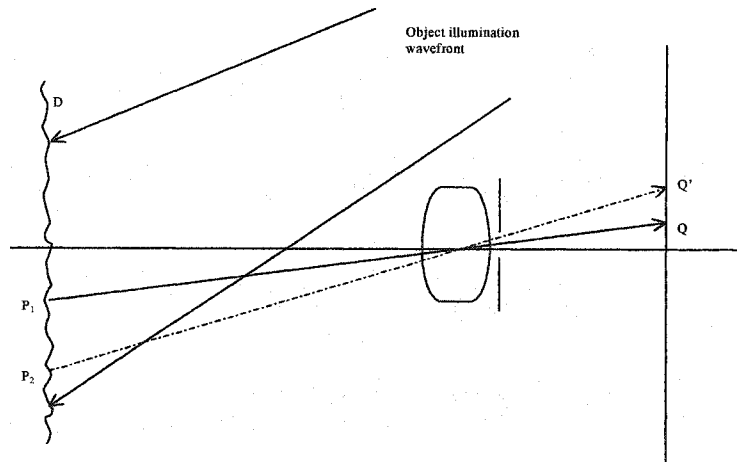
Figure-2.3: The formation of the speckle pattern in the image plane of a lens.
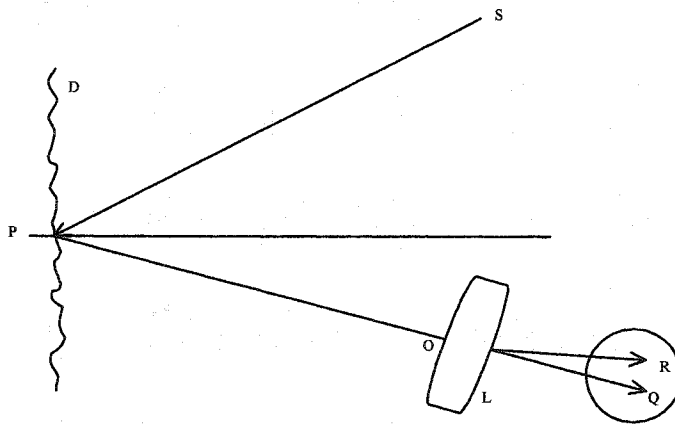
Figure-2.4: The optical path of a ray in subjective speckle: image-plane viewing.

the viewing lens aperture. Thus, the size of the area that illuminates a point in the viewing plane, is proportional to the viewing lens aperture diameter and inversely proportional to the distance between T and the viewing lens. Because the optical path from T to Q is the same for all ray directions, the optical path from S to Q via a point P is given by

$$l = SP + l_p + TQ - PT \tag{2.12}$$

when the viewing plane is the focal plane of the lens (Fig.2.6), T is effectively at infinity. All the rays illuminating a point Q in the viewing plane are parallel to MQ. The surface area illuminating a point in the viewing plane is now the projection of the viewing lens aperture on the object, so that unless viewing is at a very oblique angle, its diameter is approximately that of the viewing lens aperture. The optical path from S to Q via a point P is

$$l = SP + l_p + MQ + PN \tag{2.13}$$

when the object is displaced, so that the point P is displaced by d to P′, the optical path from the source S to a point in the viewing plane via a given point in the object is altered (Fig.2.7). This change in phase associated with the change in optical path length is the basis of speckle correlation techniques. If the change in optical path from S to P is Δl_1 then (from Fig.2.7)

$$\Delta l_1 = SP' - SP \tag{2.14}$$

For all practical arrangements SP>>$|d|$, so that

$$\Delta l_1 = SP' - SP = d \cos \gamma_1 \tag{2.15}$$

If the direction of SP and SP′ are given by a unit vector n_0 and $n_0′$, then assuming SP and SP′ are approximately parallel i.e. $n_0 \approx n_0′$, so that

$$\Delta \ell_1 = n_o \cdot d \tag{2.16}$$

The path length l_p can be assumed to be unchanged and the change in path Δl_2 associated with the path from P to Q (Fig.2.8) is given by

$$\Delta l_2 = d \cos \gamma_2$$

where its assumed that the direction in which the light is scattered from P to Q and from P′ to Q are approximately parallel. If this direction is given by n_s then

$$\Delta \ell_2 = -n_s \cdot d \tag{2.17}$$
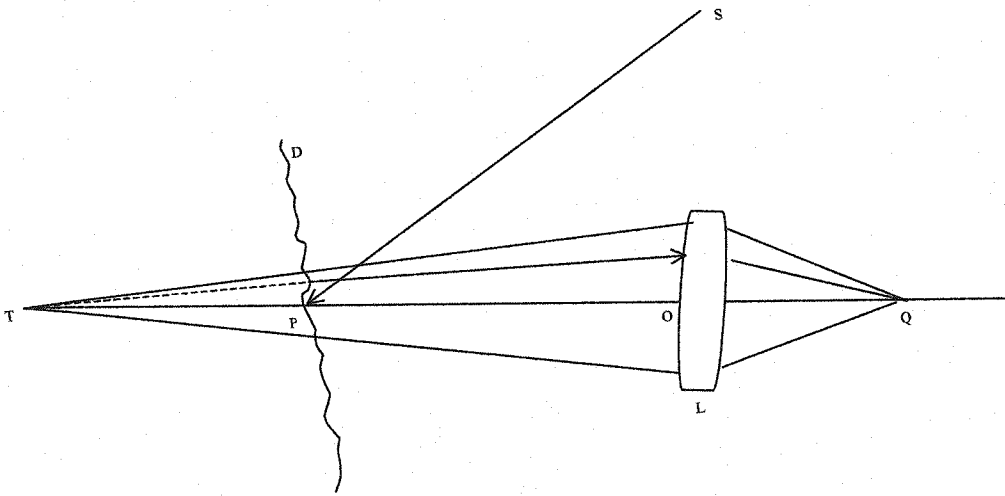
Figure-2.5: The optical path of a ray in subjective speckle: defocused viewing.
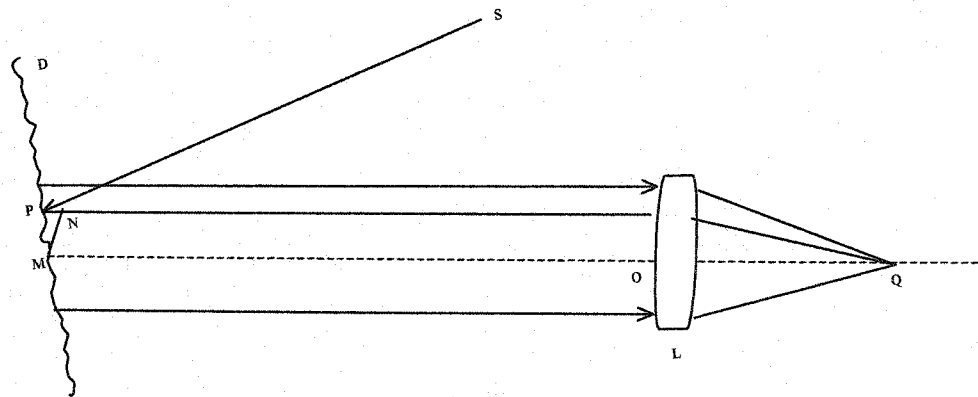
Figure-2.6: The optical path of a ray in subjective speckle: focal plane viewing.
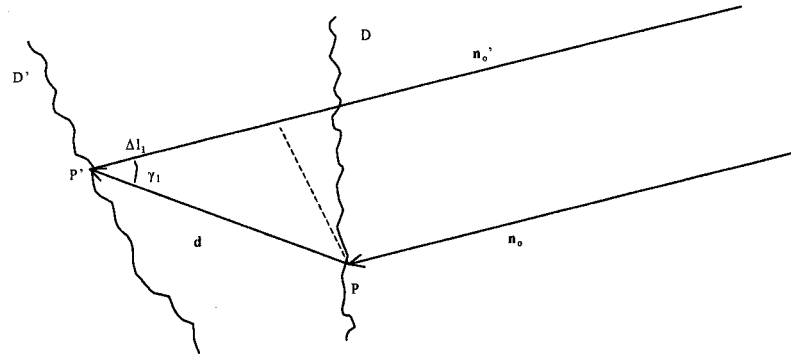
Figure-2.7: The ray geometry for the calculation of the phase difference between the illuminating wavefronts introduced by a surface displacement d.
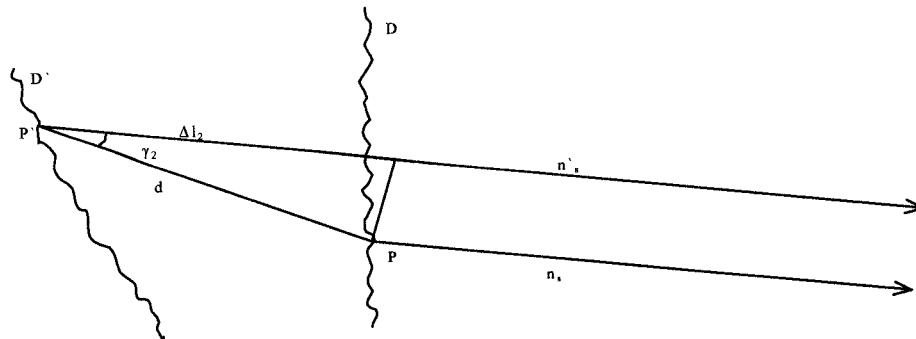
Figure-2.8: The ray geometry for the calculation of the phase difference between the scattered wavefronts introduced by a surface displacement d.

Thus the total phase change due to the displacement is given by

$$\varphi = \frac{2\pi}{\lambda}(n_o - n_s) \cdot d \qquad\qquad (2.18)$$

2.3 Electronic Speckle Pattern Interferometry (ESPI)

2.3.1 What is ESPI?

In speckle pattern interferometry a fringe pattern is derived from an optically rough surface observed in its original and displaced positions. The minimum speckle size is typically in the range of 5 to 100μm[1] and a standard video camera may be used to record the pattern. This method is known as Electronic Speckle Pattern Interferometry (ESPI) and was first demonstrated by Butters and Leendertz[3]. Similar work has since been described by Biedermann *et al.*[4] and Løkberg[5] *et. al.* The major feature of ESPI is that it enables real-time correlation fringes to be displayed directly upon a monitor without recourse to any form of photographic processing, plate relocation etc. This comparative ease of operation allows the technique of speckle pattern correlation interferometry to be extended to considerably more complex problems of shape measurement and deformation analysis. In the following sections different methods of correlation fringe formation, and their limitations and applications have been highlighted.

2.3.2 Fringe Formation by Signal Subtraction

The faceplate of the camera that is used to grab the images is located in the image plane of the speckle interferometer. In the subtraction method, the output signal from the camera with the object in its initial state is recorded. The object is then displaced and the camera signal is subtracted electronically from the stored signal. This process was carried out in the pre-digital age and hence was accomplished completely with analog electronics. Those areas of the two images where the speckle pattern remains correlated

will give a resultant signal of zero, while the uncorrelated areas will give non-zero signals. If the sum of the intensities of the incident waves are Φ_1 and Φ_2 just before and after the displacements then

$$\Phi_1 = I_1 + I_2 + 2\sqrt{I_1 I_2}\, \cos\psi \tag{2.19}$$

and

$$\Phi_2 = I_1 + I_2 + 2\sqrt{I_1 I_2}\, \cos(\psi + \Delta\varphi) \tag{2.20}$$

where I_1 and I_2 are the intensities of the individual waves, ψ is the difference in phase and $\Delta\varphi$ is the change in phase due to deformation[1].

If the output camera signals V_1 and V_2 are linearly proportional to the input image intensities, then the subtracted signal is given by

$$V_s = (V_1 - V_2) \propto (\Phi_1 - \Phi_2) = 2\sqrt{I_1 I_2}\left[\cos\psi - \cos(\psi + \Delta\varphi)\right]$$

or $\quad$
$$V_s = 4\sqrt{I_1 I_2}\, \sin(\psi + \Delta\varphi)\sin\frac{1}{2}\Delta\varphi \tag{2.21}$$

This signal has positive and negative values depending on the phase term. The monitor will display the negative-going signals as areas of blackness; to avoid this loss of signal, V_s is rectified before being displayed on the monitor. The brightness B on the monitor is then proportional to $|V_s|$, and given by

$$B = 4K\left[I_1 I_2 \sin^2\left(\psi + \frac{1}{2}\Delta\varphi\right)\sin^2\frac{1}{2}\Delta\varphi\right]^{\frac{1}{2}} \tag{2.22}$$

where K is a constant.

If the brightness B is averaged along a line of constant $\Delta\varphi$, the maximum and minimum values of it that comes out are

$$B_{max} = 2K\sqrt{I_1 I_2}, \text{ when } \Delta\varphi = (2n+1)\pi, \quad n\text{=}0,1,2.... \tag{2.23}$$

and

$$B_{min} = 0, \quad \text{ when } \Delta\varphi = 2n\pi, \quad n\text{=}0,1,2.... \tag{2.24}$$

These alternate maxima and minima gives rise to the fringe pattern. In Fig.2.9, subtraction correlation fringes are shown.

2.3.3 Fringe Formation by Signal Addition

Contrary to the signal subtraction, in this case the two signals obtained before and after the deformation are added together on the camera faceplate. The camera output voltage is proportional to the added intensities. The areas of maximum correlation have maximum speckle contrast and, as the correlation decreases, the speckle contrast falls. It reduces to a minimum but non-zero value where the patterns are uncorrelated. The voltage V_a is given by[1]

$$V_a \propto (\Phi_1 + \Phi_2) = 2I_1 + 2I_2 + 4\sqrt{I_1 I_2}\cos\left(\psi + \frac{1}{2}\Delta\varphi\right)\cos\frac{1}{2}\Delta\varphi \qquad (2.25)$$

The contrast of the speckle pattern can be defined as the standard deviation of the intensity. For a line of constant $\Delta\varphi$, this is

$$\sigma_{12} = 2\left[\sigma_1^2 + \sigma_2^2 + 8\langle I_1\rangle\langle I_2\rangle\cos^2\frac{1}{2}\Delta\varphi\right]^{\frac{1}{2}} \qquad (2.26)$$

where σ_1 and σ_2 are the standard deviations of I_1 and I_2. The contrast varies between maximum and minimum values given by

$$[\sigma_{12}]_{\max} = 2[\sigma_1^2 + \sigma_2^2 + 2I_1 I_2]^{\frac{1}{2}}, \quad \text{when } \Delta\varphi = 2n\pi, \quad n=0,1,2.... \qquad (2.27)$$

and

$$[\sigma_{12}]_{\min} = 2[\sigma_1^2 + \sigma_2^2]^{\frac{1}{2}}, \qquad \text{when } \Delta\varphi = (2n+1)\pi, \quad n=0,1,2.... \qquad (2.28)$$

while the contrast of the added intensities varies the mean value along a line of constant $\Delta\varphi$ is the same for all $\Delta\varphi$ and is given by

$$\langle \Phi_1 + \Phi_2\rangle = 2\langle I_1\rangle + 2\langle I_2\rangle \qquad (2.29)$$

when the sum of the two speckle patterns is directly displayed on the monitor, the average intensity remains constant, and the variation in correlation is shown as a variation in the contrast of the speckle pattern but not in its intensity. This technique is employed to observe the time-averaged vibration fringes. The correlation fringe pattern is shown in Fig.2.10. Subtraction fringes have intrinsically better visibility than addition fringes since the minima have zero intensity.
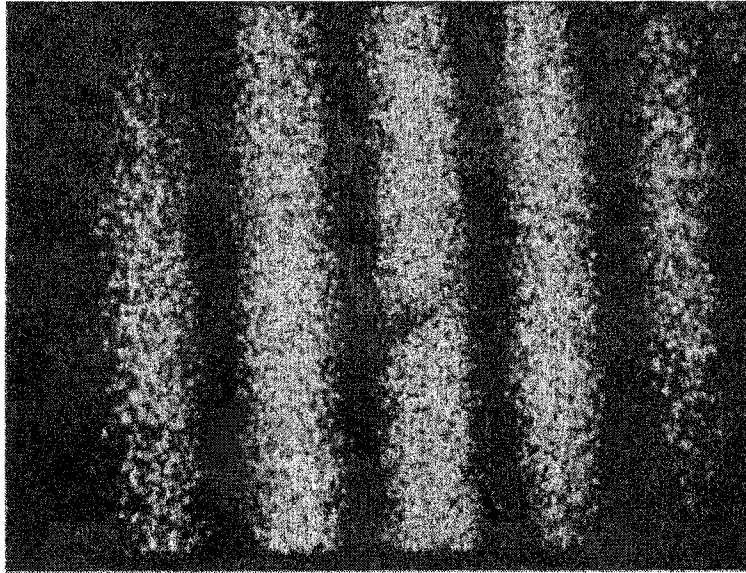
Figure-2.9: Sin^2 speckle pattern correlation fringes obtained using electronic subtraction [Taken from Ref. 1 with kind permission of Dr. R. Jones, p.169].
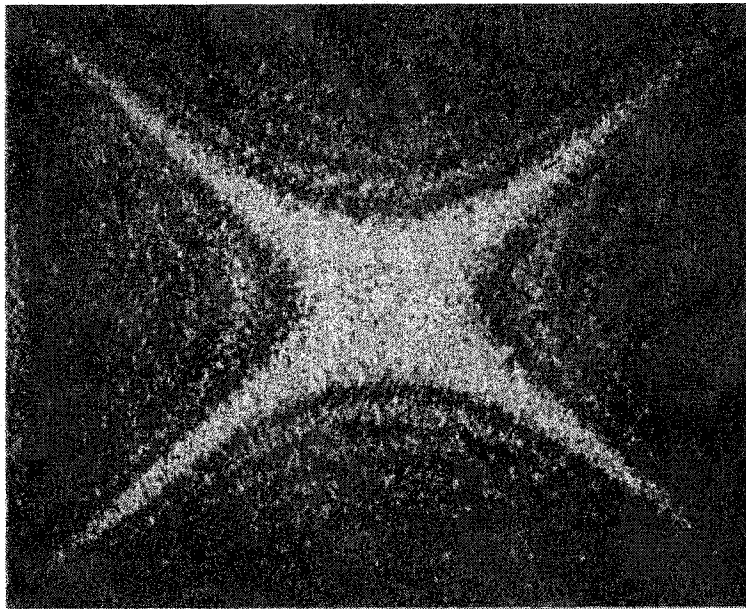
Figure-2.10:   Speckle pattern correlation fringes obtained using electronic addition. The sample was excited by a small piezo-electric crystal attached to its rear [Taken from Ref. 1 with kind permission of Dr. R. Jones, p.172].

Chapter 2.   Speckle Interferometry

2.3.4   Fringe Formation by Direct Correlation

This is an alternative and recently developed method of directly correlating digitally acquired speckle patterns[6]. This method requires more calculations than the standard methods described earlier but the main advantage is that it produces substantial fringe contrast irrespective of the illumination level over the sample surface. Further, the values output in this method are directly related to a wrapped phase value from Eq.2.18.

This method is based on the correlation coefficient between the added intensities Φ_1 and Φ_2 before and after the deformation irrespectively. The correlation coefficient of two random variables X and Y is defined as[7]

$$\rho_{XY} = \frac{\langle XY \rangle - \langle X \rangle \langle Y \rangle}{\sigma_X \sigma_Y} \tag{2.30}$$

where

$$\sigma_X = \left(\langle X^2 \rangle - \langle X \rangle^2 \right)^{\frac{1}{2}}, \qquad \text{and} \qquad \sigma_Y = \left(\langle Y^2 \rangle - \langle Y \rangle^2 \right)^{\frac{1}{2}}$$

If X and Y are independent then

$$\langle XY \rangle = \langle X \rangle \langle Y \rangle \tag{2.31}$$

In this case ρ_{XY} will be zero.

Recall Φ_1 and Φ_2, which are defined in equations (2.19) and (2.20) as

$$\Phi_1 = I_1 + I_2 + 2\sqrt{I_1 I_2} \, \cos \psi$$

and

$$\Phi_2 = I_1 + I_2 + 2\sqrt{I_1 I_2} \, \cos(\psi + \Delta\varphi)$$

Now consider only a small area of the surface of the object such that over this area $\Delta\varphi_c$ in nearly uniform. Then the correlation co-efficient between the intensities over this small area will be

$$\rho(\Delta\varphi_c) = \frac{\langle \Phi_1 \Phi_2 \rangle - \langle \Phi_1 \rangle \langle \Phi_2 \rangle}{\left(\langle \Phi_1^2 \rangle - \langle \Phi_1 \rangle^2 \right)^{\frac{1}{2}} \left(\langle \Phi_2^2 \rangle - \langle \Phi_2 \rangle^2 \right)^{\frac{1}{2}}} \tag{2.32}$$

This can be further evaluated by noting that:

(i) I_1, I_2 and ψ are independent variables and can be averaged separately.

(ii) $\langle \cos \psi \rangle = \langle \cos(\psi + \Delta\varphi) \rangle = 0$ (i.e., the average value of the cosine function is zero.) and

(iii) $\langle I^2 \rangle = 2 \langle I \rangle^2$

and assuming $\langle I_1 \rangle = \langle I_2 \rangle = \langle I \rangle$, gives

$$\rho(\Delta\varphi) = \frac{1}{2}(1 + \cos \Delta\varphi) \tag{2.33}$$

Thus the correlation is unity when $\Delta\varphi = 2n\pi$, and zero when $\Delta\varphi = (2n+1)\pi$. This shows the direct relation between the change in the phase $\Delta\varphi$ introduced by the motion and the correlation co-efficient calculated from the local intensities in the two images. The direct correlation method is based on the results of equations (2.32) and (2.33) that the correlation coefficient between two speckle patterns is modulated with a cosine dependence on the change in the phase $\Delta\varphi$ due to the displacement. Consider A_{ij} and B_{ij} are the pixel intensities of two digitally recorded complete speckle patterns, where i and j represents individual speckle positions within the images and each pixel represents on average the intensity of each speckle. Now under sufficiently small displacements so that the speckle de-correlation effect[8] can be neglected, and over suitably small spatially corresponding sets of m adjacent pixels a_k and b_k, the change in the phase $\Delta\varphi$ can be assumed to be nearly constant, the discrete local correlation coefficient r between these two cells and analogous to equation (2.32) is given by[6]

$$r = \frac{\frac{1}{m}\sum_{}^{m}(a_{k1}b_{k1}) - \left[\frac{1}{m}\sum_{}^{m}(a_{k1})\right]\left[\frac{1}{m}\sum_{}^{m}(b_{k1})\right]}{\sigma_a \sigma_b} \tag{2.34}$$

where

$$\sigma_a = \left\{\frac{1}{m}\sum_{}^{m}(a_{k1}^2) - \left[\frac{1}{m}\sum_{}^{m}(a_{k1})\right]^2\right\}^{\frac{1}{2}} \tag{2.35}$$

with the corresponding formula for σ_b. This is Pearson's coefficient of correlation for finite discrete sets of data. Here its taken to be a local approximation to the coefficient of correlation in equation (2.32). In the analysis, square cells of desired size are selected
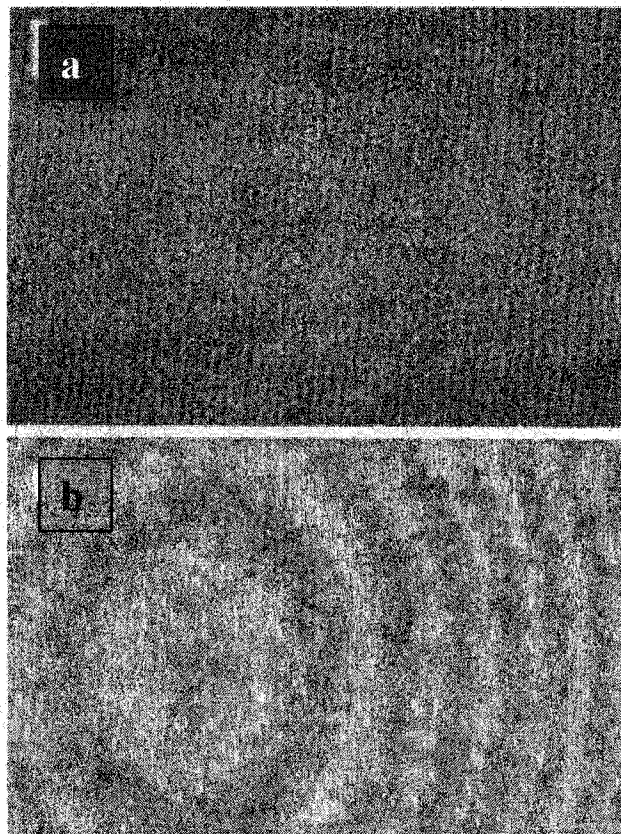
Figure-2.11: Speckle pattern correlation fringes obtained from the same raw frames by a) subtraction method and b) direct correlation[9] method [Taken from Ref. 6 with kind permission of Dr. D.R. Schmitt, p.8850].

and the calculation of equation (2.34) is carried out systematically over each possible set of cells. The mapping of these calculated r values then forms the fringe pattern. An example of fringe pattern by direct correlation is shown in Fig.2.11.

As suggested in Eq. (2.34), when the in-phase condition exists, *r* approaches unity, indicating good positive correlation. For the out-of-phase condition, *r* approaches zero, indicating no correlation. It is important to note that *r* values less than zero are possible with Eq. (2.34) but should not exist according to Eq. (2.33). Such values represent a negative correlation between the pixel intensities within the two cells. In the present context a negative correlation has the same meaning as no correlation and is assigned a value of zero.

2.3.5   Applications and Limitations of ESPI

Speckle interferometry has a wide range of applications in the field of engineering, medicine and botany mainly because of its non-invasive approach. It is beyond the scope of this section to discuss all of them here. However, only the main applications of ESPI will be highlighted in the following section.

Non-destructive testing (NDT):   Interferometric methods are suitable for their non-contacting character and can measure surface displacements that result from the application of very small loads. In NDT it is used to detect whether or not a material has a fault within without damaging it. The discontinuity appears as an irregularity in the fringe pattern and enables the region of fault to be identified. The surface displacement is generally created by mechanical loading, heating, hydrostatic pressure or vacuum or vibration. The major limitations in this process are that the defect has to be made to create a discontinuity in the surface displacement and comparable to the minimum fringe spacing to be able to make any appreciable effect on the overall fringe geometry. When these limitations are taken into account, ESPI becomes one of the most successfully applied techniques in detection of debonds in tires and composite materials like carbon fibre reinforced polymer (CFRP) or metal clad honeycomb structures[1].
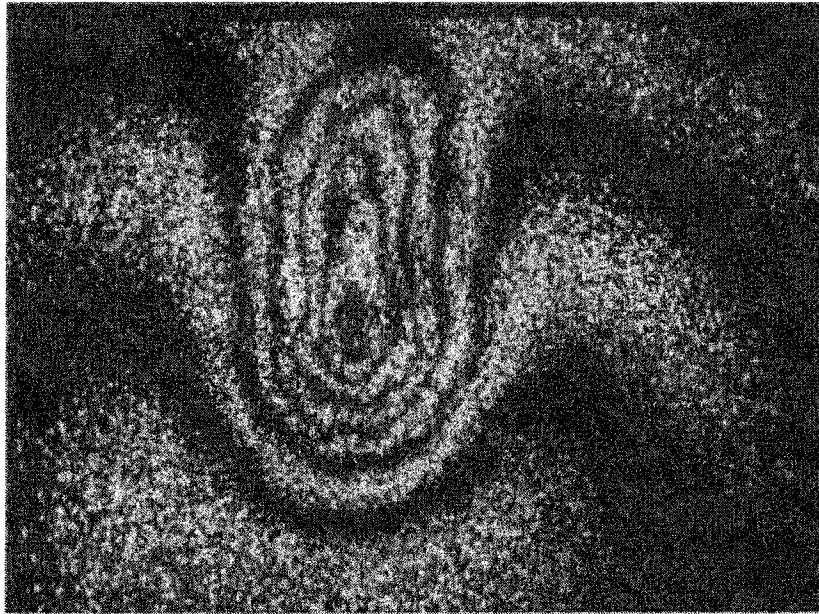
Figure-2.12: Out of plane displacement ESPI fringes which indicate a region of debond between a CFRP outer cladding and an internal honeycomb structure [Taken from Ref. 1 with kind permission of Dr. R. Jones, Page.278].
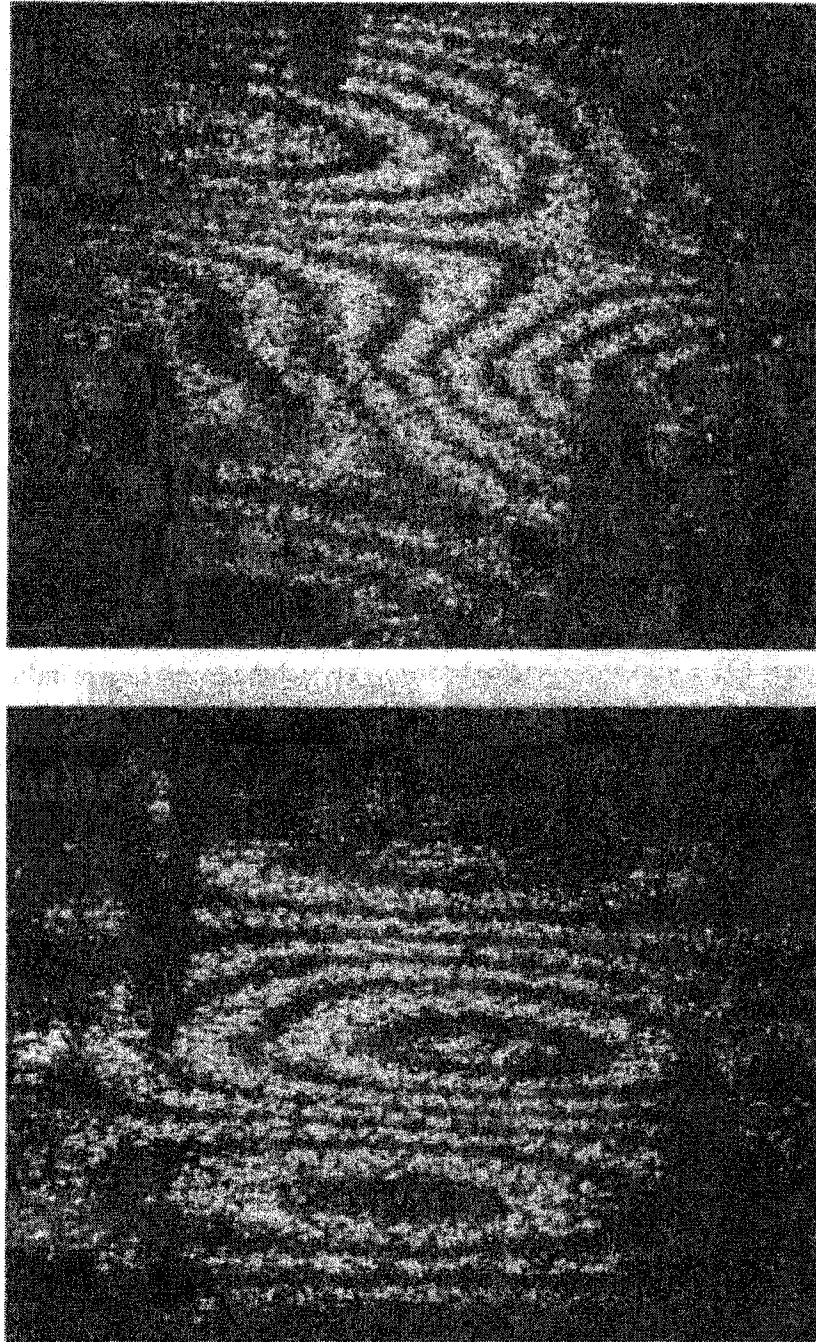
Figure-2.13: The out of plane displacement distribution in the vicinity of a (a) known good weld and (b) known cold weld using ESPI [Taken from Ref. 1 with kind permission of Dr. R. Jones, p.279].

Fig.2.12 demonstrates the way in which debonds between the honeycomb and the CFRP cladding are revealed under vacuum. The region of high density fringes corresponds to the faulted zone.

Another example of NDT application is to inspect the quality of strip welds formed between thin ($\approx$0.1 mm thick) metallic sections. The electronic speckle interferogram shown in Fig.2.13 shows fringe patterns in the vicinity of a known good weld made under optimum heating conditions and in the vicinity of known poor weld formed under 'cold' conditions. There is a clear difference between the two interferograms.

Component inspection and quality control: By virtue of the resolution and accuracy attainable in interferometric methods, it is used to control and monitor the dimensional tolerance of production components. Moreover ESPI is used to detect the shape differences between a master and production components of complex geometry[1]. This is a problem of considerable commercial importance since improvements in the accuracy of the blades help to reduce the fuel consumption of the engine as well as increasing the level of performance. Two parameters have been measured:

    i.   the accuracy to which the profile of the manufactured blade follows that of the design and

    ii.   orientation of the blade relative to a defined axis usually called the stacking axis.

The technique requires that a blade of known dimension be used as a master for the manufacture of the fringe. At the fringe observation stage the master blade is removed and replaced by nominally identical production blade and fringe is formed. The purpose of this analysis is to identify the coordinate of the fringe centres and perform the computations necessary to transform them to a plot of shape difference. Fig.2.14 shows ESPI fringes at a contour sensitivity of 25μm that have been identified and redisplayed on the monitor. They correspond to the difference between the form of a production blade and master.

Experimental engineering design investigation: Interferometric fringes have higher fringe density in regions of a structure where strain concentrations are present. Moreover, fringe irregularities show up in the regions of uneven load

distribution. This information may be used in the experimental study of prototype designs and investigate sources of failure due to stress concentration[1].

Static displacements and strain determination: Interferometric fringes are formed due to the surface displacements and this strain information is embedded in the fringe patterns. This method therefore provides a powerful tool for experimental strain analysis, a fact that has been exploited by a considerable number of workers[9].

Among many other applications of ESPI, one is to measure the elastic moduli of materials and that is the aim of this present research. This is of considerable importance in the fields of Geophysics and Engineering.

Figure-2.14: 25μm sensitivity ESPI contour fringes defining the difference between a section of master turbine blade and inspection blade. The position of these fringes had been identified and enhanced by computer analysis[1] [Taken from Ref. 1 with kind permission of Dr. R. Jones, p.292].

References:

1. R. Jones and C. Wykes, *Holographic and Speckle Interferometry*, Cambridge University Press, Cambridge, UK, 1983.

2. J. W. Goodman, *In Laser Speckle and Related Phenomena*, Chapter 2, ed. J. C. Dainty, Springer-Verlag: Berlin, 1975.

3. J. N. Butters and J. A. Leendertz, *Journal of Measurement and Control,* 4, pp.344-350, 1971.

4. K. Biedermann and L. Ek, *K. Phys. E: Scientific Instruments,* 8, pp.571-576, 1975.

5. O. J. Løkberg and K. Høgmoen, *Vibration phase mapping using electronic speckle pattern interferometry, Appl. Opt.,* 15, pp.2701-2704, 1976.

6. D. R. Schmitt and R. W. Hunt, *Optimization of fringe pattern calculation with direct correlations in speckle interferometry, Applied Optics,* Vol.36. No. 34. pp.8848-8857, 1997.

7. R. Jones and C. Wykes, *Holographic and Speckle Interferometry,* pp. 310-311, Cambridge University Press, Cambridge, UK, 1983.

8. R. Jones and C. Wykes, *De-correlation effects in speckle-pattern interferometry,* and *Displacement dependent de-correlation and applications to the observation of machine-induced strain, Opt. Acta.,* 24. pp.533-550, 1977.

9. Contributions by various authors, *Journal of Strain Analysis,* 9, No.1. 1974.

Chapter 3

Determination of Elastic Coefficients Using Boussinesq' Theory

3.1 Introduction

Over the last couple of decades Electronic Speckle Pattern Interferometry[1] (ESPI) has become popular for deformation analysis together with the Holographic Interferometry[1,2]. ESPI provides measures of displacement through slight changes in successive video images. The raw recorded data consist of a fringe pattern representing variations in the phase of the coherent laser used, which in turn depends on the magnitude and the direction of the motion of the object under study. So the fringe pattern is a map of the changes in the phase of the light over the surface of the object due to small displacements introduced by exerting some amount of force between the exposures. The surface displacement, introduced by a normal force, depends directly on the materials elastic coefficients. Consequently, a raw fringe pattern provides some measure of not only the surface displacement but also the elastic properties like Young's modulus and Poisson ratio. However, inverting this fringe pattern is complicated due to the fact that the fringe order number n is not directly yielded. This is resolved here using an iterative Least Square Minimization method.

In this chapter a methodology to measure the static elastic properties of an isotropic material by placing a known point load on the material surface is described. In section-3.2, the analytical treatment of fringe formation and inversion is described. In section-3.3, a forward model fringe pattern is calculated using the Boussinesq' theory[3] of surface displacement under a normal force. This fringe pattern is then inverted using the least square minimization method. The purpose of this virtual experiment is to deduce what problems might be encountered in the analysis of such fringe patterns. Also an

error analysis is carried out in this section. The experimental set up is described in section-3.4. Eventually in section-3.5, this method is applied to experimental fringes to find out the Young's modulus and Poisson ratio of the material under investigation.

3.2 Analysis Methodology

The surface displacements on an isotropic elastic half-space subjected to a normal point load [Boussinesq theory] is given in the Cartesian coordinate system as[3,4]

$$u_x = \frac{-F(1-2v)(1+v)X}{2\pi E(X^2 + Y^2)} \qquad (3.1)$$

$$u_y = \frac{-F(1-2v)(1+v)Y}{2\pi E(X^2 + Y^2)} \qquad (3.2)$$

and

$$u_z = \frac{F(1-v^2)}{\pi E(X^2 + Y^2)^{\frac{1}{2}}} \qquad (3.3)$$

where F is the normal force, E is the Young's modulus and v is the Poisson ratio. u_x, u_y and u_z are displacements in X, Y and Z directions respectively. The relationship between the origin O, point of force application P and a displaced point D on the surface of the material is shown in Fig.3.1.

The ESPI that has been employed in this work has two coherent laser beams made out of one single laser source using a beam splitter. The geometry is shown in Fig.3.2. When a certain force is introduced at a point on the surface under investigation, the speckle pattern changes cyclically with respect to the magnitude and direction of the displacement and the position of each point P(x,y,z) relative to the sources as represented by unit vectors n_1 and n_2. The change between the speckle patterns taken immediately before and after the displacement is given in terms of a change in phase given by[1]

$$\varphi(x, y, z) = \frac{2\pi}{\lambda} \left[n_1(x, y, z) - n_2(x, y, z) \right] \cdot U(x, y, z) \qquad (3.4)$$
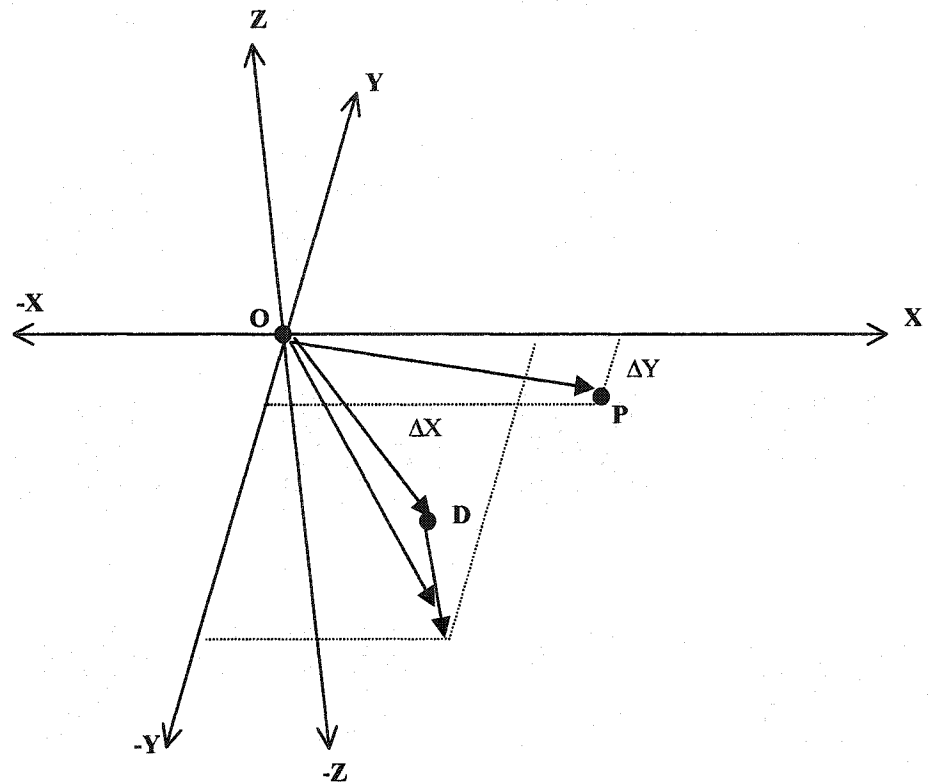
Figure-3.1: Normal force is applied at P. The relationship of a point on the surface D and the force point P with the origin O is shown.
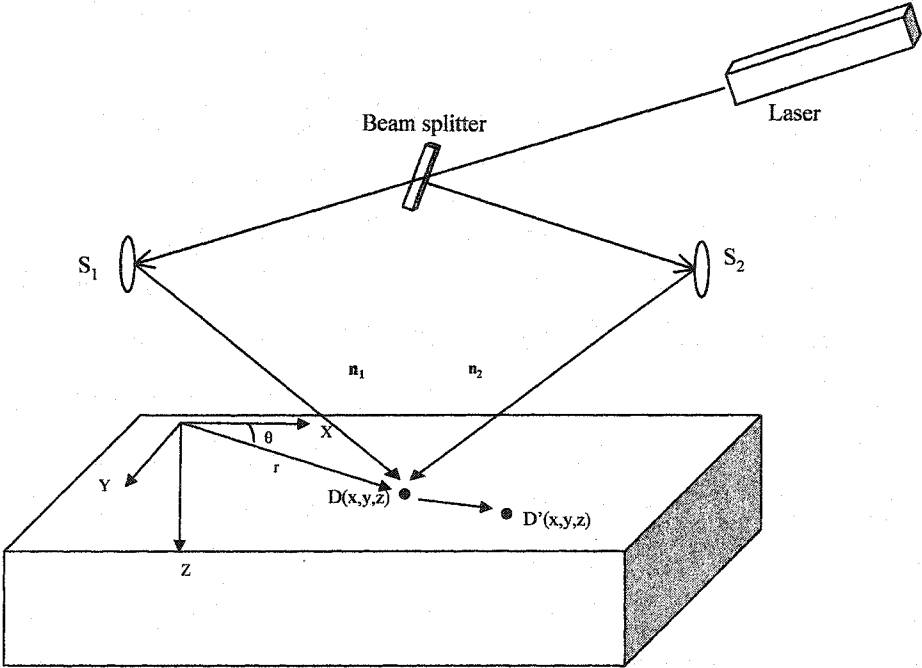
Figure-3.2: The geometry of the dual-beam interferometer.

writing $\quad \frac{2\pi}{\lambda}\left[n_1(x,y,z) - n_2(x,y,z)\right] = k(x,y,z) \quad$ gives

$$\varphi(x,y,z) = k(x,y,z) \cdot U(x,y,z) \tag{3.5}$$

where $K(x,y,z)$ is the sensitivity vector. The fringe intensity ρ in terms of φ is [from Eq. (2.33)]

$$\rho(x,y,z) = \frac{1}{2}\left(1 + \cos\varphi(x,y,z)\right) \tag{3.6}$$

which gives a maximum fringe intensity when

$$\varphi = 2n\pi \tag{3.7}$$

where n is an integer and is called the fringe order. Equations (3.4) and (3.6) have been used to model the fringe patterns. Details are given in Appendix B.

To determine the best values of Young's modulus E and Poisson ratio v from the picked fringe positions of images, an iterative minimum error procedure has been employed[5]. The method assumes that the character of the displacements due to a known load on the sample surface is known and can be modelled analytically. For a point on such surface, the displacement is

$$U(x,y,z) = u_1\mathbf{i} + u_2\mathbf{j} + u_3\mathbf{k} \tag{3.8}$$

where $\mathbf{i}$, $\mathbf{j}$ and $\mathbf{k}$ are the unit directional vectors in the x, y and z directions respectively, and u_1, u_2 and u_3 are the corresponding unknown components of the displacement magnitude. The relation between the fringe order and the displacement can be found from Equations (3.5) and (3.7) as

$$n(x,y,z) = \frac{1}{2\pi}\left(\mathbf{k}(x,y,z) \cdot U(x,y,z)\right) \tag{3.9}$$

As the first step towards inversion, first a number of points are selected at the peak of a bright fringe. As they come from the same fringe, they all share the same fringe order. An arbitrary and of course temporary trial fringe order value n is assigned to this set of points. Next, points on the trough of the next (independent of direction) dark fringe are picked and successively given a fringe order value of $(n-1/2)$. At the next bright fringe (following the same direction), the fringe peak will have a fringe value of $n-1$. This process is progressively repeated with successive fringe peaks and troughs. Note that some judgement may need to be exercised here and the researcher may need to carry

out some forward modelling to obtain a starting estimate. Eventually, a series of equations are developed which is given as

$$
\begin{bmatrix} n \\ \cdot \\ \cdot \\ n \\ n-1/2 \\ \cdot \\ \cdot \\ n-1/2 \\ n-1 \\ \cdot \\ \cdot \end{bmatrix} = \frac{1}{2\pi} \begin{bmatrix} k_x{}^1 & k_y{}^1 & k_z{}^1 \\ & \cdot & \\ & \cdot & \\ k_x{}^j & k_y{}^j & k_z{}^j \\ k_x{}^{j+1} & k_y{}^{j+1} & k_z{}^{j+1} \\ & \cdot & \\ & \cdot & \\ k_x{}^k & k_y{}^k & k_z{}^k \\ k_x{}^{k+1} & k_y{}^{k+1} & k_z{}^{k+1} \\ & \cdot & \\ & \cdot & \end{bmatrix} \cdot \begin{bmatrix} u_1 \\ u_2 \\ u_3 \end{bmatrix}
$$

(3.10)

Substituting the displacement values from Eq.3.1, 3.2 and 3.3 into Eq.3.10 and after some rearrangements, one can write

$$
\begin{bmatrix} n \\ \cdot \\ \cdot \\ n \\ n-1/2 \\ \cdot \\ \cdot \\ n-1/2 \\ n-1 \\ \cdot \\ \cdot \end{bmatrix} = \begin{bmatrix} A_1 & B_1 \\ A_2 & B_2 \\ \cdot & \cdot \\ \cdot & \cdot \\ \cdot & \cdot \\ \cdot & \cdot \\ \cdot & \cdot \\ \cdot & \cdot \\ \cdot & \cdot \\ A_{i-1} & B_{i-1} \\ A_i & B_i \end{bmatrix} \begin{bmatrix} \alpha \\ \beta \end{bmatrix}
$$

(3.11)

where i is the total number of picked points. A, B, α, β are given as

$$A = \frac{k_x}{4\pi^2}\left(\frac{-FX}{\left(X^2+Y^2\right)}\right) + \frac{k_y}{4\pi^2}\left(\frac{-FY}{\left(X^2+Y^2\right)}\right) \qquad (3.12.\text{a})$$

$$B = \frac{k_z}{2\pi^2}\left(\frac{F}{\left(X^2+Y^2\right)^{\frac{1}{2}}}\right) \qquad (3.12.\text{b})$$

$$\alpha = \frac{\left(1-2v\right)\left(1+v\right)}{E} \qquad (3.13.\text{a})$$

and

$$\beta = \frac{\left(1-v^2\right)}{E} \qquad (3.13.\text{b})$$

Details of this derivation are given in Appendix B.

Equation (3.11) may be written in matrix notation as

$$N = GM \qquad (3.14)$$

where $G = [A\ B]$ and $M = [\alpha\ \beta]^T$. In Equation (3.11), the arbitrary assigned value of n may be wrong but the vector components A_1, A_2..., B_1, B_2... are known for each particular picked points form the source geometry S_1 and S_2 and the picked points positions. The values of the elastic coefficients E and v, embedded in M, are still unknown but can be determined from Eq.(3.14) using the well known Least Square Minimization method to obtain a trial solution of the form

$$M = (G^T G)^{-1} G^T N \qquad (3.15)$$

from which a fringe order error value $F_{error} = |N\text{-}GM|^2$ is calculated. The entire procedure is then repeated by incrementing or decrementing the fringe order values in n by unity and again solving for a new trial M and corresponding fringe order error by least squares. The procedure iterates until a minimum error is detected. The fringe order assignment for this minimum error is most correct and will provide, in the least-square's sense, the best value of M for determination of E and v. The Young's modulus E and Poisson ratio v are calculated using Eqs.(3.13) with the following relation

$$M = \begin{bmatrix} \alpha \\ \beta \end{bmatrix} \qquad (3.16)$$

In the following sections this procedure is first tested on artificially calculated fringe patterns and then applied to real experimental fringe patterns.

3.3   Forward Modelling and Inversion

In the following sections, first a forward modelled fringe pattern is calculated by substituting Boussinesq's displacement Eqs.(3.1), (3.2) and (3.3) into Eqs.(3.4) and (3.6). Then this synthetic fringe pattern is directly inverted using the least square minimization method [Eq.(3.15)] to get back the Young's modulus E and Poisson ratio v of the material. An effort is taken to find the possible sources of errors during the inversion. Noise is added to the noise free synthetic data and it is inverted again to show the possible differences between the noisy and noise free cases.

Synthetic fringe creation: The synthetic fringe pattern in Fig.3.3 is created by applying 1500N force on a Plexiglas block with Young's modulus E = 3GPa (E = 3E9 N/m^2), and Poisson's ratio v = 0.45. The surface of the block (which is the x-y plane) is assumed to be illuminated by two coherent laser sources $S_1(x,y,z)$ and $S_2(x,y,z)$. The input parameters used are given in the following table.

Table-3.1:   Input parameters used to create Fig.-3.3.

Viewing Area (cm)	Force application point. (x-y)	Force on the block	Sources positions (x,y,z) in cm	Laser wavelength (nm)	E (GPa)	Poisson ratio
19.4x 14.3	X=9.5 Y=3.2	1500N	S_1 (-4.6, 7.0, -5.3) S_2 (23.5, 7.3, -6.3)	829	3.0	0.45

Inversion of synthetic fringe pattern: The fringe pattern of Fig.3.3 is inverted to get the E and v values by the fringe picking method which applies least square minimization as described in the earlier section. To provide input to the inversion, points were manually picked along the bright and dark fringes. A window of size 11x11 pixels was delineated around each picked points. This was used to make sure
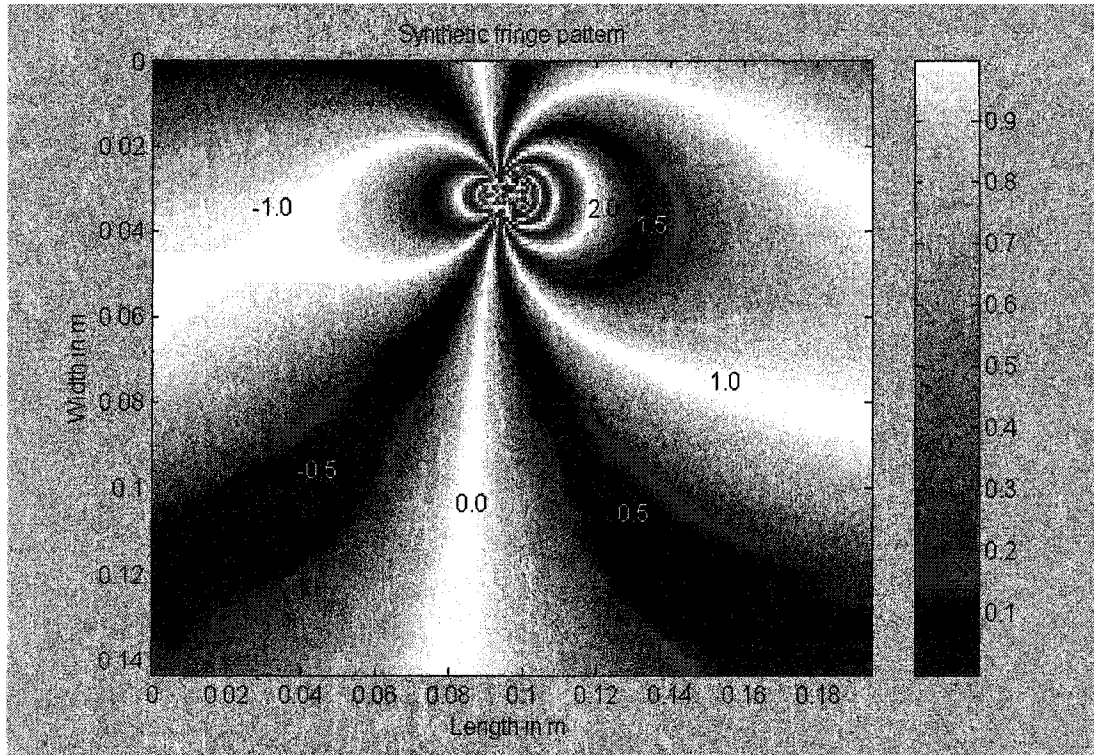
Figure-3.3: Noise free synthetic fringe pattern. The orders of the fringes are set from the results of the minimization curve (Fig.3.4).

that even if a picked point is not at the maxima or minima (central part of the respective fringes), the code creates a window all around that picked point and finds the desired maximum or minimum number within it. This gives a better result with synthetic noise free images. Window size has to be carefully chosen since a window of wrong size might bring the next fringe into consideration, resulting a bad output (especially when the fringes are closely spaced near force point). One of the minimization curves is shown in Fig.3.4 and the results are given in Table-3.2.

Table –3.2: Results from inversion of the image in Fig.3.3.

Trial No.	Fringes picked	No. of Points picked	Win. length	E in GPa	Poisson ratio v	Least sq.error	% Error in E	% Error in v	Comments
1		106		3.0343	0.4504	0.0020	1.14	0.08	Fringes have been picked starting from right side and going through all the fringes and ending at the left. The whole process can be done in the opposite direction.
2		121		3.0136	0.4510	0.0017	0.45	0.22	
3		126		3.0350	0.4504	0.0020	1.16	0.08	
4		121		3.0347	0.4505	0.0034	1.15	0.11	
5		116		3.0272	0.4506	0.0027	0.90	0.13	
6		109		3.0082	0.4511	0.0025	0.27	0.24	
7	8	121	11x11	3.0317	0.4505	0.0017	1.05	0.11	
8		117		3.0025	0.4513	0.0024	0.08	0.28	
9		123		2.9957	0.4514	0.0027	0.14	0.31	
10		121		3.0290	0.4499	0.0314	0.96	0.02	
11		126		3.0471	0.4493	0.0380	1.57	0.15	
12		121		3.0284	0.4499	0.0332	0.94	0.02	
13		116		3.0459	0.4493	0.0340	1.53	0.15	
Direct Inv.	-	-	-	2.9999	0.4500	0.0088	0.003	0.0	Small amount of error present due to the numeric

One important question in the inversion is, what would be the error just due to numerics (occurs due to the limitations of the computer) and error due to numerics in picking. To verify this, the same data set is inverted directly. At first the values of fringe order *n* for every pixel point is calculated using Eq.(3.7). This is then used as input into

The minimization curve from the inversion is shown below.
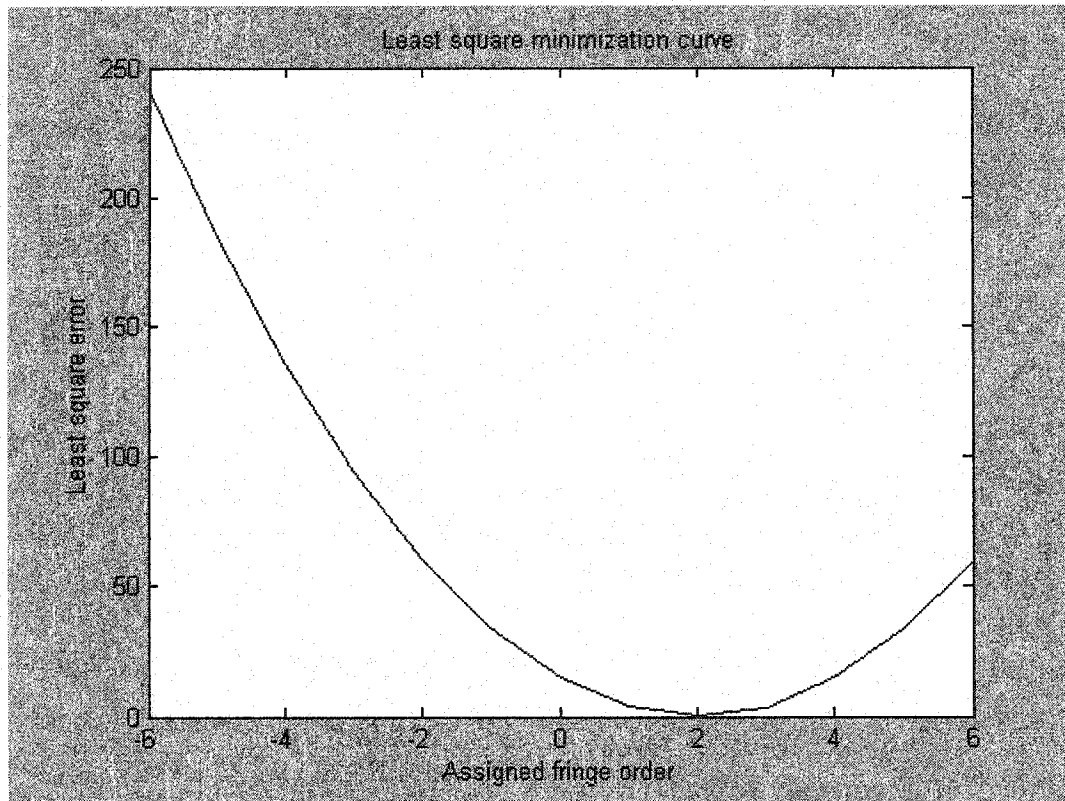
Figure 3.4: Least square minimization curve shows that the fringe order of the first picked fringe is 2. Curves from other trials showed the same result.

Eq.(3.11) to obtain the E and ν values. The unwrapped phase value φ, and A and B values are the same as obtained from the forward modelling. As is seen from the last row of Table-3.2, the values of E and ν obtained in this way are almost same as the input values (3GPa and 0.45 respectively) but still there is a little insignificant difference present. This error arises due to the numerics and the fact that the pixel values will never be truly 0 or 1 in reality.

Identifying the sensitive parameters: In the above virtual inversion, the input parameters such as the positions of the sources or the force application point are exactly the same as used in the forward model [Table-3.1]. In a real test, it might not be possible to determine these parameters accurately and this will result in some unavoidable error. In the following section, the input parameters for the inversion will be slightly changed from their exact values one at a time in order to assess their vulnerability. To do this, first the fringe pattern of Fig.3.3 has been inverted once again using the parameters of Table-3.1 as input (this result is given in row 1 of Table-3.3). The co-ordinates of the picked points, the assigned fringe orders and the total number of picked points have been saved and subsequently used in the later inversions where only the input parameters are gradually changed. This keeps the consistency between different inversions. The percentage of error has been calculated from the first result relative to the later ones.

The degree of error that might be associated with a certain parameter is selected with some consideration of a real experimental arrangement, i.e., by estimating the amount of error that might exist in the experimental determination of those parameters. Accordingly,

- co-ordinates of the laser sources could be uncertain by as much as ±3mm (cumulative from both of the measuring ends) due to the complex positioning of the sources relative to the origin and difficulties associated with measuring points in 3-D space.

- The viewing area of the sample surface may vary by as much as three millimetres due to the cumulative effect of the errors in measurement

and cropping of the image area during the inversion. So error of ±3mm is assigned to its dimensions.

- The applied force gets an error of ±30N since according to the manufacturers specification of the load cell, at the peak force range of 1500N there might be 2% error associated with the reading.

- The co-ordinates of the force application point have been assigned an error value of about ±2mm, which again arises from the measurements.

It is evident from Table-3.3 that the co-ordinates of the point of force application (both x and y co-ordinates individually and combined as seen in rows 2,3and 4), x and z-coordinates of the first laser source S_1, z-coordinate of the second laser source S_2 and the length of the block are among the more sensitive parameters. These parameters individually have contributed more than 2% of error to each or both of the output values E and v. When many of these errors are considered together [except the force application point (row 22)], the output Young's modulus and Poisson ratio values resulted with 30% and 8% errors respectively, which is extremely high. When combined all together, these errors affect the results in some anomalous ways- in few cases their combined effect cuts down the amount of error in the out put (row 23, Table-3.3), but mostly it increases.

The summary of Table-3.3 is plotted in Fig.3.5. The upper bars show the errors associated with the Young's modulus when the parameter values have been increased from the actual values (by adding the error) and the lower bars show the errors when the parameter values have been decreased from the actual values. As seen from this figure, among the most vulnerable parameters are the; x-coordinate of the block dimension, co-ordinates of force points and the z-coordinate of the first source (S_1). To minimize the error with the result, these parameters should be measured most precisely and carefully during the experiment.

The situation with Poisson's ratio is similar to that shown in Fig.3.6, except the fact that the overall effect of errors on Poisson ratio is less than Young's modulus. This can be seen from the magnitude of percentage errors in Fig.3.6.

It is seen that the errors associated with different parameters affect the results asymmetrically, i.e., when the positive (+) error is added to the parameter it gives a

Table-3.3: Input parameters and the results from inversion. The values in bold italic were allowed to change during inversion.

Trial no.	Viewing area in cm	Force Point in cm	F. (N) x100	S_1 in cm x	S_1 in cm y	S_1 in cm z	S_2 in cm x	S_2 in cm y	S_2 in cm z	E GPa	% error in E	ν	% err. in ν
1	19.4x14.3	X=8.53 Y=2.70	15	-4.6	7.0	-5.3	23.5	7.3	-6.3	3.02	0.00	0.450	0.0
2	19.4x14.3	*X=8.35* Y=2.70	15	-4.6	7.0	-5.3	23.5	7.3	-6.3	3.14	3.77	0.443	1.5
3	19.4x14.3	X=8.53 *Y=2.52*	15	-4.6	7.0	-5.3	23.5	7.3	-6.3	2.86	5.34	0.454	0.9
4	19.4x14.3	*X=8.35* *Y=2.52*	15	-4.6	7.0	-5.3	23.5	7.3	-6.3	2.77	8.27	0.454	0.9
5	19.4x14.3	X=8.53 Y=2.70	*14.7 (±3)*	-4.6	7.0	-5.3	23.5	7.3	-6.3	2.96	2.00	0.450	0.0
6	19.4x14.3	X=8.53 Y=2.70	15	*-4.3*	7.0	-5.3	23.5	7.3	-6.3	3.11	2.79	0.445	1.1
7	19.4x14.3	X=8.53 Y=2.70	15	*-4.9*	7.0	-5.3	23.5	7.3	-6.3	2.97	1.70	0.454	0.8
8	19.4x14.3	X=8.53 Y=2.70	15	-4.6	*6.7*	-5.3	23.5	7.3	-6.3	3.05	0.96	0.449	0.3
9	19.4x14.3	X=8.53 Y=2.70	15	-4.6	*7.3*	-5.3	23.5	7.3	-6.3	2.99	0.90	0.451	0.3
10	19.4x14.3	X=8.53 Y=2.70	15	-4.6	7.0	*-5.0*	23.5	7.3	-6.3	3.01	0.58	0.457	1.6
11	19.4x14.3	X=8.53 Y=2.70	15	-4.6	7.0	*-5.6*	23.5	7.3	-6.3	3.28	8.58	0.436	3.2
12	19.4x14.3	X=8.53 Y=2.70	15	-4.6	7.0	-5.3	*23.2*	7.3	-6.3	3.06	1.27	0.452	0.4
13	19.4x14.3	X=8.53 Y=2.70	15	-4.6	7.0	-5.3	*23.8*	7.3	-6.3	3.01	0.52	0.449	0.5
14	19.4x14.3	X=8.53 Y=2.70	15	-4.6	7.0	-5.3	23.5	*7.0*	-6.3	3.02	0.02	0.451	0.2
15	19.4x14.3	X=8.53 Y=2.70	15	-4.6	7.0	-5.3	23.5	*7.6*	-6.3	3.03	.024	0.449	0.2
16	19.4x14.3	X=8.53 Y=2.70	15	-4.6	7.0	-5.3	23.5	7.3	*-6.0*	3.17	4.77	0.439	2.4
17	19.4x14.3	X=8.53 Y=2.70	15	-4.6	7.0	-5.3	23.5	7.3	*-6.6*	3.05	0.96	0.455	1.2
18	*19.1*x14.3	X=8.53 Y=2.70	15	-4.6	7.0	-5.3	23.5	7.3	-6.3	3.14	3.80	0.444	1.3
19	*19.7*x14.3	X=8.53 Y=2.70	15	-4.6	7.0	-5.3	23.5	7.3	-6.3	2.72	10.2	0.461	2.5
20	19.4x*14.0*	X=8.53 Y=2.70	15	-4.6	7.0	-5.3	23.5	7.3	-6.3	3.04	0.38	0.449	0.2
21	19.4x*14.6*	X=8.53 Y=2.70	15	-4.6	7.0	-5.3	23.5	7.3	-6.3	2.96	2.02	0.452	0.5
22	*19.7x14.6*	X=8.53 Y=2.70	*14.7*	*-4.3*	*6.7*	*-5.6*	*23.2*	*7.6*	*-6.0*	3.95	30.4	0.411	8.6
23	*19.7x14.6*	*X=8.35* *Y=2.52*	*14.7*	*-4.3*	*6.7*	*-5.6*	*23.2*	*7.6*	*-6.0*	3.07	1.64	0.43	4.8
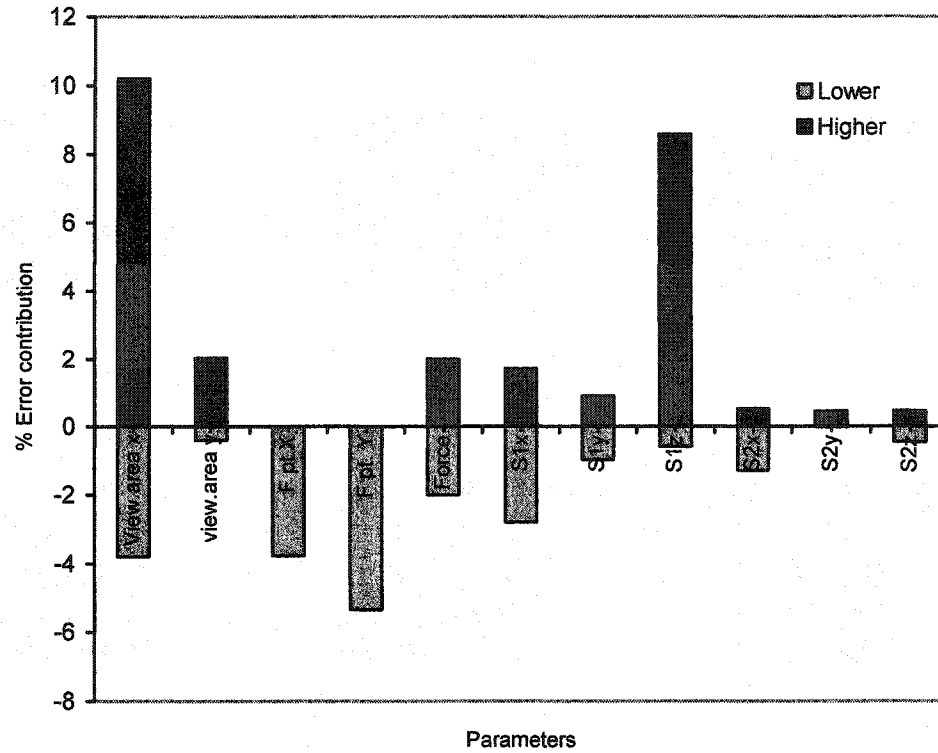
Figure-3.5: The error values associated with E are plotted against the parameters. The upper bars represent the parameter values that have been increased from the actual values by adding the errors associated with parameters. The lower bars are just the opposite.
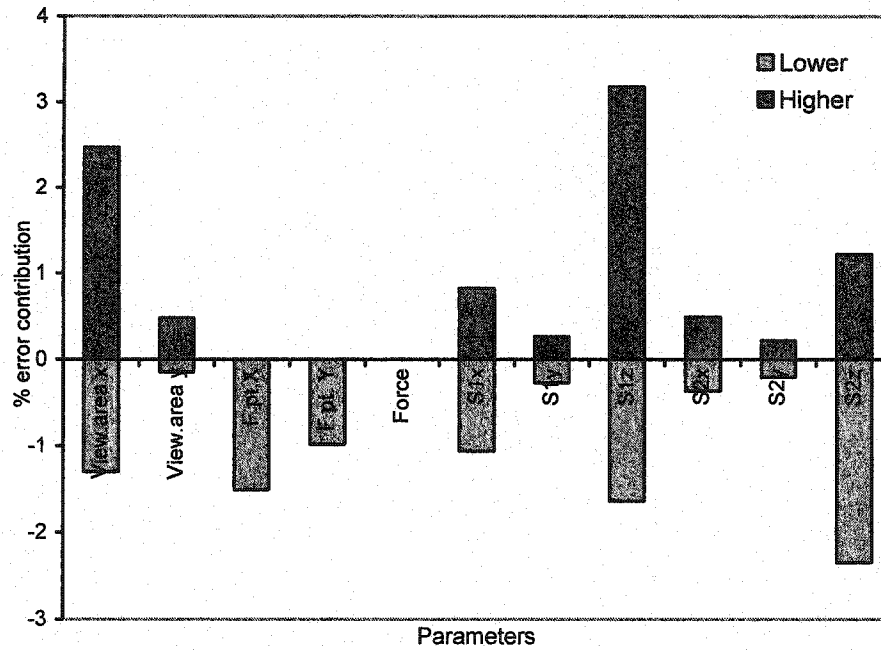
Figure-3.6: The percentage error values associated with v are plotted against the parameters. The upper bars represent the parameter values that have been increased from the actual values by adding the errors associated with parameters. The lower bars are just the opposite.
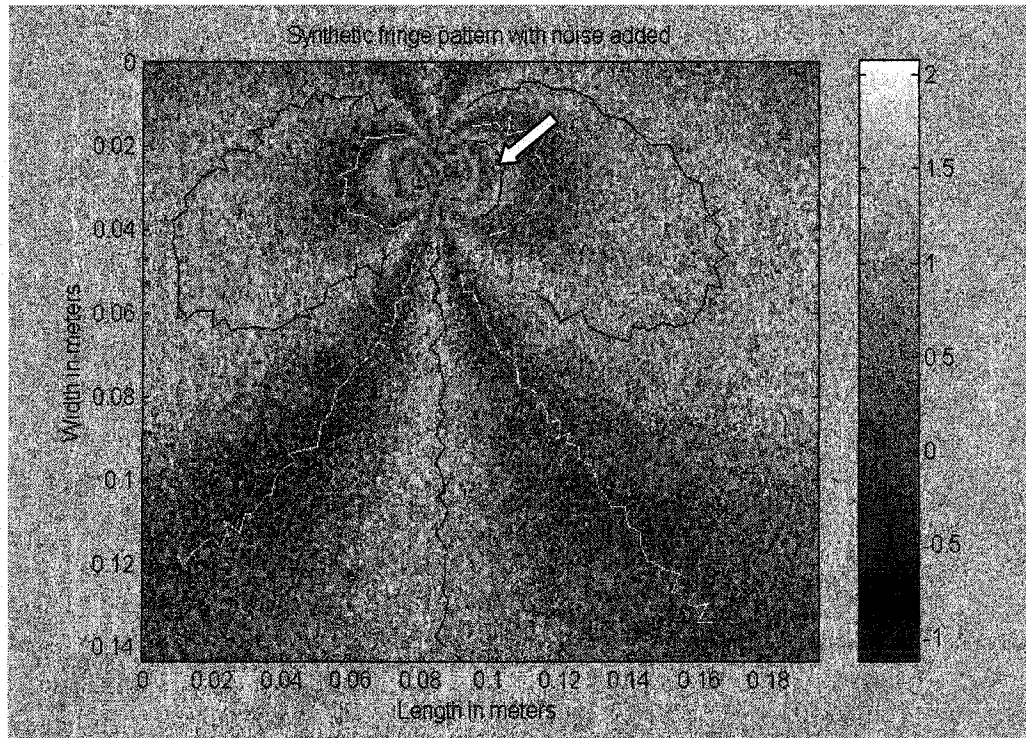
Figure-3.7: Synthetic fringe pattern with noise. Random noise with normal distribution has been added. Fringes are picked along the lines. Force application point is shown with the white arrow.

different result than when the negative (-) error is subtracted from the parameters. This is why the error contributions in Fig.3.5 and Fig.3.6 are not same on both sides of the origin. The only exception is the force.

Inversion of noisy synthetic fringe pattern: In the earlier section, noise free synthetic fringe pattern was inverted. But in reality, the fringes will be contaminated with speckle noise[6]. In this section a noisy synthetic fringe pattern has been inverted for E and v values.

The parameters used to make the image in Fig.3.7 are exactly the same as shown in Table-3.1. Only random noise with Gaussian distribution has been added to it. The image in Fig.3.7 has been inverted to obtain the values of E and v using the usual fringe picking method that involves least square minimization. The results are given in Table-3.4.

Table-3.4: Results from inversion of the image in Fig.-3.7.

Trial No.	No. of fringes picked	No. of Points picked	Win. length	E in GPa	Poisson ratio v	Least sq. error	% Error in E	% Error in v
1	8	148	7x7	2.862	0.455	0.50	4.59	1.05
2	8	161	7x7	3.153	0.445	0.37	5.09	0.98
3	8	134	7x7	2.887	0.455	0.43	3.74	1.15
4	8	128	7x7	2.849	0.456	0.41	5.02	1.37
5	8	139	7x7	2.974	0.452	0.42	0.86	0.49
6	8	142	7x7	2.969	0.453	0.36	1.01	0.63
7	8	145	7x7	2.932	0.454	0.44	2.26	0.90
8	8	149	7x7	3.011	0.452	0.46	0.35	0.43
9	8	157	7x7	2.819	0.457	0.36	6.02	1.51
10	8	183	7x7	3.053	0.450	0.73	1.75	0.14
11	8	508	7x7	3.064	0.449	1.43	2.13	0.24
12	8	631	7x7	3.069	0.448	1.62	2.31	0.51

From the results it is evident that the noise played an important role. The results of E are in error by as high as 6% and as low as 0.35%. The reason of this variation can be explained as follows.

When a particular point is picked, suppose on a noise contaminated black fringe (or white), a window is generated around the point and the coordinate of the minimum valued (or maximum valued) point within that window is selected. In noise free case this point happens to be on the actual fringe minima (or maxima) but in the noise contaminated case, the actual minimum (or maximum) point is shifted due to the noise. This variation changes with position and consequently the results might be far off or fairly close depending on the positions selected. This situation is shown in Fig.3.7, where the lines show the actually picked positions. Noise made the lines erratic.

Inversion of synthetic fringe pattern using white fringes: Earlier the noise free and noise contaminated synthetic fringe patterns were inverted using both the black and the white fringes. Analysis of the experimental images suggests that in some cases the black fringes seem to be more contaminated by noise than the white fringes. This has been suggested on the basis of theoretical analysis of the statistics of the fringe formation recently carried out by Wolfgang Engler[6]. Consequently, it may be important to try to invert first the noise free then the noisy synthetic images using white fringes only. The white fringes are those with a correlation of 1. The results are given in Table-3.5 and Table-3.6.

Table-3.5:   Results from inversion of the image in Fig.3.2 using white fringes.

Trial No.	Fringes picked	Points picked	Window length	E in GPa	Poisson ratio v	Least sq. error	% Error in E	% Error in v
1	4	66	11x11	3.0166	0.4509	3.87×10^{-4}	0.5537	0.2018
2	4	65	11x11	2.9972	0.4492	0.0013	0.0926	0.1833
3	4	74	11x11	3.0145	0.4509	4.06×10^{-4}	0.4822	0.2084
4	4	76	11x11	2.9986	0.451	0.0127	0.0464	0.2196
5	4	68	11x11	3.0057	0.4507	0.0121	0.1888	0.1544
6	4	91	11x11	3.0042	0.4507	0.0152	0.1399	0.1557

From Table-3.5, it's evident that considering only the white fringes doesn't improve the results much at least in the case of noise free fringes.

The results of the inversion of noise-contaminated fringe pattern of Figure-3.7 using the white fringes are given in Table-3.6.

Table-3.6: Results from inversion of the noisy image of Fig.3.7 using white fringes.

Trial No.	Fringes picked	Points picked	Window length	E in GPa	Poisson ratio v	Least sq. error	% Error in E	% Error in v
1	4	49	11x11	2.9416	0.4521	0.1295	1.9450	0.4608
2	4	50	11x11	2.9180	0.4488	0.1870	2.7336	0.2682
3	4	46	11x11	2.8314	0.4556	0.1519	5.6212	1.2376
4	4	47	11x11	2.9845	0.4516	0.1359	0.5152	0.3642
5	4	56	11x11	3.0357	0.4510	0.1814	1.1885	0.2168
6	4	49	11x11	3.1300	0.4476	0.1400	4.3330	0.5400

It is seen that in the noise contaminated case, the results are essentially the same as before when all the fringes were picked [Table-3.4]. In the following figure, there is a comparison between all these results taken from Table-3.2, 3.4, 3.5, and 3.6. Only the first five smallest percentage error values associated with the Young's modulus are plotted in Fig.3.8. The values in pink colour represents the result of the noisy fringe pattern where both black and white fringes have been picked. The black cross represents results from noisy image inversion when only the white fringes were picked. The blue and the brown colours represent the same for noise free cases. At this point, it is clear from these results that picking only the white fringes didn't help improve the results by an appreciable amount neither in the noise contaminated case nor in the noise free case.
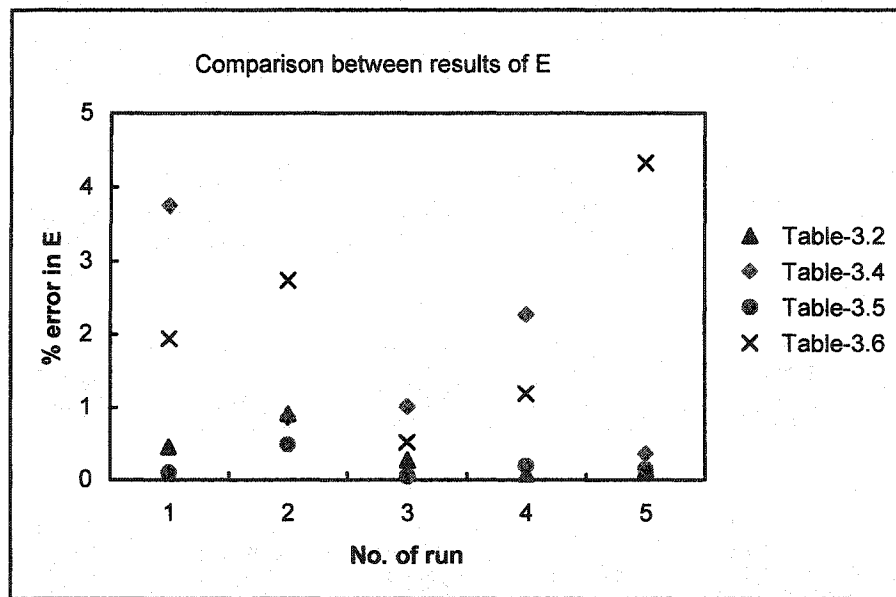
Figure-3.8: The percentages of errors associated with Young's modulus obtained from different inversions are plotted above.

3.4   Experimental Set up

In this section, the geometry of the experimental set up and a real picture of the experimental arrangement are shown.

Geometry of the Experimental Arrangement
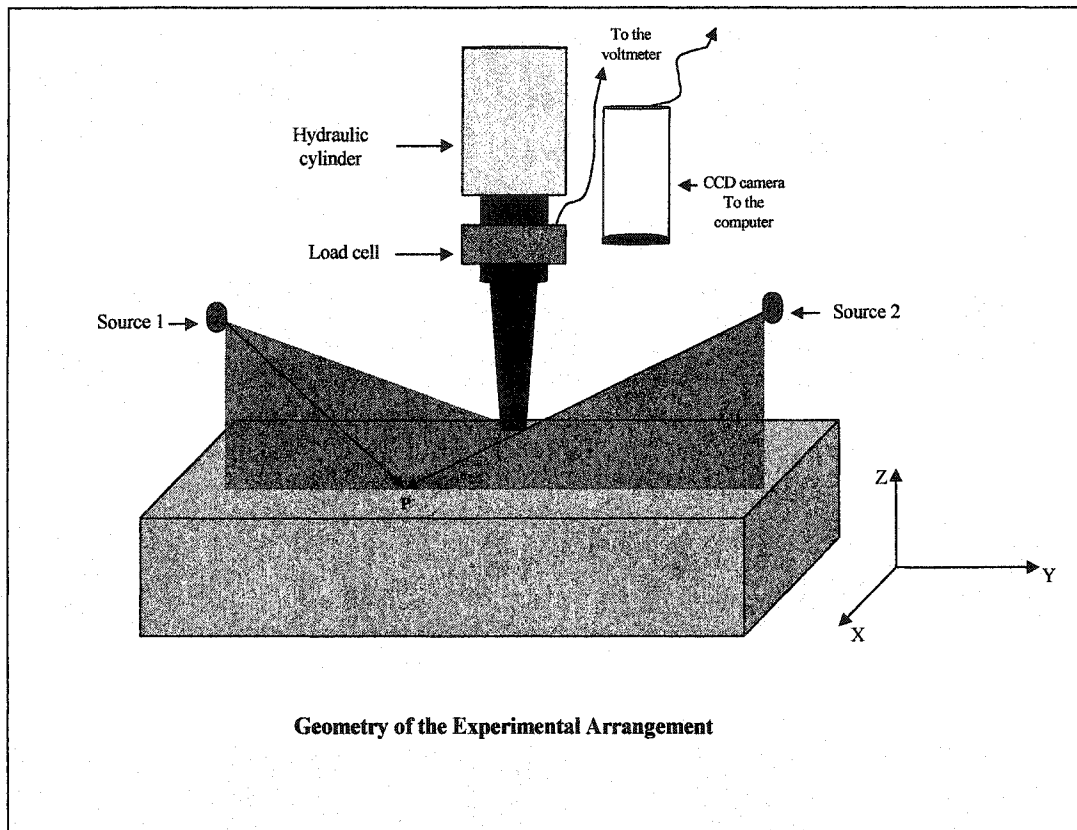
Figure-3.9:   Experimental set up of the dual beam interferometer. The laser sources S_1 and S_2 are created from a single laser source using a beam splitter (not shown). The lasers are shining on the material under investigation.

Optical configuration: During the experiment the whole set up was placed on a metal isolation table floated by air pressure just to reduce the vibration primarily arising from motions of the building due to wind, people, and elevator. Thick black curtains were placed around this table to prevent lights from interfering with the lasers. This is not essentially necessary and the experiment can actually be conducted under

full room lights, although this results in a noisier fringe pattern. The computer along with the monitor, the hydraulic pump and the accumulator are placed in a different table to isolate them from the floating table.

Laser: A Lepton IV Diode Laser combined with CP series precision Diode Laser Driver and CT15W Precision Thermoelectric Controller has been employed for the source. This provides a complete highly stable laser system. The laser wavelength is 829nm (near Infra-red) with maximum output of 35mW. The camera is more sensitive to the infrared laser. The laser head module contains the laser, collimation optics, beam shaping optics and thermoelectric cooler, thermistor and heat sink. Together these provide a highly stable, round collimated source. The beam splitter is a partially silvered glass that allows nearly half of the incident laser to go through and half reflects back. These two beams then fall on abraded ceramic surfaces, called sources S_1 and S_2, that scatter the light to illuminate the object's surface. These surfaces were made by grinding ceramic (or porcelain).

Camera: A CCD camera [Texas Instruments multicam CCD] has been employed to capture the images of the displaced and undisplaced modes.

Hydraulic system: The hydraulic hand pump is connected to the cylinder and piston assembly and an accumulator. The accumulator is used to achieve small changes in the line pressure. A load cell is attached between the piston and the indenter that reads the force exerted on the sample surface by the indenter. The indenter tip is made approximately 0.5cm in diameter to prevent the sample from cracking under load. The signal from the load cell passes through a signal conditioner [Intertechnology, Model 460-115, Calex]. Eventually the force is read in a calibrated voltmeter.

Surface preparation: The surface of the material under investigation has been sand blasted. For the case of aluminum and Plexiglas this sand blasted surface has been painted with non-reflecting white paint to get better scattering of laser light. This improves the image quality significantly. In the case of materials like marble, painting is not required since it is already white. This material is then placed on a solid steel surface (Fig.3.11) that is a part of the interferometer and it also holds the hydraulic cylinder.
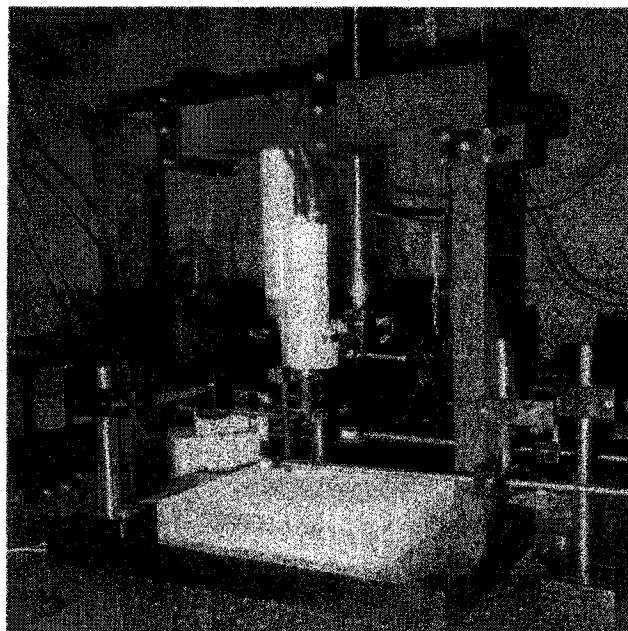
a) Left side.
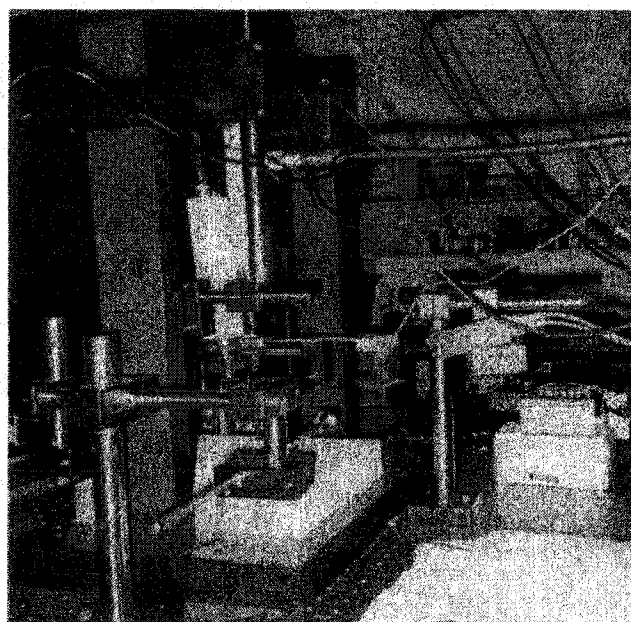
b) Right side.

Figure-3.10: Photograph of the experimental set up.

The source holders, beam splitter, camera and laser are all movable in three directions x, y and z, which gives flexibility in setting up the apparatus.

3.5   Experimental Results

During the experiment, grey scale images (8 bit, 640 pixels horizontally and 480 pixels vertically) from a high resolution Charged Coupled Display (CCD) camera have been captured immediately before and after the object has been deformed. An image is formed in the monitor by the 'Speckle' software created by Wolfgang Engler, in collaboration with Vision Smart, Edmonton AB, as part of an NSERC strategic grant. This software captures one initial reference image (consider it as the undeformed state of the surface) and later captures the image (video image) of the deformed surface. These two images are cross-correlated (using Pearson's cross correlation method described in chapter 2) to give a fringe pattern on the computer monitor in near real time (system yields four frames per second at present).

This experiment has been done with Plexiglas and marble as samples. The top left corner of the image is chosen as the origin and the source positions are measured with respect to it. The co-ordinates of the point of force application are also measured from this origin and all subsequent measurement such as positions of each pixel, are measured relative to the force application point. The point of force application can also be made as the origin but having the top left corner of the image as origin makes all measurements much easier. The results are summarized in Table-3.8, 3.9 and 3.10.

Results for Plexiglas: A Plexiglas block of dimension 25x22x5 cm is used in this experiment. The viewing area of the surface is 12x8.7cm rectangle. The reference image and the video image are shown in Fig.3.11. The final fringe pattern (Fig.3.12.a) is created after cross correlating these two images using the Speckle Software. The arrow in each figure shows the point of force application. Following similar method Fig.3.12.b is created.
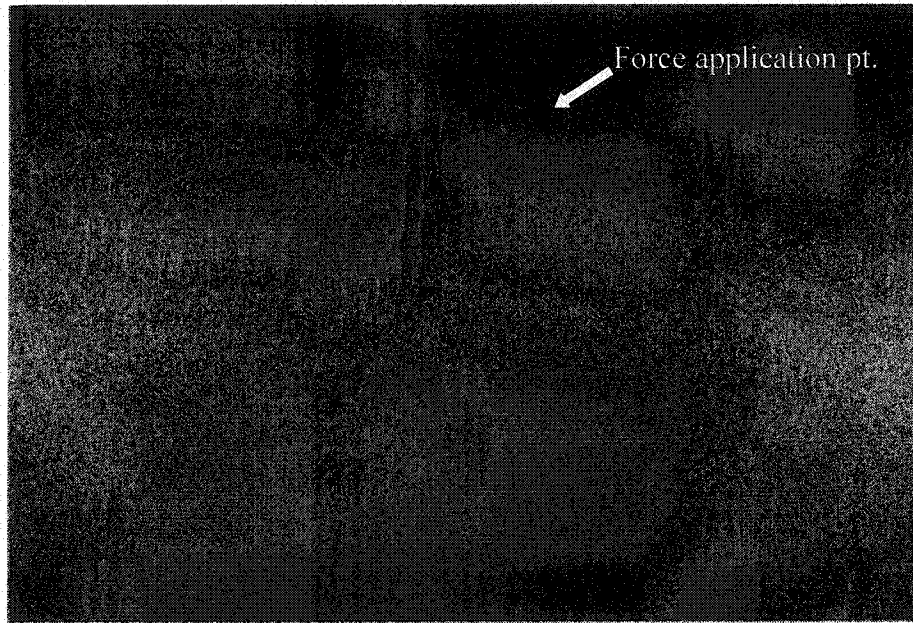
a.
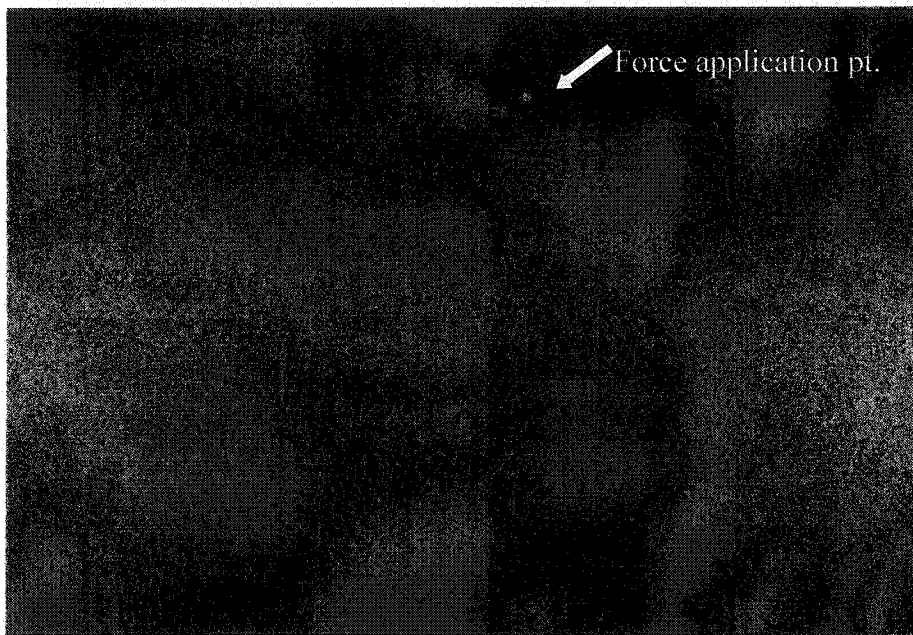
b.

Figure-3.11: a) Reference image and b) Video image from the experiment.
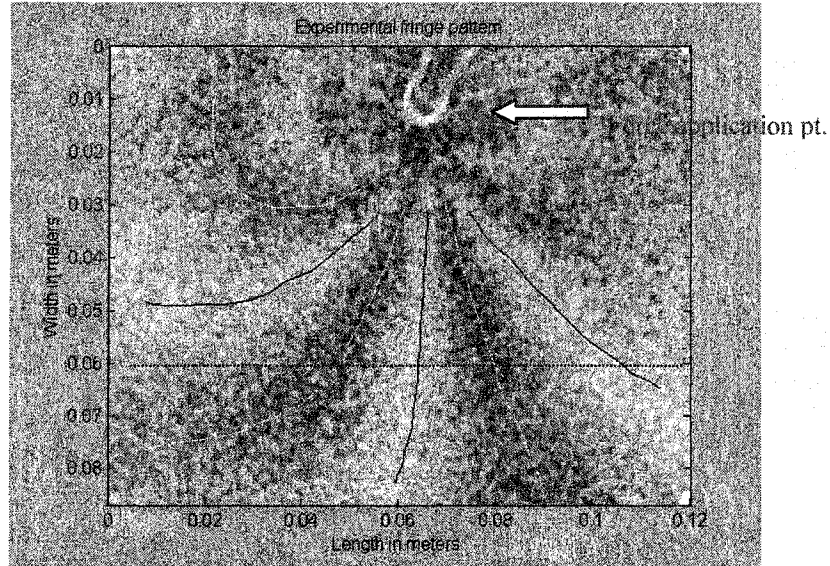
Figure-3.12.a: Experimental Fringe pattern of Plexiglas. The indenter put 1000N of force on the surface. The intensity pattern along 0.06m line is shown in Fig.3.13.
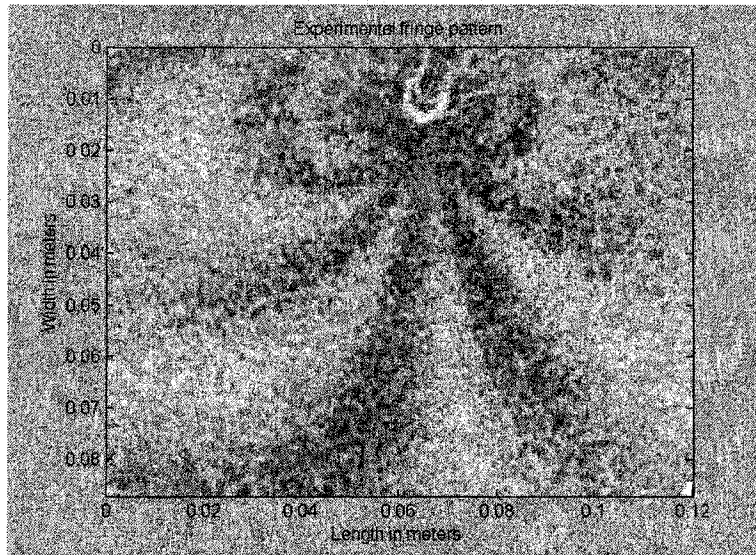
Figure-3.12.b: Experimental Fringe pattern of Plexiglas. The indenter put 1300N of force on the surface. The intensity pattern along 0.06m line is shown in Fig.3.13.

Table-3.7:   Input parameters used in the inversion of experimental images.

Viewing area	Force appl. Point in cm.	Force on the block	Source positions (x,y,z) in cm	Laser wavelength
(12x 8.7) cm	X=6.3	1000-N	S_1 (-2.3, 4.6, -5.6)	829nm
	Y=1.0	1300-N	S_2 (15, 5.1, -5.4)	

Table-3.8:   Results of inversion of experimental fringe pattern for Plexiglas.

| App. Force N	Trial No.	No. Fringe picked	Points picked	Win. length	E in GPa	Poisson ratio v	Least sq. error	Ave. E GPa ±0.3	Ave. v ±0.03
	1		280		3.31	0.37	0.56		
	2		391		3.11	0.39	0.58		
1000	3	8	386	0x0	3.05	0.39	0.74	3.1	0.38
	4		484		3.15	0.39	0.67		
	5		597		3.16	0.38	0.48		
	1		297		3.35	0.37	4.4		
	2		330		3.16	0.37	6.8		
1300	3	6	436	0x0	3.19	0.39	5.35	3.1	0.38
	4		308		2.9	0.39	4.5		
	5		503		2.81	0.38	5.0		

In the inversion, the experimental image is first corrected for perspective distortion (details of this analysis is given in Appendix C). Then points are picked manually along the lines in Fig.3.12.a, i.e., no window was created around the picked point. The reason can be seen from the intensity spectrum of this noisy image (Fig.3.13). A window would not be able to find the exact position of the central maxima or the minima as it is shifted due to the noise. So, in this case, the minima and the maxima are selected just by looking at the image with the interpreter biases included. Similar method is followed for the inversion of Fig.3.12.b.

The average results of E and v are 3.1±0.3GPa and 0.38±0.03 respectively. These two values are used along with the input parameters in Table-3.7 to reproduce the
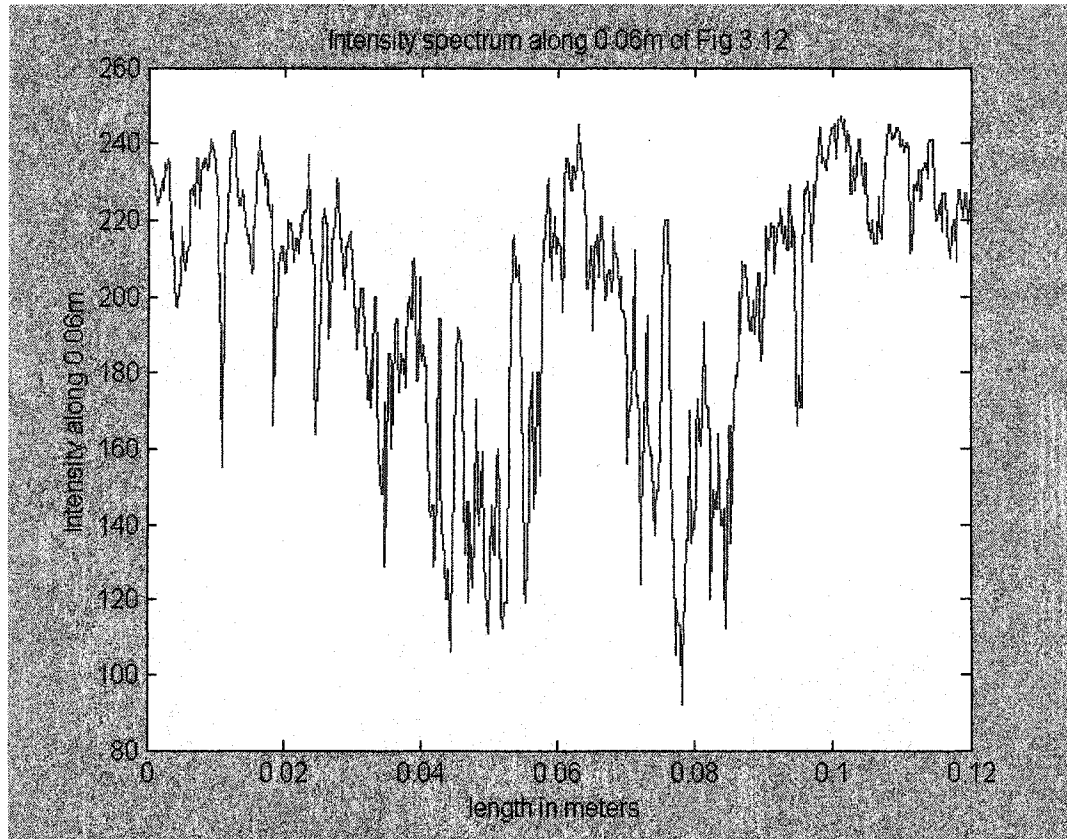
Figure-3.13: Intensity spectrum of the image in Fig.3.12.a along 0.06m.
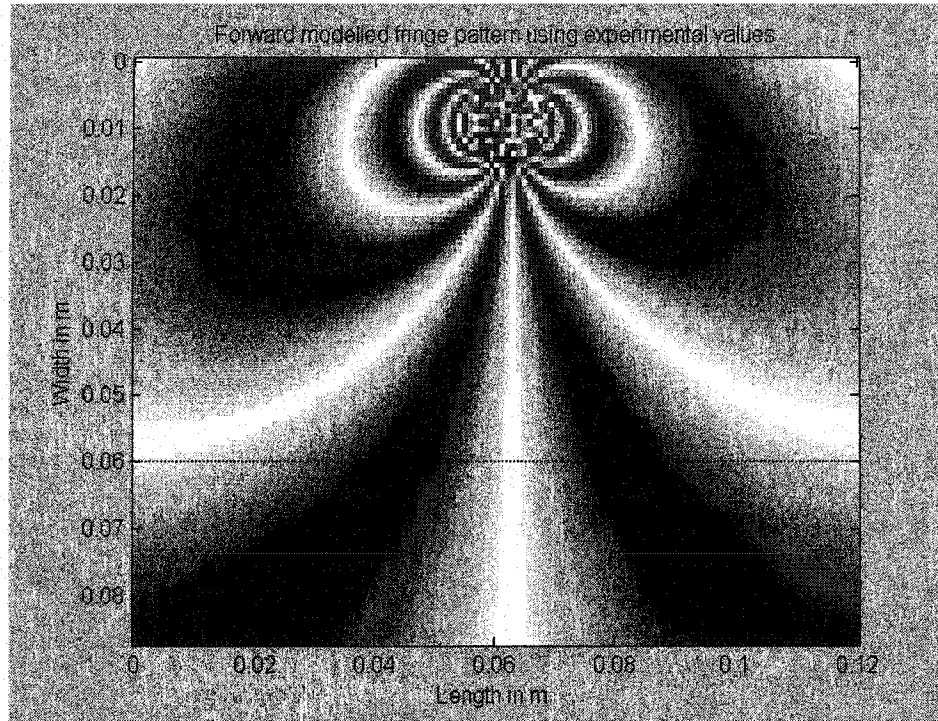
Figure-3.14: Reproduced Fringe pattern of Plexiglas corresponding the experimental one in Fig.3.12.a. The parameters used are same as in experiment (Table-3.7). E and ν are 3.1GPa and 0.38 respectively (Table-3.8).
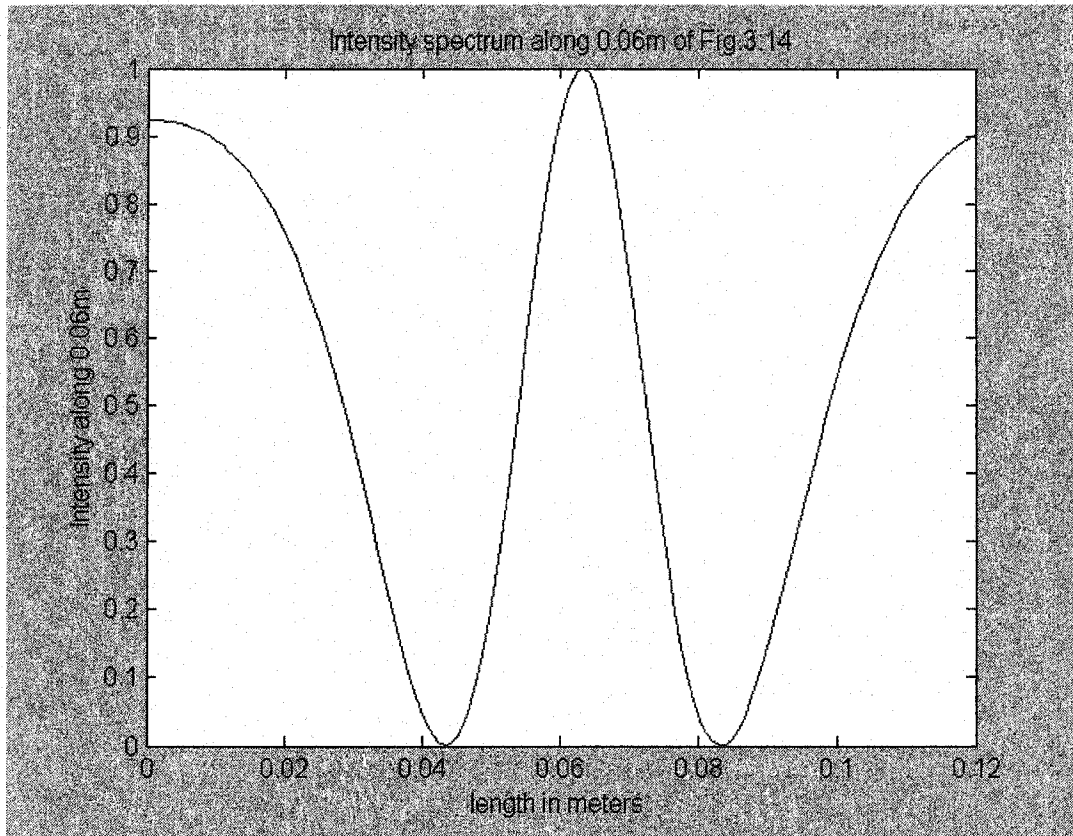
Figure-3.15: Intensity spectrum of the reproduced image in Fig.3.14 along 0.06m line.

fringe pattern in Fig.3.12.a. This will allow comparing the experimental image with the synthetic one. The reproduced fringe pattern is shown in Fig.3.14 and the intensity spectrum along 0.06m line is potted in Fig.3.15.

Results for marble: One of the objectives of this work is to apply this ESPI method to natural rocks to determine their elastic parameters. Experimental results using marble as sample has been presented in the following section.

Table-3.9: Input parameters used in the inversion of experimental marble image.

Viewing area	Force appl. Point in cm.	Force on the block in N	Source positions (x,y,z) in cm	Laser wavelength
(13x 9) cm	X=7 Y=2.4	1000	S_1 (-1.55, 6, -6.65) S_2 (15.8, 6.2, -7.3)	829 nm
		1100		

Table-3.10.A: Results of inversion of experimental fringe pattern of marble.

Force in N	Trial No.	No. Fringes picked	Points picked	Win. length	E in GPa	Poisson ratio v	Least sq. error	Ave. E in GPa	Ave. v
1000	1	3 on left	293	0x0	3.05	0.245	0.73	3.00	0.25
	2		181		2.99	0.238	0.77		
	3		413		2.98	0.250	0.52		
	4		285		3.03	0.246	0.88		
	5		364		2.97	0.251	0.28		
	1	10	465	0x0	1.48	0.353	21.7	1.50	0.36
	2		398		1.68	0.334	19.2		
	3		421		1.55	0.347	22.5		
	4		456		1.29	0.374	11.5		
	5		343		1.48	0.351	18.6		

Table-3.10.B: Results of inversion of experimental fringe pattern of marble.

Force in N	Trial No.	No. Fringes picked	Points picked	Win. length	E in GPa	Poisson ratio v	Least sq. error	Ave. E in GPa	Ave. v
1100	1	3 on left	230	0x0	2.94	0.253	1.21	2.96	0.25
	2		180		2.82	0.267	0.20		
	3		264		2.95	0.25	0.23		
	4		275		3.11	0.235	0.52		
	5		313		2.98	0.245	0.26		
	1	10	442	0x0	1.22	0.39	11.16	1.3	0.38
	2		380		1.19	0.40	13.21		
	3		286		1.42	0.37	16.10		
	4		422		1.36	0.37	21.15		
	5		356		1.39	0.36	19.85		

In the inversion of experimental images for marble, first three fringes on left side of the images [Fig.3.16.a and Fig.3.16.b] are picked. Next, ten fringes from all over the images are picked. This is done to find the effect of the non-homogeneity of the marble sample. The average results obtained from the second type of inversion [Table-3.10.A, E=1.5GPa, v=0.36 and Force=1000N] is used to reproduce the fringe pattern in Fig.3.17 which corresponds to the experimental fringe pattern in Fig.3.16.a. The difference between Fig.3.17 and Fig.3.16.a is clearly visible. But when the image is reproduced using the average values of E=3GPa and v=0.25 with the force F=1000N [Table-3.10.A], the three fringes on left side [Fig.3.18, fringes 2, 1.5 and 1] matched exactly with the same three fringes in Fig.3.16.a. Similar situation is observed between Fig.3.19 and Fig.3.16.b.
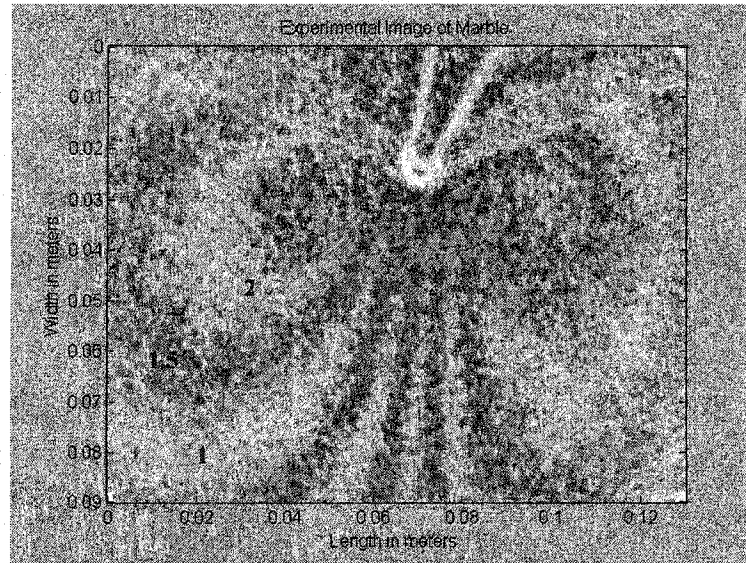
Figure-3.16.a: Experimental fringe pattern of marble.

Force applied = 1000N.
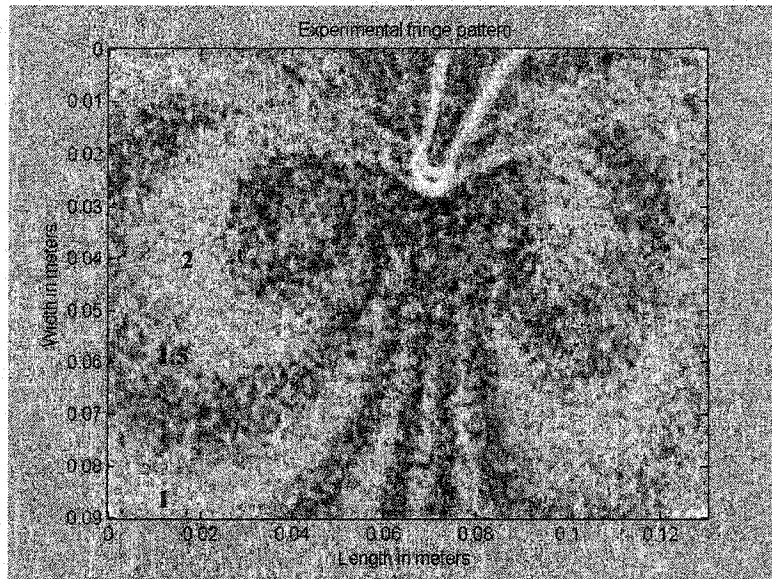
Figure-3.16.b: Experimental fringe pattern of marble.

Force applied = 1100N.
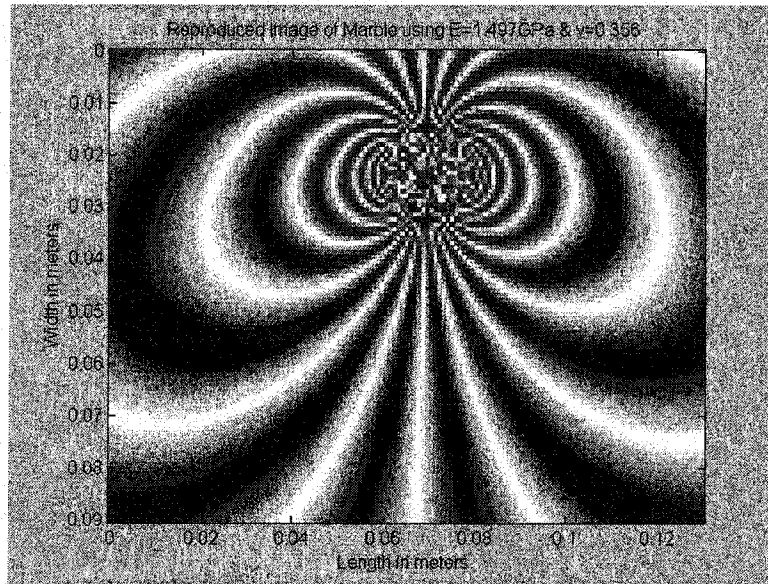
Figure-3.17: Reproduced fringe pattern of marble with the values of E=1.5Gpa and v=0.36.
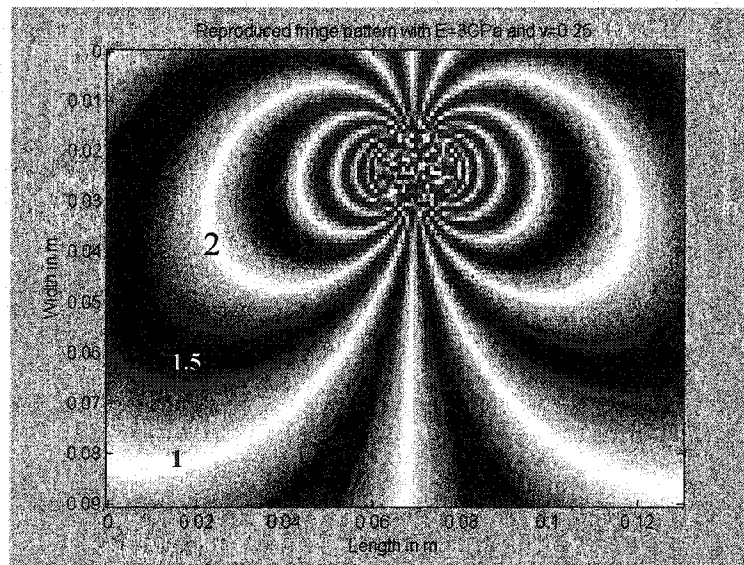
Figure-3.18: Reproduced fringe pattern of marble using the values E=3Gpa and v=0.25. Applied force is 1000N. This figure corresponds to Fig.3.16.a.
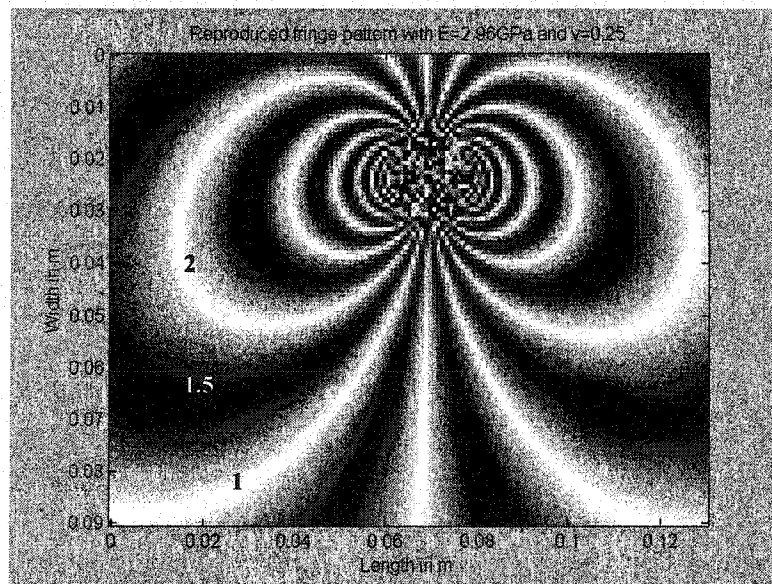
Figure-3.19: Reproduced fringe pattern of marble using the values E=2.96Gpa and v=0.25. Applied force is 1100N. This figure corresponds to Fig.3.16.b.

3.5   Conclusion

The ESPI method employing fringe inversion by direct correlation resulted in values of Young's modulus E and Poisson ratio v with an error of 2% and 0.3% respectively in the case of synthetic fringes. For experimental fringes the result of E for Plexiglas matched with the manufacturers specification of 3.1GPa and within 3% of the value determined by the strain gauge method (Appendix D), which is 3GPa. The Poisson ratio v is found to be 0.38 which also matched with the value obtained by the strain gauge method (0.38). Therefore for Plexiglas, which is a homogeneous material, this ESPI method is very successfully applied. For marble the results (E=2.96GPa and v=0.25) are not as expected (E=20~70GPa and v=0.2~0.3). This could be due to the non-homogeneity of the sample used or due to bending occurring when the sample is loaded or the uneven lower surface of the sample. This marble sample is further investigated in Chapter-4 using a different method.

References:

1. R. Jones and C. Wykes, *'Holographic and Speckle Interferometry'*, Cambridge University Press, Cambridge, UK, 1983.

2. C. M. Vest, *Holographic Interferometry*, Wiley, New York, 1979.

3. S.P. Timoshenko and J. N. Goodier, *'Theory of Elasticity'*, Third Edition, McGraw-Hill Inc. New York, 1970.

4. D. R. Schmitt, C. Smither and T. J. Ahrens, *'In-situ holographic elastic moduli measurements from boreholes'*, Geophysics, Vol. 54, No. 4, pp.468-477, Apr.1989.

5. D. R. Schmitt and R. W. Hunt, *'Model-based inversion of speckle interferometry fringe patterns'*, Applied Optics, Vol.37, No.13, pp.2573-2578, 1998.

6. W. Engler, *'Laser Speckle Interferometry: A Stochastic Investigation'*, M.Sc. Thesis, Dept. of Physics, University of Alberta, Spring 2002

Chapter 4

Determination of Young's Modulus of Cantilever Beams

4.1 Introduction

In the previous chapter, Young's modulus and Poisson ratio of a block of material has been determined using ESPI quite successfully. In each case the viewing area was large in all directions. In reality situations may arise where the sample size is significantly small and force of the amount of thousands of Newton might destroy or disfigure the sample permanently. This chapter is devoted to determine the Young's modulus of a sample that has thickness as little as 0.64cm, width 2.54cm and length 13cm. It is a piece of aluminum block and would require very little force to cause any appreciable displacement if it is set up as a cantilever beam. This is discussed in the following sections.

4.2 Analysis Methodology

The deflection curve for a cantilever beam, fixed at one end and loaded at the other end (Fig.4.1), is given by[1]

$$U_z = \frac{F}{2EI}\left(lx^2 - \frac{x^2}{3}\right) \tag{4.1}$$

where F is the force causing the deflection, E is the Young's modulus of the material of the beam, l is the distance of the point of load application on the beam and x is the distance from the fixed end to the point of deflection on the beam. The moment of

inertia I is dependent on the width and thickness of the beam and is given by

$$I = \frac{bd^3}{12}$$ (4.2)

where b is the width and d is the thickness of the beam. The beam deflection U_z is entirely assumed in the z-direction die to the geometry of the problem.

A dual-beam laser speckle interferometer is employed to find the change in phase in the speckle pattern due to the deflection of the beam. The speckle pattern changes cyclically with respect to the magnitude and direction of the displacement and the position of each point on the cantilever surface relative to the sources as represented by unit vectors n_1 and n_2 (Appendix B, Fig.B.1). The change between the speckle patterns taken immediately before and after the displacement is given in terms of a change in phase[2] as

$$\varphi(x,y,z) = \frac{2\pi}{\lambda}\left[n_1(x,y,z) - n_2(x,y,z)\right]\cdot U(x,y,z)$$ (4.3)

Substituting the value of defection U_z into Eq.(4.3) and following the same procedure as described in Section-3.2, the fringe intensity is calculated from the following relation

$$\rho(x,y,z) = \frac{1}{2}\left(1 + \cos\varphi(x,y,z)\right)$$ (4.4)

Now recall Eq.(3.11) which has been used for inversion of fringe pattern in Section-3.2. The corresponding equation for the cantilever problem is

$$\begin{bmatrix} n \\ \cdot \\ \cdot \\ n \\ n-1/2 \\ \cdot \\ \cdot \\ n-1/2 \\ n-1 \\ \cdot \\ \cdot \end{bmatrix} = \begin{bmatrix} A_1 \\ A_2 \\ A_3 \\ \cdot \\ \cdot \\ \cdot \\ \cdot \\ \cdot \\ \cdot \\ A_{i-1} \\ A_i \end{bmatrix} [m]$$ (4.5)

71

where i is the total number of picked points. In this case A and m are given as

$$A = \frac{Fk_z}{4\pi I}\left(lx^2 - \frac{x^3}{3}\right)$$
(4.6)

$$m = \frac{1}{E}$$
(4.7)

Equation (4.5) may be written in matrix notation as

$$N = GM$$
(4.8)

The value of Young's modulus E is determined from Eq.(4.8) using the well known Least Square Minimization method as employed in Section-3.2

$$M = (G^T G)^{-1} G^T N$$
(4.9)

In the following sections this procedure is first tested on artificially calculated fringe patterns and then applied to real experimental fringe patterns.

4.3   Modelling and Inversion:

In the following sections, first a forward modelled fringe pattern of a deflected cantilever beam is created from Eq.(4.4) by substituting Eq.(4.1) into Eqs.(4.3). Then this synthetic fringe pattern is directly inverted using the least square minimization method [Eq.(4.9)] to get back the Young's modulus E of the material.

Synthetic fringe creation: The fringe pattern in Fig.4.2 is created by applying 0.25N force at the end of the cantilever beam made of aluminum with Young's modulus E = 70GPa (E = 70E9 N/m^2). The surface of the cantilever (which is the x-y plane) is assumed to be illuminated by two coherent laser sources $S_1(x,y,z)$ and $S_2(x,y,z)$. The input parameters used are given in the following table.

Table-4.1: Input parameters used to create Fig.4.2.

Viewing area	Force appl. point. (x-y) cm	Force in Newtons	Sources positions (x,y,z) in cm	Laser wavelength	E In GPa
(15x 2.5) cm	X=15.0 Y=1.25	0.25	S_1 (-1, 1.5, -8) S_2 (17 1.5 -7)	829nm	70

72
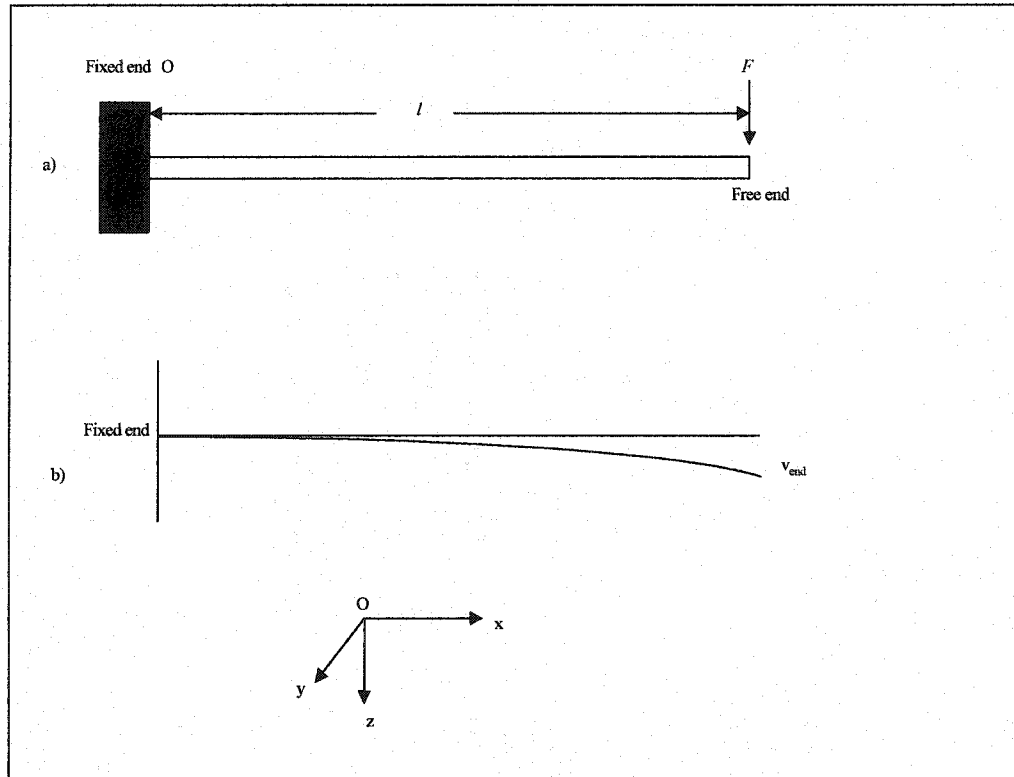
Figure-4.1: Cantilever carrying a concentrated load at the end.

Inversion of synthetic fringe pattern: The fringe pattern of Fig.4.2 is inverted to get the value of E by the fringe picking method which applies least square minimization as described before [Chapter 3, Section-3.2]. To provide input to the inversion, points were manually picked along the bright and dark fringes. A window of size 15x15 pixels was delineated around each picked points. One of the minimization curves is shown in Fig.4.3. The results are given in Table-4.2.

Table –4.2: Results from inversion of the image in Fig.4.2.

Trial No.	Fringes picked	No. of Points picked	Win. length	E in GPa	Least sq.error $X10^{-4}$	% Error in E	Average E in GPa
1		116		70.04	2.55	0.052	
2		101		70.62	2.88	0.886	
3	6	96	15x15	70.44	2.38	0.624	70.4
4		119		70.61	1.31	0.871	
5		113		70.08	2.12	0.114	
6		124		70.51	1.67	0.730	
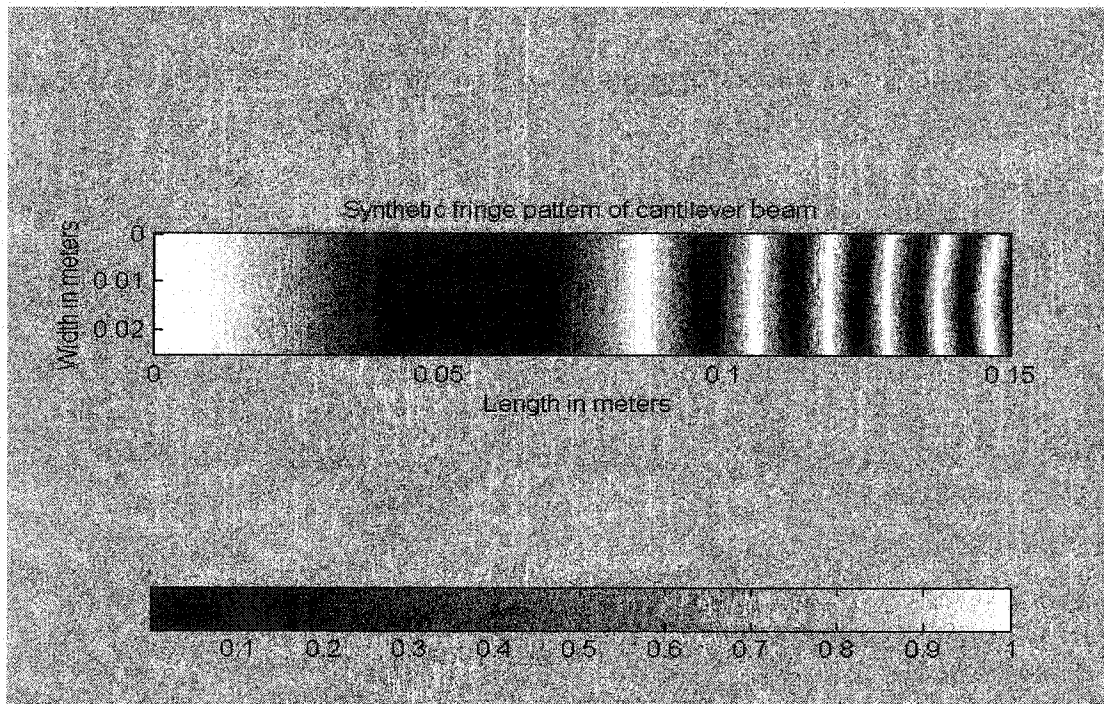
Figure-4.2: Synthetic fringe pattern of a cantilever beam loaded at the end x=15cm.
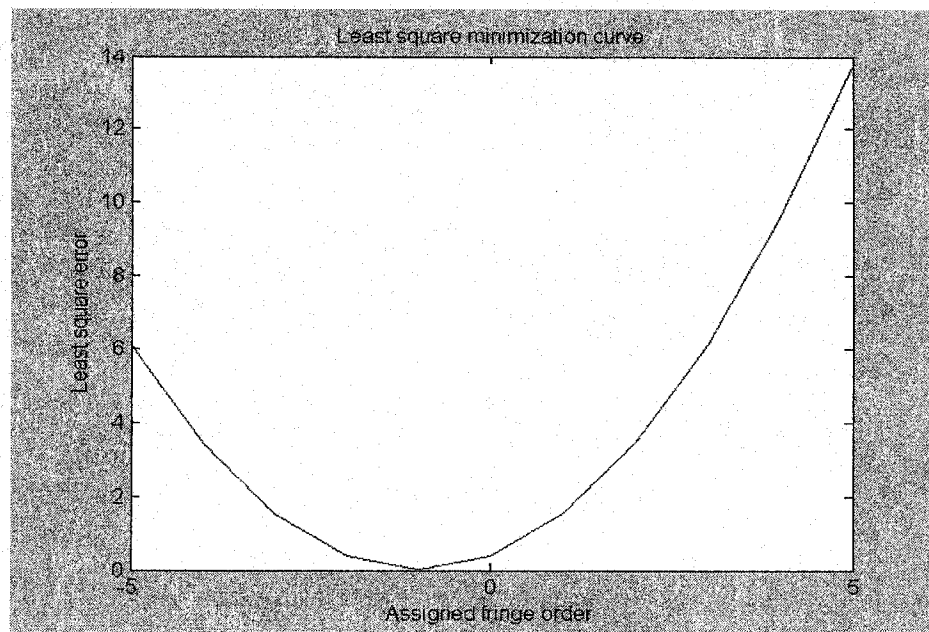
Figure-4.3: One of the minimization curves from the inversion of Fig.4.2.

4.4 Experimental Results and Discussion:

Results for aluminum: An aluminum cantilever beam of length 13cm, width 2.54cm and thickness 0.64cm is loaded with 0.20N and 0.30N of forces at the free end. Grey scale images (8 bit, 640 pixels horizontally and 480 pixels vertically) from a high resolution Charged Coupled Display (CCD) camera have been captured immediately before and after the cantilever is loaded. The images are formed in the monitor and subsequently inverted using the fringe picking method. The results are summarized in Table-4.3 and 4.4. The top left corner of the image is considered as origin for all the measurements. The rest of the procedure in fringe picking is exactly the same as followed in Chapter-3. These images are shown in Fig.4.4 and Fig.4.5.

Table-4.3: Input parameters used in the inversion of experimental images.

| Viewing area	Force appl. Point in cm.	Applied load	Source positions (x,y,z) in cm	Laser wavelength
(13x 2.54) cm	X=13	0.2-N	S_1 (-14.1, 1.3, -4.7) S_2 (3.3, 1.5, -4.4)	829nm
	Y=1.25	0.3-N		

Table-4.4: Results of inversion of experimental fringe pattern for aluminum.

Trial No.	No. Fringes picked	Points picked	Load in N	Win. length	E in GPa ±2.5	Least sq. error	Ave. E in GPa ±2.5	
1	6	121			62.83	0.44		
2	6	137			61.95	0.39		
3	6	153			59.65	0.86		
4	6	134	0.2		60.11	0.57	61.1	
5	6	147			61.02	0.55		
1	6	119		0x0	60.96	0.25		60.5
2	6	134			58.88	0.53		
3	6	149			59.20	0.80		
4	6	138	0.3		61.10	0.71	60.0	
5	6	135			59.85	0.62		

The average result of E is 60.5±2.5GPa. This value is used along with the input parameters in Table-4.3 to reproduce the fringe patterns. This allowed comparing the experimental images with the synthetic ones. The reproduced fringe patterns are shown in Fig.4.4.b and Fig.4.5.b. This value of Young's modulus (60.5±2.5GPa) agrees with the result 60±2GPa found by the standard strain gauge method (Appendix D). When the experimental images and the reproduced images are compared, they are in excellent agreement. The extreme right ends of the experimental images are hazy because of the high illumination level of the laser at this end. The fringe positions of the reproduced patterns in Fig.4.5.a and Fig.4.5.b matched with that of the experimental fringe patterns in Fig.4.4.a and Fig.4.4.b respectively.
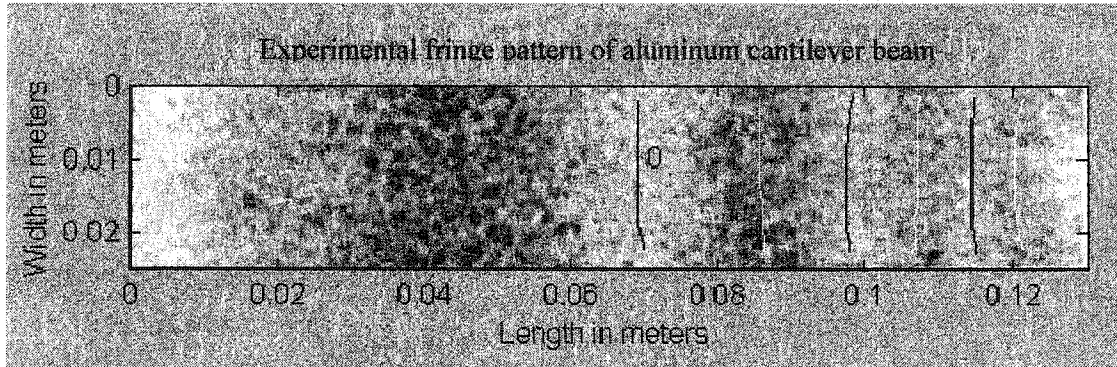
Figure-4.4.a: Experimental fringe pattern of cantilever beam. The applied load is 0.2N at the extreme right end of the image. Fringes are picked along the lines.
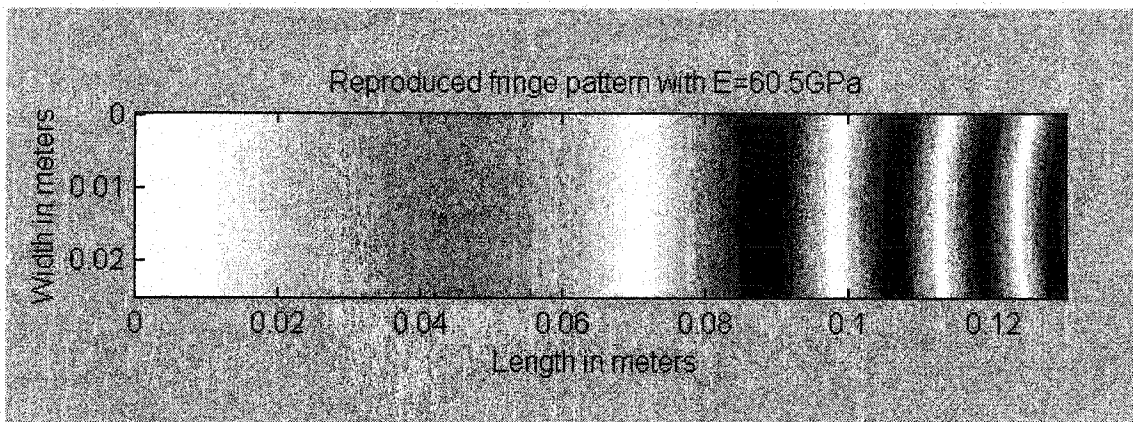
Figure-4.4.b: Reproduced fringe pattern with E=60.5GPa and F=0.2N. This image corresponds to Fig.4.4.a.
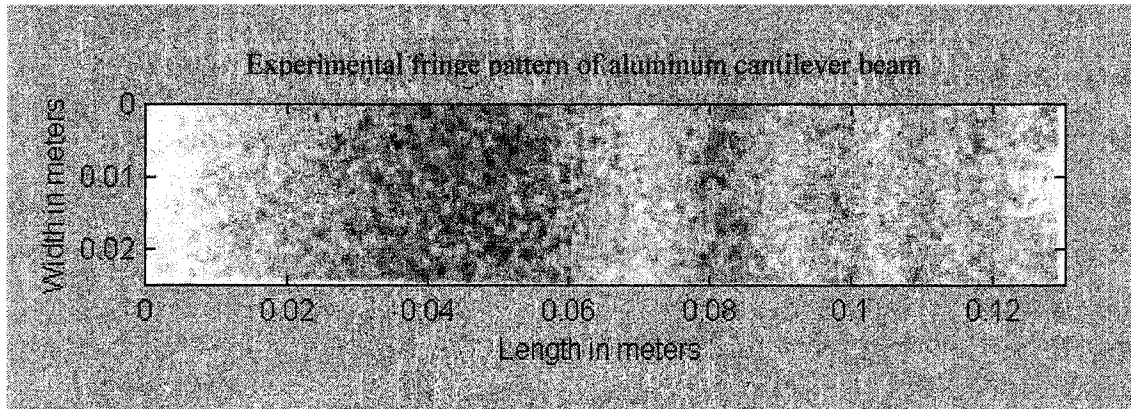
Figure-4.5.a: Experimental fringe pattern of cantilever beam. The applied load is 0.3N.
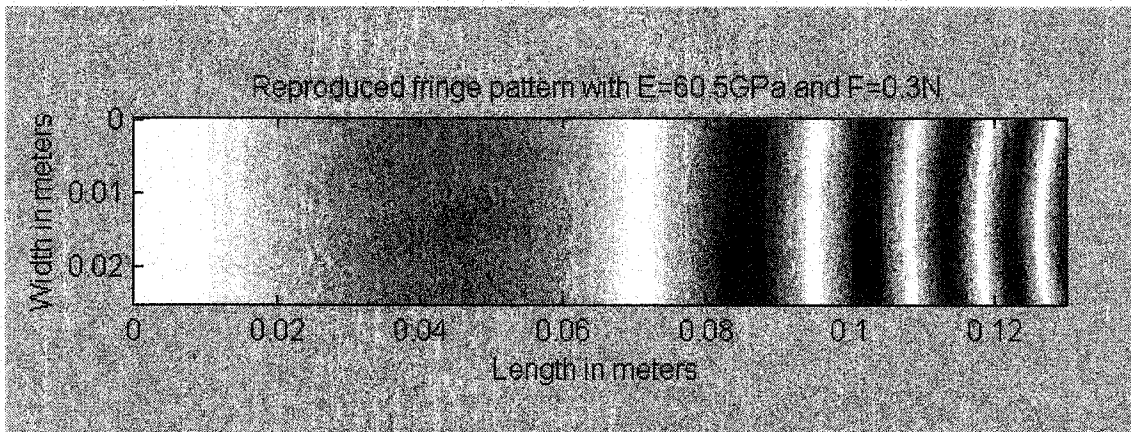
Figure-4.5.b: Reproduced fringe pattern with E=60.5GPa and F=0.3N. This image corresponds to Fig.4.4.b.

Results for marble: In this case a piece of marble (16.2x3.2x1.55)cm has been used as cantilever beam and is deformed gradually by placing 30, 40, 50, 70 and 100gm of weight at the free end. As before grey scale images of the deformed and unreformed states are captured and subsequently inverted using the fringe picking method (Fig.4.6). These results are summarized in Table-4.5 and 4.6. Using the results in Table-4.6 and the input parameters in Table-4.5, each of the images have been reproduced and shown in Fig.4.7.

Table-4.5: Input parameters used in the inversion of experimental marble images.

Viewing area	Force appl. Point in cm.	Applied load	Source positions (x,y,z) in cm	Laser wavelength
(16.2x 3.2) cm	X=16.2 Y=1.6	0.29-N 0.39-N 0.49-N 0.69-N 0.98-N	S_1 (1.9, 1.4, -3.8) S_2 (19.3, 1.3, -3.9)	829nm

Table-4.6: Results of inversion of experimental marble fringe patterns.

Applied load in N	No. Fringes picked	Win. length	No. of trials for each image	Average E in GPa ± 2
0.29	3		5	18.1
0.39	4		6	18.2
0.49	5	0x0	6	17.2
0.69	5		6	13.5
0.98	7		5	13.2
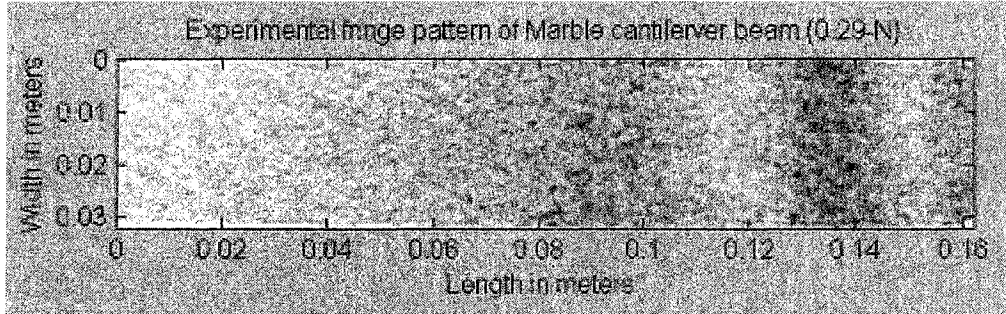
Figure-4.6.a: Experimental fringe pattern of marble for 30gm load.
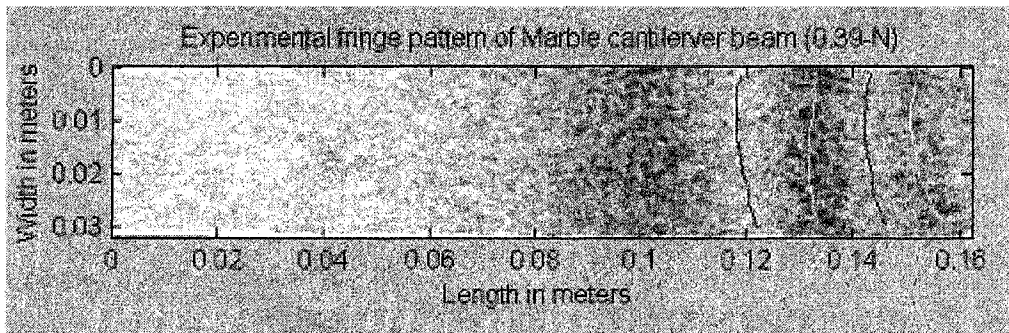
Figure-4.6.b: Experimental fringe pattern of marble for 40gm load.
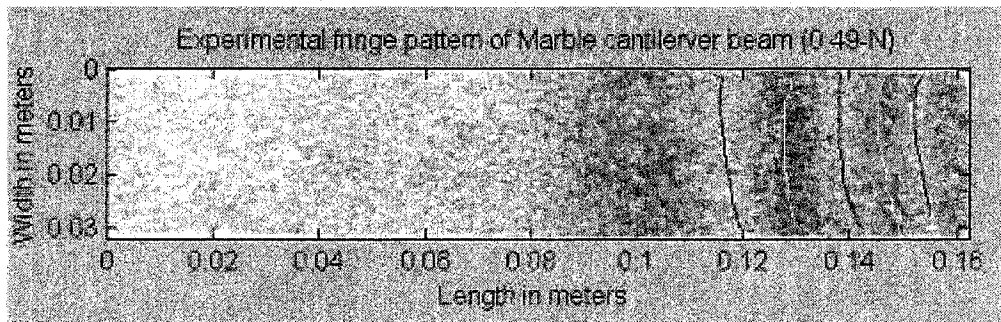
Figure-4.6.c: Experimental fringe pattern of marble for 50gm load.
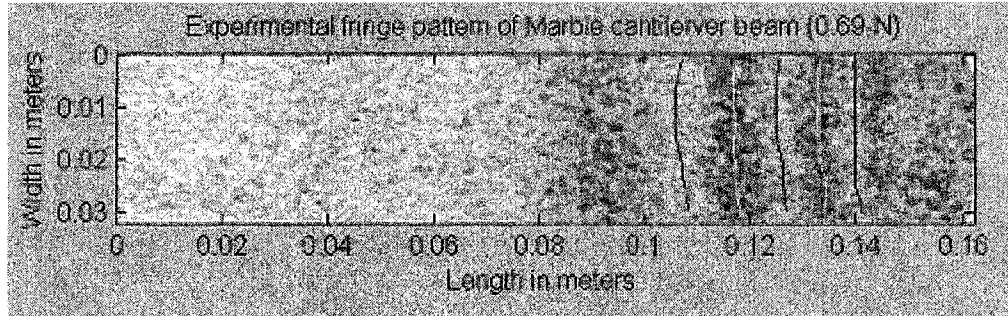
Figure-4.6.d: Experimental fringe pattern of marble for 70gm load.
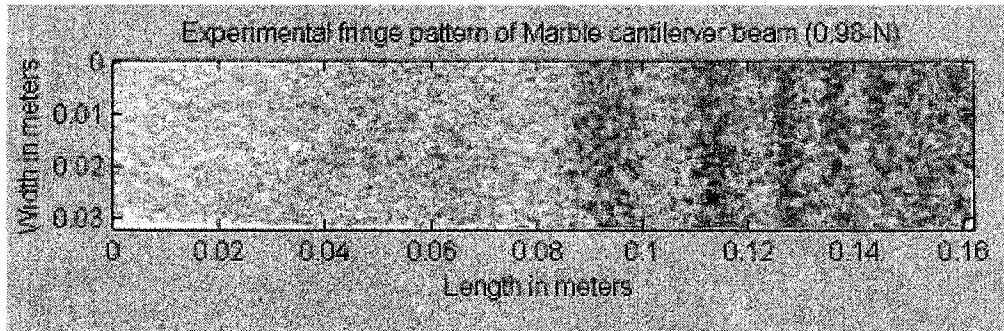
Figure-4.6.e: Experimental fringe pattern of marble for 100gm load.
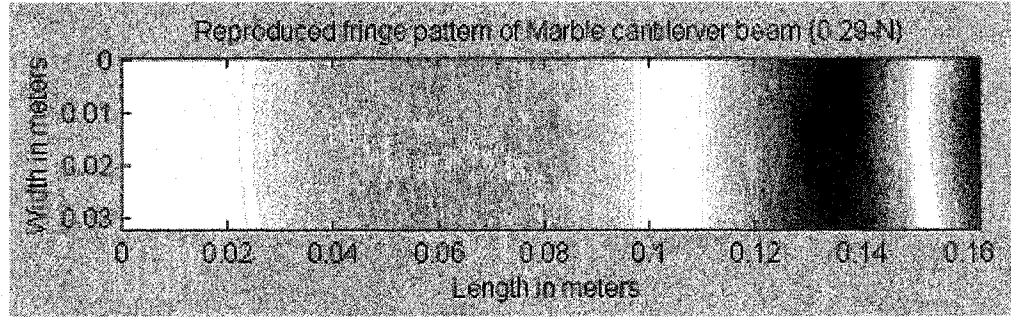
Figure-4.7.a: Reproduced fringe pattern of marble cantilever loaded with 30gm.
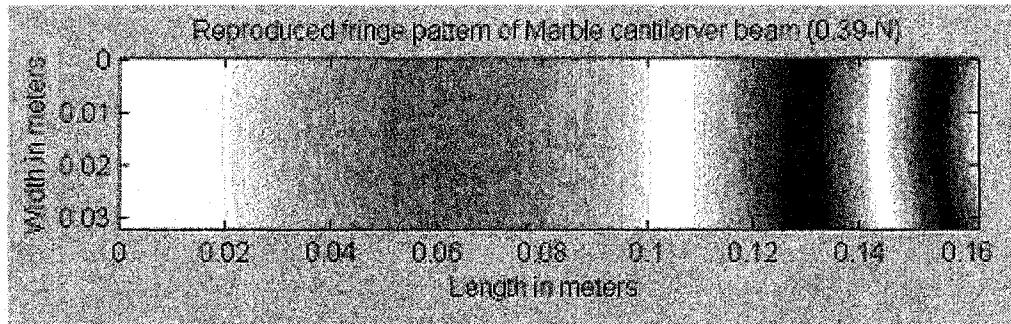
Figure-4.7.b: Reproduced fringe pattern of marble cantilever loaded with 40gm.

Figure-4.7.c: Reproduced fringe pattern of marble cantilever loaded with 50gm.
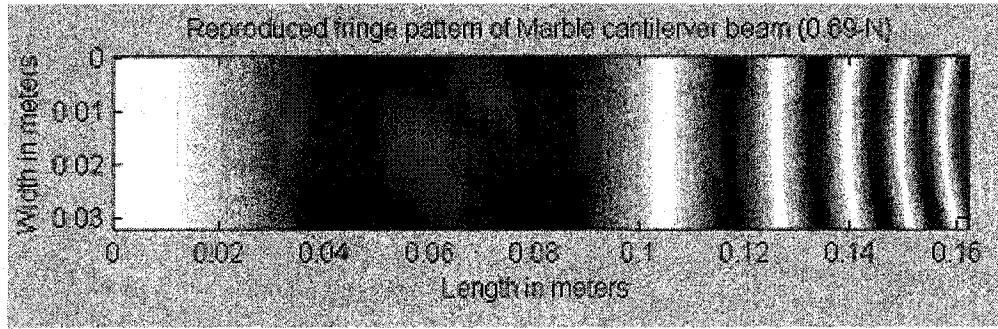
Figure-4.7.d: Reproduced fringe pattern of marble cantilever loaded with 70gm.
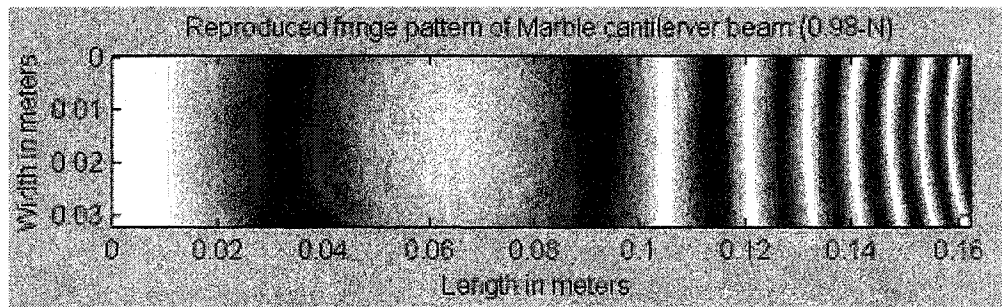
Figure-4.7.e: Reproduced fringe pattern of marble cantilever loaded with 100gm.

The value of the Young's modulus obtained from the inversion of marble images varied between 13Gpa to 19Gpa with different applied load as shown in Table-4.6. This might be arising from the non-homogeneity of the marble sample. When the images are reproduced, the first three (Figures 4.7.a, 4.7.b and 4.7.c) showed sig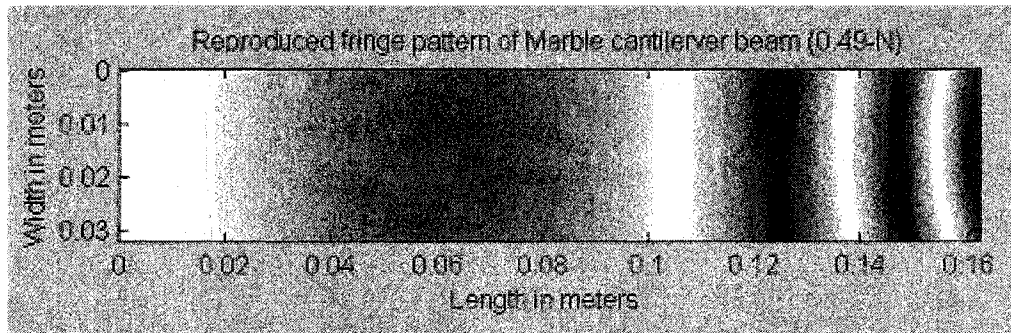nificant difference from the respective experimental images in terms of the fringe positions. But the last two reproduced fringe patterns (Figures 4.7.d and 4.7.e) are very close with the respective experimental images.

The results of the Young's modulus of marble obtained above are plotted in Fig.4.8 against the applied load. There is a gradual decrease in the value of E. Although the mechanical properties of rocks may not follow linear elasticity at high stress level, or at temperatures that are a significant fraction of the rock solidus, all rocks at relatively low temperatures and pressures behave elastically when the applied force is not too large[3]. So at this experimental load range it is more likely that the differences in E values are due to the unevenness of the sample surfaces than anything else.

4.5   Conclusion

Electronic Speckle Pattern Interferometry has been successfully applied in creating interferograms of cantilever beams both virtually and experimentally. The virtual inversion resulted an average value of 70.4Gpa of the Young's modulus which is only 0.6% off from the input 70Gpa. The experimental interferogram of aluminum cantilever beam resulted a value 60.5Gpa of the Young's modulus of the material which is less than 1% off from the value obtained using strain gauge method (60Gpa). For the cantilever beam made of non-homogeneous marble, the value of Young's modulus ranges from 13Gpa to 19Gpa depending on applied load. The reproduced interferograms show better similarity with the experimental ones when the input Young's moduli are around 13Gpa.

Young's modulus vs Load for Marble cantilever
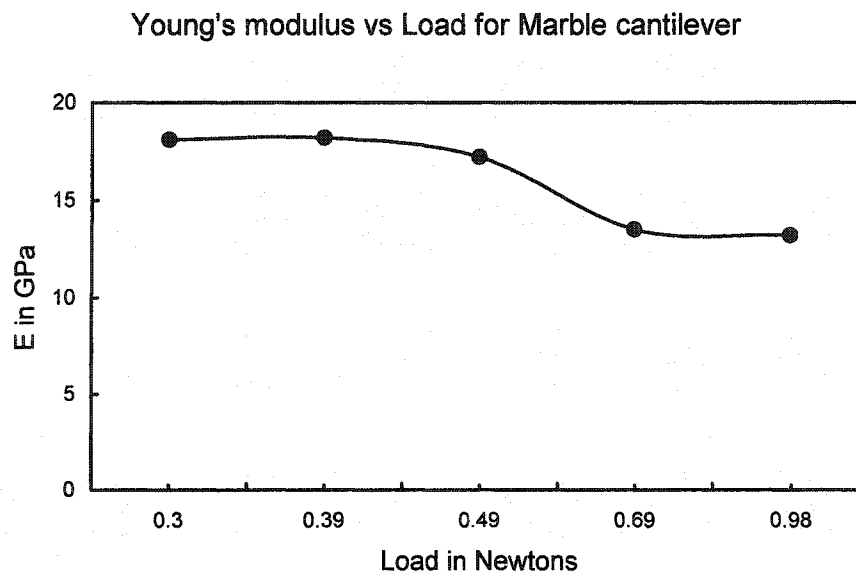
Figure-4.8: Experimentally obtained values of the Young's modulus E of marble cantilever are plotted against the applied load. A non-linear response is readily observable.

References:

1. P. P. Benham and R. J. Crawford, *'Mechanics of Engineering Materials'*, 2nd Edition. Essex, England, pp. 176-178. 1996.

2. R. Jones and C. Wykes, *'Holographic and Speckle Interferometry'*, Cambridge University Press, Cambridge, UK, 1983.

3. G. Schubert and D. L. Turcotte, *'Geodynamics Applications of Continuum Physics to Geological Problems'*, John Wiley & Sons. Inc. United States, 1982.

Chapter 5

Conclusion

In the present work, Electronic Speckle Interferometry (ESPI) has been employed to measure the elastic co-efficients of homogeneous and non-homogeneous materials; an extension of the technique of residual stress determination by Schmitt and Hunt[1]. In the process first theoretical interferograms are created and inverted and later it has been tested experimentally on three different kinds of materials – Plexiglas, marble and aluminum, to determine their Young's modulus and Poisson ratio.

During the Boussinesq analysis of Plexiglas and marble blocks, forward modelled synthetic fringe patterns are calculated using the Boussinesq displacement equations[2] for normal loading on the surface of the material. These synthetic interferograms are inverted using Least Square Minimum error method to obtain the Young's modulus and Poisson ratio of the material. This virtual inversion produced results with less than 2% of error for Young's modulus and 0.4% for Poisson ratio. To verify the computer precision, synthetic fringes have been directly inverted from the known phase. The result for Young's modulus is within 0.003% of the original value and Poisson ratio resulted with 0% error. One significant feature that is observed during the inversion is that the value of the Poisson ratio always resulted with less error. An error analysis has been carried out to find the sensitivity of the parameters like x, y and z co-ordinates of the laser sources, applied load etc. in the experiment. It is found that the cumulative effect of the errors associated with different parameters brings the errors with the output values towards 5% to 6%. The virtual inversion is performed successfully and the whole method is tested experimentally with Plexiglas and marble samples.

In the experiment with Plexiglas, which applied Boussinesq's deformation theory, the values of Young's modulus and Poisson ratio are calculated independently from two interferograms created by deforming the Plexiglas surface with known force. No fringe

processing technique was used to remove the noise. The fringe picking method resulted in values of 3.1GPa and 0.38 for Young's modulus and Poisson ratio respectively. The manufacturer's specification for this material are E=3GPa and ν=0.32~0.45. The values obtained by the standard strain gauge method are E=3GPa and ν=0.38. This Plexiglas block is homogeneous and the results matched with the respective expected values. The reproduced fringe patterns show close similarity with the experimental one.

When this experimental test is done with a piece of non-homogeneous marble, the result came out to be E=3GPa and ν=0.25 when only three fringes on the left side of the interferogram are considered. Considering the entire interferogram resulted even lower values; E=1.3~1.5GPa and ν=0.36~0.38. All these values are much lower than the expected value of E=20~70GPa. This is probably due to the unevenness of the lower surface of the sample which would tend to bend under pressure. This marble sample is further studied in the form of a cantilever beam.

In the cantilever experiment, first forward modelled synthetic fringe patterns have been created considering the cantilever deformation equation[3] under a steady load at the free end. These fringe patterns resulted in a value of 70.4GPa in the virtual inversion which is less than 0.6% off from the input value 70GPa. Two cantilever beams made of aluminum and marble has been tested experimentally.

In the experiment, a cantilever beam made of aluminum is loaded at the free end with 20gms and 30gms of weight and two interferograms are created due to the deformation of the surface. These interferograms are inverted for Young's modulus by the fringe picking method and resulted in an average value of E=60.5GPa. The standard strain gauge method resulted in a value of 60GPa for the same piece of aluminum.

The marble cantilever beam has been loaded with five different loads starting from 30gms and ending at 100gms. For each of the cases an interferogram is created and later inverted following the same procedure of fringe picking. At lower loads of 30, 40 and 50gms the value of the Young's modulus of the material of the cantilever came out to be between 17.2 to 18.2GPa. Whereas for 70gms and 100gms of weights the values are 13.5 and 13.2GPa. When the experimental images are reproduced theoretically with these values of E, the images that represent 13.2 and 13.5GPa came out to be similar to the respective experimental ones. Which implies the Young's modulus of the marble to

be 13.3GPa (average value of 13.2 and 13.5GPa). But again this is not in the range of the expected value of 20~70GPa for marble.

Therefore, for the non-homogeneous marble sample the Boussinesq analysis resulted in a value of E=3GPa and the Cantilever method resulted in E=13.3GPa. This discrepancy could be due to the fact that although in both cases the marble samples are cut from the same piece, they are not measured in the same direction; i.e., during the Boussinesq method the E was measured along z-direction whereas in the cantilever test it was measured along y-direction. The result is, therefore, inconclusive for the marble and further investigation is necessary.

A Few of the disadvantages of the ESPI method as observed during this work are as follows:

- The optics has to be separated from the surroundings to reduce noise due to vibration of the building. This requires the experiment to be done on an optical table floated by air. This would limit the applicability of the method in fieldwork.

- The fringe patterns are highly sensitive to temperature fluctuations mainly due to the heat radiated from human body close to the set up. Moreover, the experimental sample has to be warmed up for at least half an hour before the experiment to avoid any significant movement due to heat conduction on the surface.

- The material under investigation has to be sand blasted and smoothened to achieve correct deformation at a specific load.

- The width and breadth of the cantilever beam is highly influential on the result. For example a change of 1mm in breadth along the length of the beam can change the result of E by 15 to 20 percent. So the beam has to be evenly cut and smoothened.

The advantages are:

- The inversion method is simple and straightforward. It does not require any fringe processing.

- The whole experiment can be done on a sample without cutting out portions of it to fit into the universal testing machines.
- The cantilever experiment is particularly simple to implement and invert.

This ESPI technique can be utilized to determine stress discontinuity and crack formation and propagation on materials. Further effort can be made in automating the fringe picking method so that after the deformation the output results will be shown in the monitor in real time.

References:

1. D. R. Schmitt and R. W. Hunt, '*Inversion of Speckle Interferometer Fringes for Hole-drilling Residual Stress Determinations*', Experimental Mechanics,

2. S.P. Timoshenko and J. N. Goodier, *'Theory of Elasticity'*, Third Edition, McGraw-Hill Inc. New York, 1970.

3. P. P. Benham and R. J. Crawford, '*Mechanics of Engineering Materials*', 2nd Edition. Essex, England, pp. 176-178. 1996.

Appendix   A

Basic Concepts

Waves and Their Superposition

The simplest kind of oscillation, which is fundamental to all kinds of wave motion, is known as Simple Harmonic Motion (SHM). When a particle is oscillating with simple harmonic motion, its displacement $\Phi(t)$ in a given direction from a fixed point at time t is described by the following equation

$$\Phi(t) = u_o \sin(2\pi f t + \phi) \tag{A.1}$$

where u_0 is the maximum displacement of the particle from its equilibrium position and f is the frequency of vibration of the particle. The argument of the sine function $(2\pi f t + \phi)$ is called the phase of the oscillation with initial phase φ. The time period $\tau = 1/f$ is the duration of one cycle of motion. This vibrating system is given an initial energy which it will try to retain indefinitely if dissipative forces are not present. The kinetic energy K of the system is given by

$$K = \frac{1}{2} m v^2 \tag{A.2}$$

where v is the velocity of the body. In reality the velocity changes cyclically and so must the kinetic energy. However, a potential energy P may be defined such that the sum of the two remains constant. The elastic potential energy P is given as

$$P = \frac{1}{2} \kappa x^2 \tag{A.3}$$

where κ is the spring constant and is a measure of the stiffness of the spring.

If P is defined as zero when $K = K_{max}$, then the total energy E is given by

$$E = K_{max} \tag{A.4}$$

When the vibrating particle passes through the origin, its velocity is at a maximum, having a value of

$$v_{max} = 2\pi f u_o \tag{A.5}$$

giving the energy of the system as

$$E = 2m\pi^2 f^2 u_o^2 \tag{A.6}$$

Now consider a wave being propagated along a string. If one end of the string is made to vibrate up and down so that its motion is described by Eq.(A.1). A point adjacent to the end of the string will be forced to oscillate in the same, but will be slightly behind the first point in its motion. However, since the motion of points along the string is cause by the motion of the end of the string, it is clear that energy must be supplied to that point in order to maintain the motion. The rate at which energy passes a given point in unit time is known as the intensity of the wave. If the medium is considered to be made up of a series of particles of mass m and if there are N particles per unit length then the total energy E_λ over one wavelength is

$$E_\lambda = 2mN\lambda\pi^2 f^2 u_o^2 \tag{A.7}$$

Now during one cycle of the motion, an amount of energy E passes a given point so that the amount of energy, which passes a given point in unit time, is given by

$$I = \frac{E}{\tau} = \frac{cE}{\lambda} = 2mNc\pi^2 f^2 u_o^2 \tag{A.8}$$

Thus the intensity of the wave is proportional to the square of its amplitude.

The principle of superposition of waves states that if two or more wavefronts are travelling past a given point, the total amplitude of the displacement at that point is given by the sum of the individual displacements; a system that obeys this principle is a linear system. If the waves are polarized in the same direction, the amplitudes are added algebraically; if the polarizations are different, then a vector addition is required. Consider two wavefronts incident at a point given by

$$\Phi_1 = u_o \sin(2\pi f t + \phi_1) \tag{A.9}$$

$$\Phi_2 = u_o \sin(2\pi f t + \phi_2) \tag{A.10}$$

The total amplitude after some algebraic manipulation is given by

$$\Phi_T = \Phi_1 + \Phi_2 = 2u_o \sin\left(2\pi ft + \frac{\phi_1 + \phi_2}{2}\right)\cos\left(\frac{\phi_1 - \phi_2}{2}\right) \quad\quad (A.11)$$

Thus the resultant motion is a simple harmonic oscillation of frequency f and amplitude

$$u_T = 2u_o \cos\left(\frac{\phi_1 - \phi_2}{2}\right) \quad\quad (A.12)$$

Since the intensity of the wavefronts is proportional to the square of the amplitude, the total intensity I_T given by

$$I_T \propto 4u_o^{\;2} \cos^2\left(\frac{\phi_1 - \phi_2}{2}\right) \quad\quad (A.13)$$

which may be written as

$$I_T = 4I_o^{\;2} \cos^2\left(\frac{\phi_1 - \phi_2}{2}\right) \quad\quad (A.14)$$

where I_0 is the intensity of a single wave. Thus the intensity of the sum of the waves may be twice the intensity of the sum of the individual intensities, may be zero or may have any intermediate value depending on the cosine term. This effect is known as interference.

The solution of Eq.(A.11) to give Eq.(A.12) and Eq.(A.14) for the displacement and intensity were fairly simple since both the waves had the same amplitude u_o. If, however, the amplitudes are different, the above analysis becomes tedious. The mathematics is simplified by representing the displacement with a complex number. Consider the case of light beam. The complex amplitude of the light wave is described by

$$\Phi(r,t) = u_o \exp i(2\pi ft + \phi) \quad\quad (A.15)$$

where $\Phi(r,t)$ is known as the complex amplitude.

Since the intensity is proportional to $u_0^{\;2}$, one may write

$$I \propto \Phi\Phi^* \quad\quad (A.16)$$

Now consider two collinear beams of light represented by complex amplitudes Φ_1 and Φ_2 given as

$$\Phi_1 = u_1 \exp i(2\pi ft + \phi_1) \quad\quad (A.17)$$

$$\Phi_2 = u_2 \exp i(2\pi ft + \phi_2) \quad\quad (A.18)$$

The total complex amplitude is given by

$$\Phi_T = u_1 \exp i(2\pi f t + \phi_1) + u_2 \exp i(2\pi f t + \phi_2) \tag{A.19}$$

This may be written as

$$\Phi_T = (u_1 \exp i\phi_1 + u_2 \exp i\phi_2) \exp i2\pi f t \tag{A.20}$$

The intensity is then readily found from

$$I \propto \Phi_T \Phi_T^* = u_1^2 + u_2^2 + u_1 u_2 \left[\exp i(\phi_1 - \phi_2) + \exp(-i(\phi_1 - \phi_2)) \right] \tag{A.21}$$

Using the relationship

$$(\exp ix + \exp - ix) = 2\cos x \tag{A.22}$$

Eq.(A.21) can be written as

$$\Phi_T \Phi_T^* = u_1^2 + u_2^2 + 2u_1 u_2 \cos(\phi_1 - \phi_2) \tag{A.23}$$

Hence

$$I_T = I_1 + I_2 + 2\sqrt{I_1 I_2} \cos(\phi_1 - \phi_2) \tag{A.24}$$

when the intensity is calculated, the time dependence of the waves disappears.

Appendix B

Analytical Treatment of the Synthetic Fringe Formation and Inversion

B.1 The Sensitivity Vector and Fringe Formation

In a dual-beam speckle interferometer, a coherent laser beam is split and the two rays subsequently expanded to illuminate the surface of the object. Consider a point P on the surface of the object. The vectors joining the point P and the sources S_1 and S_2 are $\mathbf{r}_1$ and $\mathbf{r}_2$ respectively. The geometry is shown in Fig.B.1. Unit vectors $\mathbf{n}_1$ and $\mathbf{n}_2$ indicate the directions from the source points to the surface point $P(x,y,z)$. **A**, **B**, **C** are position vectors of the points P, S_1, and S_2 respectively which are given as

$$\mathbf{A} = x\hat{i} + y\hat{j} + z\hat{k} \tag{B.1}$$

$$\mathbf{B} = x_1\hat{i} + y_1\hat{j} + z_1\hat{k} \tag{B.2}$$

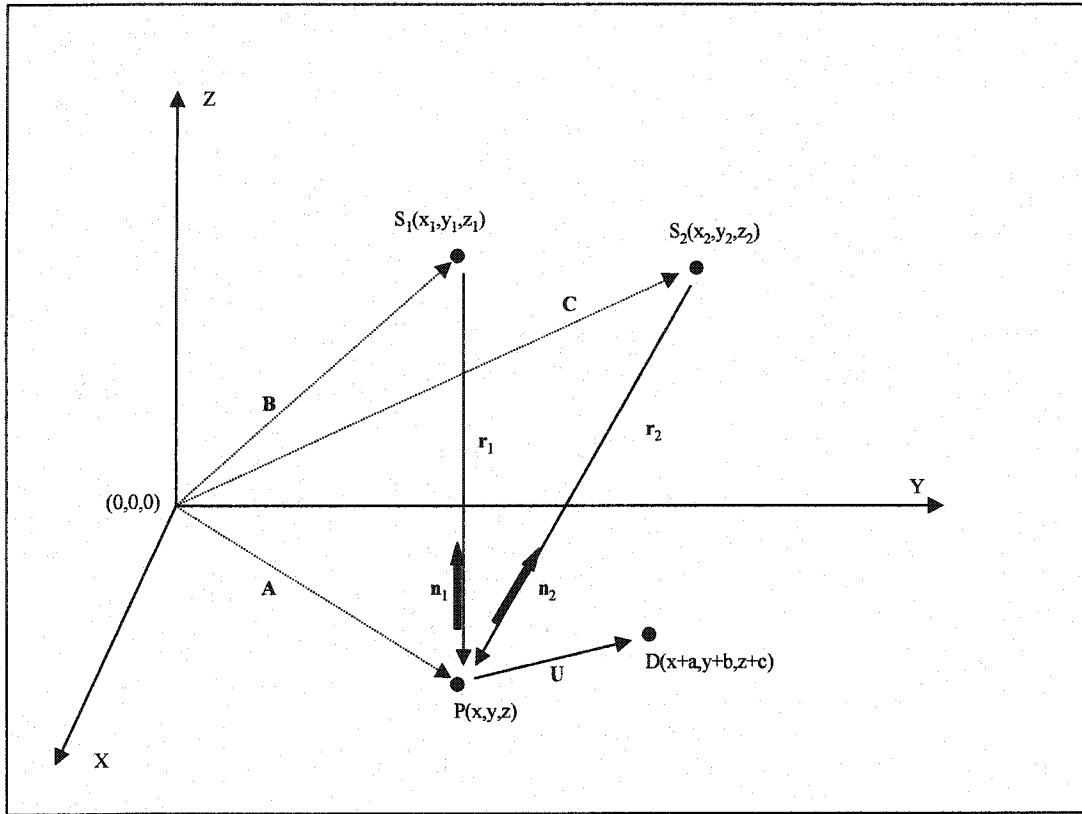$$\mathbf{C} = x_2\hat{i} + y_2\hat{j} + z_2\hat{k} \tag{B.3}$$

Again

$$\mathbf{r}_1 = \mathbf{A} - \mathbf{B}$$

or $\quad \mathbf{r}_1 = (x - x_1)\hat{i} + (y - y_1)\hat{j} + (z - z_1)\hat{k} \tag{B.4}$

And the magnitude of $\mathbf{r}_1$ is

$$|\mathbf{r}_1| = \sqrt{(x - x_1)^2 + (y - y_1)^2 + (z - z_1)^2} \tag{B.5}$$

Figure-B.1: Geometry of the fringe pattern calculation of dual-beam speckle interferometer.

and similarly,

$$\mathbf{r}_2 = (x - x_2)\hat{i} + (y - y_2)\hat{j} + (z - z_2)\hat{k} \tag{B.6}$$

and
$$|\mathbf{r}_2| = \sqrt{(x - x_2)^2 + (y - y_2)^2 + (z - z_2)^2} \tag{B.7}$$

The unit vectors $\mathbf{n}_1$ and $\mathbf{n}_2$ in the directions of $\mathbf{r}_1$ and $\mathbf{r}_2$ are given as

$$\mathbf{n}_1 = \frac{\mathbf{r}_1}{|\mathbf{r}_1|}$$

or
$$\mathbf{n}_1 = \frac{(x - x_1)\hat{i} + (y - y_1)\hat{j} + (z - z_1)\hat{k}}{\sqrt{(x - x_1)^2 + (y - y_1)^2 + (z - z_1)^2}}$$

or
$$\mathbf{n}_1 = \left(\frac{x - x_1}{|\mathbf{r}_1|}\right)\hat{i} + \left(\frac{y - y_1}{|\mathbf{r}_1|}\right)\hat{j} + \left(\frac{z - z_1}{|\mathbf{r}_1|}\right)\hat{k} \tag{B.8}$$

Similarly

$$\mathbf{n}_2 = \left(\frac{x - x_2}{|\mathbf{r}_2|}\right)\hat{i} + \left(\frac{y - y_2}{|\mathbf{r}_2|}\right)\hat{j} + \left(\frac{z - z_2}{|\mathbf{r}_2|}\right)\hat{k}$$

The expression for the sensitivity vector K(x,y,z) is then calculated from the following relation[1]

$$\mathbf{K}(x, y, z) = \left(\frac{2\pi}{\lambda}\right)\left(\mathbf{n}_1(x, y, z) - \mathbf{n}_2(x, y, z)\right) \tag{B.9}$$

So that

$$\mathbf{K}(x, y, z) = K_x\hat{i} + k_y\hat{j} + k_z\hat{k} \tag{B.10}$$

Where

$$K_x = \left(\frac{2\pi}{\lambda}\right)\left(n_{1_x} - n_{2_x}\right)$$

$$K_y = \left(\frac{2\pi}{\lambda}\right)\left(n_{1_y} - n_{2_y}\right) \tag{B.11}$$

$$K_z = \left(\frac{2\pi}{\lambda}\right)\left(n_{1_z} - n_{2_z}\right)$$

The change in the speckle patterns taken immediately before and after the displacement U(x,y,z) is quantified as a phase angle change φ given by[1]

$$\varphi = \mathbf{K}(x, y, z) \cdot \mathbf{U}(x, y, z) \tag{B.12}$$

The fringe pattern intensity ρ in terms of phase φ is[1]

$$\rho(x,y,z) = \left(1 + \cos(\varphi(x,y,z))\right)/2 \tag{B.13}$$

B.2 Analytical Treatment of Fringe Pattern Inversion

The fringe order number n in terms of the sensitivity vector $\mathbf{K}(x,y,z)$ and the displacement vector $\mathbf{U}(x,y,z)$ is given as[2]

$$n(x,y,z) = \frac{\mathbf{K}(x,y,z) \cdot \mathbf{U}(x,y,z)}{2\pi} \tag{B.14}$$

Where

$$\mathbf{U}(x,y,z) = U_x \hat{i} + U_y \hat{j} + U_z \hat{k} \tag{B.15}$$

The surface displacements on isotropic elastic half-space subjected to a normal point load [Boussinesq theory] is given in the Cartesian coordinate system as[3]

$$U_x = \frac{-F(1-2v)(1+v)X}{2\pi E(X^2 + Y^2)}$$

$$U_y = \frac{-F(1-2v)(1+v)Y}{2\pi E(X^2 + Y^2)} \tag{B.16}$$

and
$$U_z = \frac{F(1-v^2)}{\pi E(X^2 + Y^2)^{\frac{1}{2}}}$$

where F is the normal force, E is the Young's modulus and v is the Poisson ratio. U_x, U_y and U_z are displacements in X, Y and Z directions respectively.

Equation (B.14) can be written as

$$n(x,y,z) = \frac{K_x U_x + k_y U_y + K_z U_z}{2\pi} \tag{B.17}$$

Substituting Eq.(B.16) into Eq.(B.17) yields

$$n(x,y,z) = \left[\frac{k_x}{2\pi} \left(\frac{-FX}{2\pi(X^2+Y^2)} \right) + \frac{K_y}{2\pi} \left(\frac{-FY}{2\pi(X^2+Y^2)} \right) \right] \frac{(1-2v)(1+v)}{E}$$
$$+ \left[\frac{K_z}{2\pi} \left(\frac{F}{\pi(X^2+Y^2)^{\frac{1}{2}}} \right) \right] \frac{(1-v^2)}{E} \tag{B.18}$$

Eq.(B.18) can be written as

$$n(x,y,z) = A(x,y,z)\alpha + B(x,y,z)\beta \tag{B.19}$$

Where

$$A(x,y,z) = \left[\frac{k_x}{2\pi} \left(\frac{-FX}{2\pi(X^2+Y^2)} \right) + \frac{K_y}{2\pi} \left(\frac{-FY}{2\pi(X^2+Y^2)} \right) \right] \tag{B.20}$$

$$B(x,y,z) = \left[\frac{K_z}{2\pi} \left(\frac{F}{\pi(X^2+Y^2)^{\frac{1}{2}}} \right) \right] \tag{B.21}$$

$$\alpha = \frac{(1-2v)(1+v)}{E} \tag{B.22}$$

and $$\beta = \frac{(1-v^2)}{E} \tag{B.23}$$

Eq.(B.19) can be written in matrix form as

$$N = \begin{bmatrix} A & B \end{bmatrix} \begin{bmatrix} \alpha & \beta \end{bmatrix}^T \tag{B.24}$$

The values of E and v can be found from Eq.(B.22) and (B.23) to be

$$v = \frac{\alpha - \beta}{\alpha - 2\beta} \tag{B.25}$$

$$E = \frac{1-v^2}{\beta} \tag{B.26}$$

Once the values of α, β are known, E and v is calculated from Eqs(B.25) and (B.26).

References:

1. R. Jones and C. Wykes, *'Holographic and Speckle Interferometry'*, Cambridge University Press, Cambridge, UK, 1983.

2. D. R. Schmitt & R. W. Hunt, *'Inversion of Speckle Interferometer Fringes for Hole-drilling Residual Stress Determinations'*, Experimental Mechanics, Vol.40, No.2, June 2000.

3. S.P. Timoshenko and J. N. Goodier, *'Theory of Elasticity'*, Third Edition, McGraw-Hill Inc. New York, 1970.

Appendix C

Correction for Perspective Distortion

The images captured in the ESPI method suffers from perspective distortion mainly due to the angle of view of the CCD (Charged Couple Display) camera, which captures the images of the undeformed and deformed states of the surface under investigation, with respect to the surface normal. Due to this oblique sight the inspected surface appears deformed in the recorded image and may not fill the full frame. A spatial transform maps the pixels of the recorded interferograms to new pixels in the output interferogram, such that identical points of the object surface, which are imaged to different pixels in the recorded images, are mapped to identical pixels in the output images.

In the algorithm given below, a distorted image of an arbitrary convex quadrangle is rectified into a rectangular image (Fig.C.1). The spatial transform is performed by a bilinear interpolation[1]. Consider $I(x,y)$ be the recorded and stored perspectively distorted interferogram with pixel coordinates (x,y). Then the corrected interference pattern is $I'(x,y)$ such that[1]

$$I'(x, y) = I(x', y') = I(ax + by + cxy + d, ex + fy + gxy + h)$$ (C.1)

This bilinear transformation is defined by the values of the eight coefficients a through h. By specifying the mapping of the four vertices (x_a, y_z), (x_b, y_b), (x_c, y_c) and (x_d, y_d) of the input quadrangle to the four vertices (x_0, y_0), (x_1, y_0), (x_1, y_1) and (x_0, y_1) of the output

rectangle, four equations are obtained

$$
\begin{bmatrix} x_a \\ x_b \\ x_c \\ x_d \end{bmatrix} = \begin{bmatrix} x_0 & y_0 & x_0 y_0 & 1 \\ x_1 & y_0 & x_1 y_0 & 1 \\ x_1 & y_1 & x_1 y_1 & 1 \\ x_0 & y_1 & x_0 y_1 & 1 \end{bmatrix} \begin{bmatrix} a \\ b \\ c \\ d \end{bmatrix}
\tag{C.2}
$$

After inversion of the matrix the four coefficients a, b, c and d are obtained as follows

$$
\begin{bmatrix} a \\ b \\ c \\ d \end{bmatrix} = \frac{1}{(x_0 - x_1)(y_1 - y_0)} \begin{bmatrix} y_1 & -y_1 & y_0 & -y_0 \\ x_1 & -x_0 & x_0 & -x_1 \\ -1 & 1 & -1 & 1 \\ -x_1 y_1 & x_0 y_1 & -x_0 y_0 & x_1 y_0 \end{bmatrix} \begin{bmatrix} x_a \\ x_b \\ x_c \\ x_d \end{bmatrix}
\tag{C.3}
$$

The y_a through y_d are given by

$$
\begin{bmatrix} y_a \\ y_b \\ y_c \\ y_d \end{bmatrix} = \begin{bmatrix} x_0 & y_0 & x_0 y_0 & 1 \\ x_1 & y_0 & x_1 y_0 & 1 \\ x_1 & y_1 & x_1 y_1 & 1 \\ x_0 & y_1 & x_0 y_1 & 1 \end{bmatrix} \begin{bmatrix} e \\ f \\ g \\ h \end{bmatrix}
\tag{C.4}
$$

and the four coefficients e, f, g *and* h are given by

$$
\begin{bmatrix} e \\ f \\ g \\ h \end{bmatrix} = \frac{1}{(x_0 - x_1)(y_1 - y_0)} \begin{bmatrix} y_1 & -y_1 & y_0 & -y_0 \\ x_1 & -x_0 & x_0 & -x_1 \\ -1 & 1 & -1 & 1 \\ -x_1 y_1 & x_0 y_1 & -x_0 y_0 & x_1 y_0 \end{bmatrix} \begin{bmatrix} y_a \\ y_b \\ y_c \\ y_d \end{bmatrix}
\tag{C.5}
$$

Thus once the coefficients of bilinear transform are defined, the transformation is implemented by Eq.(C.1).

Distorted quadrangle   Corrected rectangle
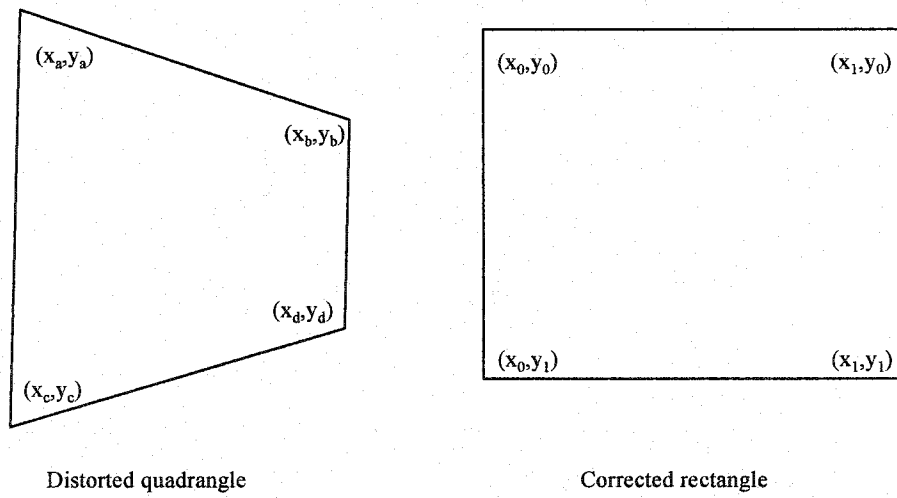
Figure.C.1: Bilinear mapping during perspective correction.

Reference:

1. P. K. Rastogi, editor *'Holographic Interferometry'*,.   Springer Series in Optical

    Sciences, Vol. 68, (Springer, Berlin, 1994), pp. 170-173.

Appendix   D

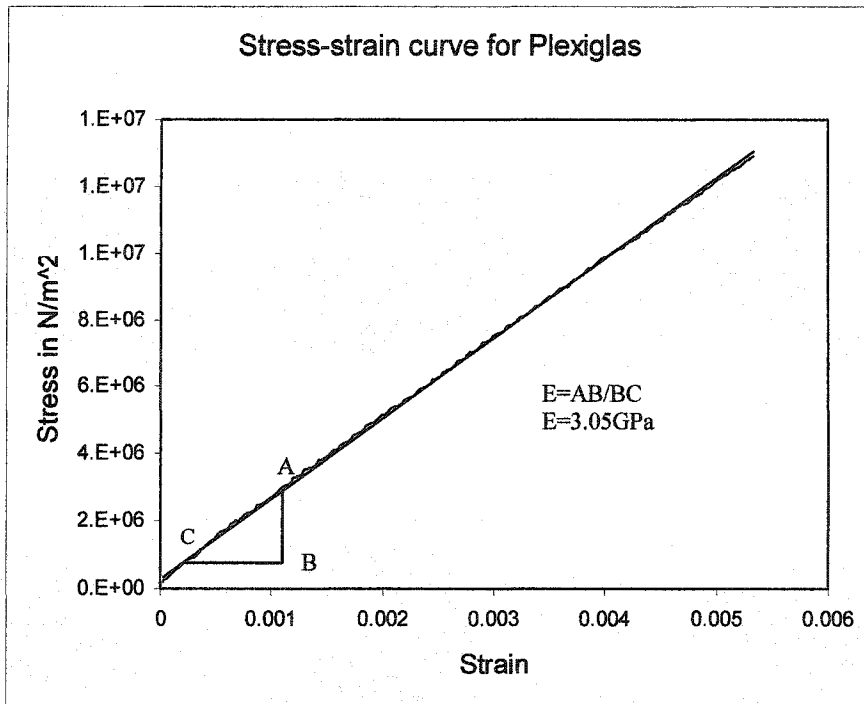# Determination of Young's modulus and Poisson Ratio Using the Strain Gauge Method

To verify the results obtained in chapters 3 and 4, it is now necessary to derive the values of Young's modulus and Poisson ratio of the samples using a well-accepted standard method. Strain gauge method, which is widely used in determining materials properties, has been used to measure the E and v values for Plexiglas and Aluminum.

A piece of Plexiglas (approximately 12cm x 2.8cm x 0.69cm) is cut from the Plexiglas sample and is fixed in the jaws of a 20,000lbs Universal Testing Machine (Fig.D.3). This machine is preset to apply 600lbs (272.11 kg) of load over 5secs. The resultant strains (both axial and transverse) are measured by a strain gauge (1/16 inch. grid length, 90° stacked gauges, made by Micro Measurements) attached on the sample. This strain gauge is connected to a signal conditioner (Vishay Instruments, 2100 series) and eventually to a digital scope (Tektronix TDS410A series) that collects the data. The Young's modulus is measured from the slope of the stress-strain curve and the Poisson ratio is measured from the ratio of the transverse strain to the axial strain. The results obtained are following:

- The Young's modulus of the Plexiglas E = 3±0.1GPa.
- The Poisson ratio of the Plexiglas is v = 0.38±.01.
- The Young's modulus of Aluminum E = 60±2GPa.

Under applied load Plexiglas creeps very fast and eventually might show lower value of E. To avoid this from happening, E has been calculated during the first 1sec of loading. The stress-strain curves are shown in Fig.D.1 and Fig.D.2.

Figure.D.1: Stress-strain curve for Plexiglas. The slope of the curve gives the value of Young's modulus.
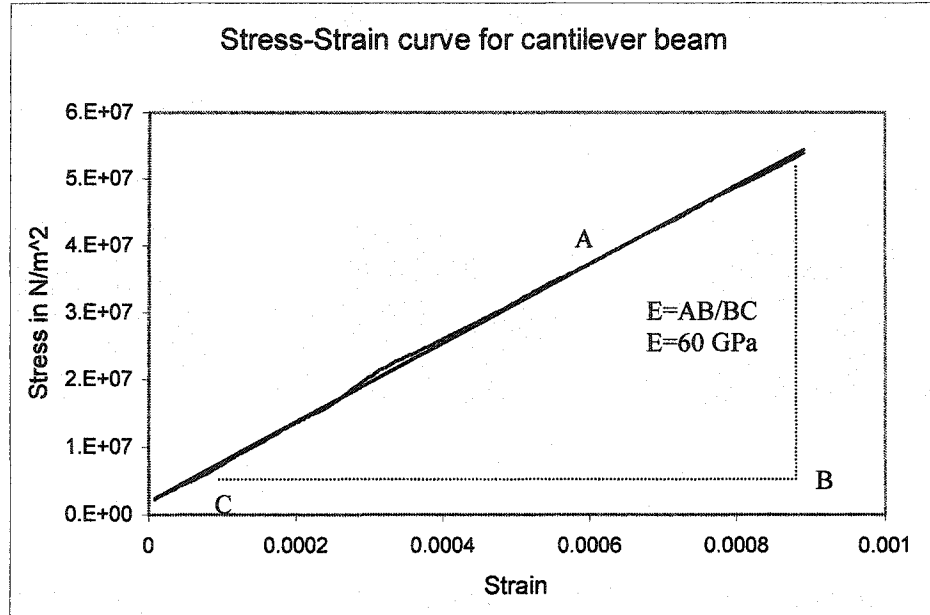
Figure.D.2: Stress-strain curve for Aluminum. The slope of the curve gives the value of Young's modulus.
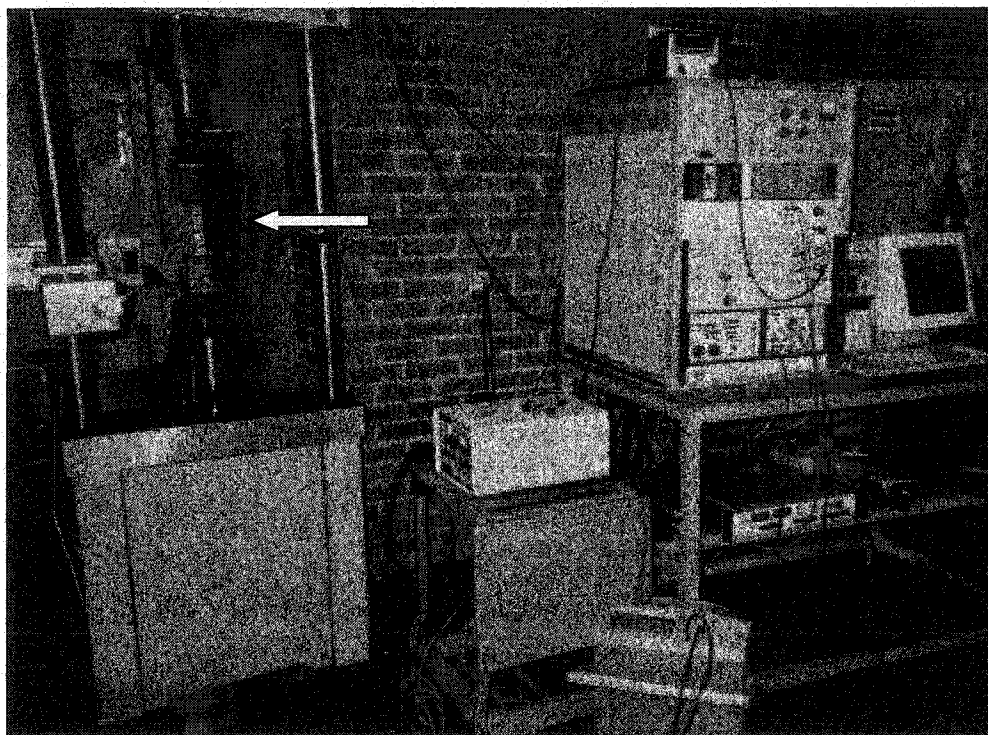
Figure.D.3: Experimental set up of Strain gauge method. The aluminum cantilever beam is placed between the jaws (Arrow).

Appendix E

Codes Used for Fringe Creation and Inversion

E.1 Codes for Fringe Formation

The analytical treatment of synthetic fringe creation and inversion is given in Appendix B. In the following section computer programs that are written for fringe creation are shown. All codes are written in MATLAB.

E.1.1 Fringe Formation for a block of sample

```
% Code name:  'makes_block_image.m'.
% Written by S. Shareef (June 2000).
%
% This program makes fringe pattern that is created by loading the sample
% by a normal force [Boussinesq method].
% First it calculates the displacements in three directions x,y, and z due to the
% force using Boussinesq displacement equations.
% Then it calls the function 'Speck.m' which produces the fringe pattern.
%
% Nomenclature:
% urow and uzeta are the radial and vertical displacements in the
% cylindrical coordinates.
% u_x, u_y and u_z are the displacements in Cartesian coordinate system.
% F,E and v are the  applied force, Young's modulus and Poisson ratio.
% lambda is the laser wavelength.
% All the units are in MKS system.
%
%
clear all; close all;
```

```
%
% Define input parameters:
length =.12;
width = .087;
E = 3E9;
F = 1000;
lambda = 829E-9;
v = 0.45;
%
%Source Positions s1 & s2
s1 = [-.023 .046 -.056];
s2 = [0.15 .051 -.054];
%
% Following generates the surface points
 [X,Y] = meshgrid(0:0.0009:length,0:0.0009:width);
%
% Point of force application
PPx = 0.063;
PPy = 0.01;
PP1 = (size(X,2)*PPx)/length;
PP2 = (size(X,1)*PPy)/width;
%
% Calculates the radial distance from the point of force application to
% all other surface points.
M = (X-X(1,PP1));
N = (Y-Y(PP2,1));
r = sqrt(M.^2 + N.^2);
%
% Calculates displacements in three directions.
urow = (-F*(1-2*v)*(1+v))./(2*pi*E.*r);
uzeta = (F * (1 - v^2))./(pi*E.*r);
u_z = uzeta;
u_x = (urow).*( M./r);
u_y = (urow).*( N./r);
%
% Calls back the function 'speck.m'.
% row is the fringe pattern intensity and phi is the phase.
```

```
[row,phi] = speck(lambda,s1(1),s1(2),s1(3),s2(1),s2(2),s2(3),u_x,u_y,u_z,X,Y);
%
% Draws the fringe pattern
x = linspace(0,length,size(row,2));
y = linspace(0,width,size(row,1));
imagesc(x,y,row);colormap(gray);colorbar;
xlabel('Length in meters');
ylabel('Width in meters');
title('Synthetic fringe pattern');
```

E.1.2 Fringe Formation for the Cantilever

The following program is similar to the previous one and uses the cantilever displacement equation to calculate the fringe pattern.

```
% Code name: 'makes_cantilever_image.m';
% Written by S. Shareef (August 2000).
% This program makes synthetic cantilever image. It uses 'speck.m' function
% to create the fringes.
% All units are in MKS system.
%
clear all; close all;
%
% Define parameters
lambda = 829E-9;
F = 0.2;
b = 0.025; %Width
d = 0.006; %Thickness
E = 70E9;
L = 0.15; %Length
I = 1/12*b*d^3;
% Generates surface points.
[X,Y] = meshgrid(0:.0003:L,0:0.0006:b);
%
%Source positions x,y,z.
s1 = [-1.9 1.3 -4.7]./100;
```

113

```
s2 = [15.5 1.5 -4.4]./100;
%
% Calculates beam deflection
deflection = ((P.*L.*X.^2)./(2*E*I))-((P.*X.^3)./(6*E*I));
u_z=deflection;
u_x=zeros(size(deflection));
u_y=zeros(size(deflection));
%
% Calls function 'speck.m' to produce the fringe pattern.
[row phi] = speck(lambda,s1(1),s1(2),s1(3),s2(1),s2(2),s2(3),u_x,u_y,u_x,X,Y);
%
% Draws the fringe pattern.
x = linspace(0,L,size(row,2));
y = linspace(0,b,size(row,1));
figure(1);imagesc(x,y,row);colormap(gray);colorbar('horizontal');
axis image;
xlabel('Length in meters');
ylabel('Width in meters');
title('Synthetic fringe pattern of cantilever beam');
```

E.1.3   Function 'speck.m'

```
% Code name: 'speck.m'.
% Written by S. Shareef (May 2000).
% This function takes the deformations in three directions x,y and z
% as input and returns the fringe intensity pattern.
%
%
function[row,phi] = speck(lambda,s1x,s1y,s1z,s2x,s2y,s2z,u_x,u_y,u_z,X,Y);
s1 = [s1x s1y s1z];
s2 = [s2x s2y s2z];
Z = zeros(size(X));
%
% Calculates the unit vectors.
magr1 = sqrt ((X - s1(1)).^2 + (Y - s1(2)).^2 + (Z - s1(3)).^2);
```

114

```
magr2 = sqrt ((X - s2(1)).^2 + (Y - s2(2)).^2 + (Z - s2(3)).^2);
n1x = (X - s1(1))./magr1;
n1y = (Y - s1(2))./magr1;
n1z = (Z - s1(3))./magr1;
n2x = (X - s2(1))./magr2;
n2y = (Y - s2(2))./magr2;
n2z = (Z - s2(3))./magr2;
%
% Calculates the sensitivity vectors.
kx = (2 * pi/lambda) * (n1x - n2x);
ky = (2 * pi/lambda) * (n1y - n2y);
kz = (2 * pi/lambda) * (n1z - n2z);
%
% Rearranges the deformations
ux = zeros(size(kx));
uy = zeros(size(ky));
uz = zeros(size(kz));
ux = ux + u_x;
uy = uy + u_y;
uz = uz + u_z;
%
% Calculates the phase and fringe intensity.
phi = kx .* ux + ky .* uy + kz .* uz;
row = (1 + cos((phi)))./2;
```

E.2   Code for Fringe Inversion

The following section shows the computer programs that are written for fringe inversion. All codes are written in MATLAB.

E.2.1 Inversion of Fringe Pattern for Block

```
% Code name: 'invert_blockimage.m'.
% Written by S.Shareef (July 2000).
%
```

```
% This program inverts the synthetic or experimental fringe pattern.
% It employs the Least Square Minimization method.
% All units are in MKS system.
%
clear all; close all;
%
% Input parameters
length =.12;
width =.087;
F = 1300;
window = 0;
lambda = 829E-9;
% Source Positions s1 & s2
s1 = [-.023 .046 -.056];
s2 = [0.15 .051 -.054];
%
% Loads the 'image' to be inverted and draws it.
load 1.v_IR_pers.mat;
xx = linspace(0,length,size(image,2));
yy = linspace(0,width,size(image,1));
figure(1);imagesc(xx,yy,image);colormap(gray);
%
% Draw the image again.
x=image;
figure(2); imagesc(x); colormap(gray);
%
% Pick Points along the fringe maxima and minima.
f_n = input('Number of fringes for which to pick points : ');
f_xy = [];
P=0; mm=0;Q=0;r=0;t=0;L=0;X=0;Y=0;X11=0;Y11=0;DD=0; D=0;ff=0;gg=0;hh=0;jc=0;
for n = f_n:-1:1;
input(['Press Enter to pick points with fringe order ',num2str((n/2)+.5),
' & Press Enter when finished']);
%
% Choose color of fringe.
color = input('What is the color of this fringe? Insert 0 for black and 1 for white: ')
clear P Q r t L X Y X11 Y11 DD ff gg hh jc mm D;
```

```
[P,Q] = getline(2);
if color == 1;
for j = 1:size(P,1);
%
% Creates a window of size rxr around the picked point and selects the maximum value within it.
r = x((round(Q(j))-window) :(round(Q(j))+window),((round(P(j))-window):(round(P(j))+window)));
[ff,gg] = max(r);
hh=max(ff);
jc1=find(ff==hh);
jc=round(0.5*(size(jc1,2)));
mm = gg(jc);
L(j) = round(P(j))-window + (jc-1);
DD(j) = round(Q(j))-window+(mm-1);
X11(j) =((length*L(j))/size(x,2));
D(j) = width*DD(j)/size(x,1);
Y11(j)=D(j);
X=X11';
Y=Y11';
ord_n = ones(length(X),1)*(n/2+.5);
figure(1);hold on; plot(X,Y,'color','black');
end
end
if color == 0;
for j = 1:size(P,1);
% Creates a window of size rxr around the picked point and selects the minimum value within it.
r = x((round(Q(j))-window):(round(Q(j))+window),((round(P(j))-window):(round(P(j))+window)));
[ff,gg] = min(r);
hh=min(ff);
jc1=find(ff==hh);
jc=round(0.5*(size(jc1,2)));
mm = gg(jc);
L(j) = (round(P(j))-window) + (jc-1);
DD(j) = (round(Q(j))-window) +(mm-1);
X11(j) = ((length1*L(j))/size(x,2));
D(j) = width*DD(j)/size(x,1);
Y11(j) = D(j);
X = X11';
```

```
Y = Y11';

ord_n = ones(length(X),1)*(n/2+.5);

figure(1);hold on; plot(X,Y,'color','white');

end

end

%

% Writes the coordinates of the picked points and the fringe orders in a matrix.

f_xy = [f_xy;ord_n X Y];

end

%

% Calculates the sensitivity vectors.

X1=f_xy(:,2);

Y1=f_xy(:,3);

Z1=zeros(size(X1));

magr1 = sqrt ((X1 - s1(1)).^2 + (Y1 - s1(2)).^2 + (Z1 - s1(3)).^2);

magr2 = sqrt ((X1 - s2(1)).^2 + (Y1 - s2(2)).^2 + (Z1 - s2(3)).^2);

n1x = (X1 - s1(1))./magr1;

n1y = (Y1 - s1(2))./magr1;

n1z = ((Z1 - s1(3)))./magr1;

n2x = (X1 - s2(1))./magr2;

n2y = (Y1 - s2(2))./magr2;

n2z = ((Z1 - s2(3)))./magr2;

kx = (2 * pi/lambda) * (n1x - n2x);

ky = (2 * pi/lambda) * (n1y - n2y);

kz = (2 * pi/lambda) * (n1z - n2z);

%

% Input coordinates of force application points.

XP1 = 0.063;

YP1 = 0.01;

MM = (X1-XP1);

NN = (Y1-YP1);

RR = sqrt(MM.^2 + NN.^2);

%

% Calculated the matrix G to be used in LSM.

A1 = (-F*MM)./(2*pi*RR.^2);

A2 = (-F*NN)./(2*pi*RR.^2);

A3 = F./(pi*RR);
```

```
G11 = (kx/(2*pi)).*A1;
G22 = (ky/(2*pi)).*A2;
G2 = (kz/(2*pi)).*A3;
G1 = G11+G22;
G = [G1 G2];
%
%
% Uses the guessed fringe order in LSM.
n_0 = f_xy(:,1);
n_1 = input('What is your guessed N order (integer) : ');
nn = (n_1:-1:-n_1);
le_and_n = [];
%
% Least Square Minimization (LSM).
for i=1:size(nn,2);
n_01=n_0-n_0(1)+nn(i);
m=inv(G'*G)*G'*n_01;
le=sum(abs(n_01-G*m).^2);
le_and_n=[le_and_n;le];
end
%
% Plots the Least square errors vs Assigned fringe order.
figure(3);
plot(nn,le_and_n)
%
% Finds the fringe order for which the least square error is minimum.
find_min11 = min(le_and_n);
find_min1 = find(le_and_n == find_min11);
find_min = find_min1(1);
n_01 = n_01-n_01(1)+nn(find_min);
% Calculates the values of Young's modulus and Poisson ratio.
m1 = inv(G'*G)*G'*n_01;
le = sum(abs(n_01-G*m1).^2)
nu = abs((m1(2,1)-m1(1,1))/(2*m1(2,1)-m1(1,1)))
E = abs((1-nu^2)/m1(2,1))
%
%
```

```
% Shows the total number of picked point.
whos X1
```

E.2.1 Inversion of Cantilever Fringe Pattern

This program is similar to the previous one except that it inverts
cantilever fringe patterns. It employs the deflection equation of
cantilever under load.

```
% Code name: 'invert_cantiimage.m'.
% Written by S. Shareef (July 2001).
% This program inverts the cantilever image for Young's modulus.
% All the units used are in MKS system.
%
%
clear all; close all;
% Input parameters
window = 0;
length =.122;
b =.025; % width;
lambda = 829E-9;
load = 0.2;
d = 0.006; % depth;
%
%Source Positions s1 & s2
s1 = [-.019  0.013 –0.047];
s2 = [0.155 0.015 –0.044];
%
% Loads the 'image' to be inverted and draws it.
load('20gm2_pers.mat');
xx = linspace(0,length,size(x,2));
yy = linspace(0,b,size(x,1));
figure(1);imagesc(xx,yy,image);colormap(gray);axis image;
%
% Draw the image again
x = image;
figure(2); imagesc(x); colormap(gray); axis image;
```

```
% Pick Points
%
f_n = input('Number of fringes (includes black & white ) for which to pick points : ');
f_xy = [];
P=0; mm=0;Q=0;r=0;t=0;L=0;X=0;Y=0;X11=0;Y11=0;DD=0;D=0;ff=0;gg=0;hh=0;jc=0;
for n = f_n:-1:1;
input(['Press Enter to pick points with fringe order ',num2str((n/2)+.5), ' & Press Enter when
finish']);
color = input('Whats the color of this fringe? Insert 0 for black and 1 for white: ')
clear P Q r t L X Y X11 Y11 DD ff gg hh jc mm D;
[P,Q] = getline(2);

if color == 1;
for j = 1:size(P,1);
r = x((round(Q(j))-window):(round(Q(j))+window),((round(P(j))-window):(round(P(j))+window)));
[ff,gg] = max(r);
[hh,jc] = max(ff);
mm = gg(jc);
L(j) = round(P(j))-window + (jc-1);
DD(j) = round(Q(j))-window+(mm-1);
X11(j) =((length1*L(j))/size(x,2));
D(j) = width*DD(j)/size(x,1);
Y11(j)=D(j);
X=X11';
Y=Y11';
ord_n = ones(length(X),1)*(n/2+.5);
figure(1);hold on; plot(X,Y,'color','black');
end
end

if color == 0;
for j = 1:size(P,1);
r = x((round(Q(j))-window):(round(Q(j))+window),((round(P(j))-window):(round(P(j))+window)));
[ff,gg] = min(r);
[hh,jc] = min(ff);
mm = gg(jc);
L(j) = round(P(j))-window + (jc-1);
```

```
DD(j) = round(Q(j))-window+(mm-1);
X11(j) =((length1*L(j))/size(x,2));
D(j) = width*DD(j)/size(x,1);
Y11(j)=D(j);
X=X11';
Y=Y11';
ord_n = ones(length(X),1)*(n/2+.5);
figure(1);hold on; plot(X,Y,'color','white');
end
end


f_xy=[f_xy;ord_n X Y];
end
%
X1=f_xy(:,2);
Y1=f_xy(:,3);
Z1=zeros(size(X1));
%
%Calculates sensitivity vector kz
%
magr1 = sqrt ((X1 - s1(1)).^2 + (Y1 - s1(2)).^2 + (Z1 - s1(3)).^2);
magr2 = sqrt ((X1 - s2(1)).^2 + (Y1 - s2(2)).^2 + (Z1 - s2(3)).^2);
n1z = (Z1 - s1(3))./magr1;
n2z = (Z1 - s2(3))./magr2;
kz = ((2*pi)/lambda).*(n1z - n2z);
% Calculates matrix G.
I = (b*d^3)/12;
n_0=f_xy(:,1);
cant_l=length;
n_1=input('What is your guessed N order (integer) : ');
nn=(n_1:-1:-n_1);
G=(load/(4*pi*I))*kz.*((cant_l.*X1.^2)-(X1.^3/3));
le_and_n=[];
% Minimization using LSM
%
for i=1:size(nn,2);
n_01=n_0-n_0(1)+nn(i);
```

```
m=inv(G'*G)*G'*n_01;
le=sum(abs(n_01-G.*m).^2);
le_and_n=[le_and_n;le];
end
%
% Plots Least square error vs Assigned fringe order.
figure(3);
plot(nn,le_and_n)
%
% Finds the fringe order value for the minimum Least square error.
find_min11 = min(le_and_n);
find_min1 = find(le_and_n == find_min11);
find_min = find_min1(1);
n_01 = n_01-n_01(1)+nn(find_min);
%
% Uses the correct fringe order value to determine Young's modulus.
m1=inv(G'*G)*G'*n_01;
le=sum(abs(n_01-G*m1).^2)
E=abs(1/m1)
%
% Total number of picked points.
whos X1
```